Precision Magnetometry and Imaging via Quantum Manipulation of Spins in Diamond

by
Keigo Arai

B.S., The University of Tokyo (2008)

Submitted to the Department of Physics
in partial fulfillment of the requirements for the degree of

Doctor of Philosophy in Physics

at the
MASSACHUSETTS INSTITUTE OF TECHNOLOGY

February 2016

Author ... Signature redacted .....
Department of Physics
January 27, 2015

Certified by. Signature redacted .....
Ronald Walsworth
Senior Lecturer, Harvard University
Thesis Supervisor

Certified by.. Signature redacted .....
Isaac Chuang
Professor of Physics
Thesis Co-supervisor

Accepted by ..... Signature redacted
Nergis Mavalvala
Professor of Physics
Associate Department Head for Education

Precision Magnetometry and Imaging via Quantum Manipulation of Spins in Diamond

by

Keigo Arai

Submitted to the Department of Physics on January 27, 2015
in partial fulfillment of the requirements for the degree of
Doctor of Philosophy in Physics

Abstract

Precise control of quantum states is a cornerstone of quantum science and technology. Recently, a multi-level electronic spin system in a robust room-temperature solid, based on the nitrogen-vacancy (NV) color center in diamond, has emerged as a leading platform for quantum sensing as well as quantum information processing at room-temperature. Developing new approaches to high-precision NV spin manipulation provides key insights for advancing these quantum technologies.

In this thesis, I demonstrate three experimental methods for controlling NV spins with various concentrations toward high-performance magnetic field sensing and imaging. First, the wide-field optical magnetic microscopy experiment provides ensemble-NV control via continuous-wave electron spin resonance and camera-based parallel spin-state readout. This microscope offers a factor of 100 larger field-of-view compared to the confocal detection size, which enables magnetic imaging of populations of living bacteria. Second, the Fourier magnetic imaging experiment demonstrates for the first time multiple-NV control using phase encoding. Pulsed magnetic field gradients encode in the NV spin phase the information about the position of the NV centers as well as the external magnetic field in the Fourier-space. This scheme allows 100-fold improvement in spatial resolution beyond the optical diffraction limit, and has higher signal-to-noise ratio than other superresolution imaging techniques when applied to NV spins. Third, the geometric phase magnetometry experiment employs single-NV control using a Berry sequence, consisting of off-resonant microwaves whose parameters vary along a cyclic path, thereby realizing 100 times larger magnetic field dynamic-range compared to the typical Ramsey-type interferometry approach. Finally, I discuss the possibilities of combining these techniques to realize various other quantum applications in future work.

Thesis Supervisor: Ronald Walsworth
Title: Senior Lecturer, Harvard University

Acknowledgments

I am able to write this acknowledgment now, thanks to all the people who supported my thesis research.

Firstly, I would like to express my sincere gratitude to my supervisor, Dr. Ronald Walsworth, for the continuous guidance of my Ph.D. research, for his understanding, motivation, and tremendous knowledge. His encouragement always gave me confidence and energy. He also allowed me a lot of flexibility and freedom so that I can become an independent researcher.

My sincere thanks also go to my co-supervisor, Prof. Isaac Chuang, for his assistance and insightful comments on my research direction and thesis writing. His questions gave me precious opportunities to look at my research from different perspectives.

Besides, I would also like to thank the rest of my thesis committee for their stewardship of my thesis: Prof. Vladan Vuletić and Prof. Pablo Jarillo-Herrero for their advice and support, which let me broaden my knowledge and consider exploring new directions after the Ph.D.

My thesis research involved a lot of collaborations with many groups. In particular, I would like to thank Prof. Amir Yacoby, Prof. Paola Cappellaro, Prof. Mikhail Lukin, Prof. Arash Komeili, and Prof. Nir Bar-Gill, for giving me a lot of constructive comments in writing the papers. I also thank all of my collaborators and friends in these groups.

Throughout my thesis research, I had a lot of stimulating discussions with all of the Walsworth group members. I could have never been achieved this thesis work without them. Whenever I encountered a problem, there was always somebody who had a good idea. During the first two years, Dr. David Le Sage and Dr. Linh Pham kindly taught me important experimental skills, such as how to align optics, control microwaves, and use computer software. The wide-field imaging project was successful thanks to these two and Dr. David Glenn and Dr. Stephen DeVience. The next two years were dedicated to the magnetic field gradient techniques, developed together with Dr. Chinmay Belthangady and Dr. Huiliang Zhang. I learned from them many advanced topics about nanofabrication, magnetic resonance imaging, and signal compression. In the last two years, Paul Junghyun Lee worked with me. His data analysis and simulation skills were indispensable for completing the geometric phase magnetometry project. Also, I'd like to thank all of my friends, who supported my Ph.D. life in Cambridge.

Lastly, I thank my family for their heartwarming support for everything.

Contents

Citations to Previously Published Work

Chapter 3 has been published in the following paper:

> D. Le Sage*, K. Arai*, D. R. Glenn*, S. J. DeVience, L. M. Pham, L. Rahn-Lee, M. D. Lukin, A. Yacoby, A. Komeili, and R. L. Walsworth. Optical magnetic imaging of living cells. *Nature* **496**(7446):486-489 (2013).

Chapter 4 has been published in the following paper:

> K. Arai*, C. Belthangady*, H. Zhang*, N. Bar-Gill, S. J. DeVience, P. Cappellaro, A. Yacoby, and R. L. Walsworth. Fourier magnetic imaging with nanoscale resolution and compressed sensing speed-up using electronic spins in diamond. *Nature Nanotechnology* **10**(10):859-864 (2015).
>
> *These authors contributed equally to this work.

List of Figures

List of Tables

Chapter 1

Introduction

Discovery of a new type of symmetry often evokes a huge thrust toward harnessing it. The spin degree of freedom, first introduced by Wolfgang Pauli, is a notable example of great success in quantum physics that has led to a wide range of applications, such as magnetic resonance imaging [149, 171] in medicine and giant magnetoresistance [18, 32] in the computer industry. As optical and electronic technologies advance, researchers also foresee many quantum applications of spin degrees of freedom, ranging from quantum sensing [41, 225, 274] and metrology [96, 136, 273] to information processing [85, 132, 137, 162]. However, these applications typically require spin control with unprecedented precision. Because it is generally a magnetic field that enables manipulation of spins [234], it implies that developing spin-based magnetometry is an important touchstone for these future applications. This thesis explores three novel experimental approaches for manipulating spins in solid-state materials, each of which enables a new class of high-performance magnetic field sensing and imaging applications.

1.1 Precision Magnetometry and Imaging

Measurement of magnetic fields with high precision is a centerpiece of many applications in biomedical and physical sciences. Researchers have developed various types of magnetometers. Because magnetic systems in nature are diverse, a wide range of specifications is used to evaluate the performance of those magnetic field sensing and imaging systems. Important ones include magnetic field sensitivity, dynamic range, field-of-view, spatial resolution, imaging speed bandwidth, and operating temperature. This section overviews the basic principle of magnetic field sensing, the relevant figures-of-merit, common magnetometry techniques, and their advantages as well as limitations.

1.1.1 Operating principle and performance

The general operating principle behind magnetic field sensing is to measure a response of a sensor against an input magnetic field B. Depending on the sensor, the change of the state, or output f, can appear in various forms, such as electric potential, electric current, and photon emission. The responsivity R of the sensor can be defined as the input-output gain

$$R = df/dB. \tag{1.1}$$

For example, for a sensor based on voltage response, the responsivity has a unit of [V T^{-1}].

Sensitivity The magnetic field sensitivity η is a measure of the minimum detectable magnetic field achieved within a unit measurement time. In experiments, a sensor undergoes many types of noise. Examples include thermal noise and shot noise. The dominant source of noise usually depends on the measurement timescale and has a finite bandwidth. The measurement noise is thus characterized by the noise spectral

density defined as

$$S_f(\omega) = \lim_{T\to\infty} \frac{\langle |F_T(\omega)|^2 \rangle}{2\pi T}, \tag{1.2}$$

where $F_T(\omega)$ is the Fourier transform[1] of a random noise $\delta f(t)$ in the time domain evaluated between $-T/2$ and $+T/2$:

$$F_T(\omega) = \int_{-T/2}^{+T/2} \delta f(t) e^{-i\omega t} dt. \tag{1.4}$$

The magnetic field sensitivity η is then given by the square-root of noise spectral density divided by the responsivity

$$\eta = \frac{\sqrt{S_f}}{R}. \tag{1.5}$$

For example, for a sensor based on voltage response, the noise spectral density and sensitivity have units of $[\mathrm{V}^2\cdot\mathrm{Hz}^{-1}]$ and $[\mathrm{T}\cdot\mathrm{Hz}^{-\frac{1}{2}}]$, respectively. The noise spectral density for six commonly used magnetometers is discussed in the next section.

Field dynamic range The field dynamic range $B_{\max}$ is defined as the maximum detectable magnetic field. There are mainly two causes that fundamentally limit the dynamic range. The first one is the sensor breakdown field, at which the sensor loses the capability of measuring the magnetic field. For example, fluxgate magnetometry employs a ferromagnetic core, whose magnetic response approaches zero above approximately a few times of the coercivity. Thus, this value roughly gives the dynamic range. The second one is signal ambiguity. For example, in interferometry-based magnetometry such as Ramsey d.c. magnetic field sensing, the output signal be-

[1] A finite interval is considered because for a stochastic process

$$\int_{-\infty}^{+\infty} |\delta f(t)|^2 dt \to \infty. \tag{1.3}$$

comes a sinusoidal function of magnetic field. Then there are multiple possibilities of magnetic field value that give the same signal level. This will limit the dynamic range within one cycle of oscillation unless some phase estimation is applied.

Spatial resolution The spatial resolution δx of magnetic imaging is usually limited by either of the two parameters: (i) source-to-sensor distance d and (ii) physical size of the sensor L. If the source-to-sensor distance d is large, the magnetic field pattern is blurred at the sensor. If there are a few magnetic field sources which are close to each other compared to d, it is already a challenging computational problem to reconstruct the distribution of the source. If the sensor size L is larger than the characteristic scale of a magnetic field pattern, the pattern is averaged out and the magnetic image is not constructed properly. For a point magnetic sensor such as NV centers, the first parameter is often the problem unless one collects signals from a large ensemble of NV centers. If an ensemble of NV centers is used to improve sensitivity, the second parameter also becomes a problem. On the other hand, for magnetometers which are sensitive to magnetic flux, such as superconducting quantum interference devices (SQUID), the second parameter generally gives a technical limitation. A general trend is that as the sensor size decreases, the sensitivity becomes worse. Thus, there is oftentimes a trade-off between spatial resolution and sensitivity.

Imaging speed To construct a magnetic image, there are mainly two approaches: parallel detection and point-by-point scanning. The former approach employs multiple detectors simultaneously, and therefore, in principle, the imaging time does not increase linearly with the number of imaging pixels. However, depending on what type of parallel detector is used, an additional offset time might be added. For example, for parallel detection with charge-coupled devices (CCD) or complementary metal-oxide-semiconductors (CMOS), the sensor elements need to relay the charge

packets (electrons) in potential wells to count the number of photons at each pixel, which is the main technical limitation of readout speed. For a point-by-point scanning system, the physical scanning time technically limits the imaging speed. For example, in a scanning probe system, the probe is usually controlled via piezoelectric actuator with a finite traveling speed, which is ultimately limited by the speed of sound.

1.1.2 Approaches for magnetic field sensing

Here various types of commonly used magnetometry techniques are classified into three categories: (i) atom-based, (ii) electric-circuit-based, and (iii) solid-state-spin-based magnetometers (Table 1.1).

Atom-based magnetometry

Vapor cell magnetometry – Vapor cell magnetometers [5, 41] consist of a vapor of alkali atoms enclosed in a glass cell. When the cell is illuminated by a lamp or a laser beam, the atoms inside are optically excited to higher energy states and decay to a single lower energy state (polarization). An external field, shifting the energy levels, is measured via absorption of light or polarization rotation of transmitted light. Although this technique provides only a sub-millimeter-scale spatial resolution, limited by the vapor size, it can be operated at room temperature and offers the best sensitivity (0.54 fT $\mathrm{Hz}^{-\frac{1}{2}}$ [140]) among many others, and thus finds many applications. For a polarization-rotation-based detection with duration τ, the signal exhibits a sinusoidal function

$$f(B) \sim \cos(\gamma B \tau), \tag{1.6}$$

where γ is the gyromagnetic ratio. When the Larmor precession angle is of the order unity, the measurement uncertainty δB is proportional to $1/\tau$. If this

measurement is repeated T/τ times, where T is the total measurement time, the uncertainty gains a factor of $(T/\tau)^{-\frac{1}{2}}$. If there are N sensing atoms, it also improves by $N^{-\frac{1}{2}}$. Consequently, the sensitivity is scaled as

$$\eta = \delta B\sqrt{T} \propto \frac{1}{\sqrt{N\tau}}. \tag{1.7}$$

Quantum theory shows that using spin-squeezing, one can go below this scaling limit. The dynamic range is defined as one cycle of oscillation $B_{\text{mat}} \propto 1/\tau$ due to 2π phase ambiguity; however, this can be further enhanced via quantum phase estimation algorithms (see also Section 1.2.3). In applications, the most notable example is the nuclear magnetic resonance imaging (MRI) of a human body [228]. It is also employed for precision measurements of fundamental and particle physics, such as electric dipole moments and axion search [184, 279], and local Lorentz invariance test [26, 38].

BEC magnetometry – Another variant of the atom-based approach is Bose-Einstein condensate (BEC) magnetometry [265]. In the presence of an external magnetic field, a ^{87}Rb BEC undergoes the Larmor precession, which can be imaged optically. The BEC magnetometry offers significant improvement in spatial resolution (limited by the optical diffraction $\sim$ 300 nm). The fundamental limit of the sensitivity is given by the atom shot noise ($\sim$ 1 pT Hz$^{-\frac{1}{2}}$). The number of atoms can be recast as $N = nA$, where n is the local density of the BEC gas and A is the measurement area of interest. The area scaling for BEC magnetometry is thus $\sim A^{-1/2}$. The BEC size is limited by the size of an external potential well and is independent of the number of atoms.

Electric-circuit-based magnetometry

SQUID magnetometry – The electric-circuit-based approach is another promis-

ing direction. One successful example is the SQUID, consisting of superconducting loops containing Josephson junctions [12]. There are several SQUID species, such as radio frequency, direct current (d.c.), and relaxation SQUIDs. The d.c. scheme [124] employs two Josephson junctions in parallel. One important aspect of SQUID magnetometry is that it is sensitive to magnetic flux

$$\Phi = \int_{\text{loop}} \mathbf{B} \cdot d\mathbf{A}, \tag{1.8}$$

where $d\mathbf{A}$ is the area element of the SQUID loop. If there is an external magnetic flux, a "screening current" circulates in the loop and cancels the magnetic flux. Once the current exceeds a critical value, an electric potential appears across the junction. As the flux increases, the direction of screening current alternates every half of the magnetic flux quantum $\Phi_0 = 2.06 \times 10^{-15}$ Wb. Thus, the electric potential becomes a function of the applied magnetic field. One strength of the SQUID is that the noise spectrum, which gives one of the fundamental limits, follows $1/f$ for lower frequency side, reaching the < 10 fT $\text{Hz}^{-\frac{1}{2}}$ level at ~ 1 kHz, and then becomes white beyond that at the operating temperature of liquid helium (4.2 K). This white spectrum originates from thermal noise in the resistive shunt circuit [13]. It is also common to operate SQUID at relatively higher temperatures (77 K) under open conditions, and thus SQUID has been used for imaging various small biomagnetic samples [243]. For a typical loop area of 100 μm $\times$ 100 μm and a flux noise spectral density of $\sim 10^{-6}\Phi_0$ $\text{Hz}^{-\frac{1}{2}}$, the magnetic field sensitivity reaches $0.2 - 2$ pT $\text{Hz}^{-\frac{1}{2}}$. Unlike vapor cell magnetometry, a sub-micron scale spatial resolution is achievable by use of nanoscale Josephson junctions [88]. However, since the magnetic field sensitivity is fundamentally limited by the sensing area, there is a trade-off between spatial resolution and sensitivity. In addition, the linewidth of the superconducting

wires sets a technical limit for the loop size because the wire width should be larger than the penetration depth of the superconducting material.

Fluxgate magnetometry – The fluxgate magnetometer is one of the oldest magnetometry techniques and has been used for navigation and metal detection [16, 219, 220]. Among many designs, one example consists of two parallel bars of high-permeability ferromagnetic metal (core) wrapped by two electromagnetic coils for excitation and sensing. When an oscillating electric current is sent through the excitation coil, the cores induce a.c. magnetic fields. The direction of winding is reversed between the two bars, so that the magnetic fields will cancel each other under zero field. However, in the presence of an external magnetic field, the induced magnetic fields are imbalanced, which can be detected by the sensing coil. This technique provides a sensitivity of ~ 1 pT $\mathrm{Hz}^{-\frac{1}{2}}$ and a resolution of ~ 1 mm. What limits the sensitivity of fluxgate magnetometry is the white noise from the core and $1/f$ noise; however, the nonlinearity of fluxgate operation makes it difficult to construct a simple theoretical model of the noise [219].

Scanning Hall probe magnetometry – Hall probe microscopes are also an electric-circuit-based magnetometry system. A Hall sensor made of 2D electron gas materials (e.g. GaAs/AlGaAs) using standard semiconductor fabrication techniques (molecular-beam-epitaxy) detects tunneling current exerted by an external magnetic field. A scanning method is commonly used together to construct magnetic images because scanning probe microscopy allows accurate and precise control over the sample position. The responsivity is given by

$$R = \frac{|R_H|}{t} = \frac{1}{net}, \tag{1.9}$$

where R_H is the Hall coefficient, t the Hall bar thickness, $e = 1.6 \times 10^{-19}$ C the electric charge, and n the carrier density. Typically, the responsivity reaches $\sim$ 2000 $\mathrm{VA^{-1}T^{-1}}$ over a wide temperature range. The main sources of noise are $1/f$ noise, thermal noise, and generation-recombination noise. Large Hall probes carry smaller $1/f$ noise because of the large number of carriers. At a temperature of <100 K, thermal noise sets the fundamental limit (< 100 nT $\mathrm{Hz}^{-\frac{1}{2}}$), especially for small probes [196]. Experimentally, current fluctuations often cause a dominant noise floor ($\sim$ 1 μT $\mathrm{Hz}^{-\frac{1}{2}}$) [116]. It is also important to remove acoustic noise and air flow because the scanning system is susceptible to instrumental vibrations. Since the Hall effect doesn't depend on the size of a circuit, this approach in principle offers high spatial resolution ($\sim$ 300 nm) as well as reasonably good magnetic field sensitivity over a broad range of temperatures (1 mK to 500 K) [46].

Solid-state-spin-based magnetometry

MRFM – The third class is solid-state-spin-based magnetometry, among which magnetic resonance force microscopy (MRFM) [225] also uses a scanning probe system. It consists of a ferromagnetic (e.g. FeCo) tip attached to a cantilever. When the cantilever approaches the sample of interest, a small force is exerted on the cantilever due to a strong magnetic field gradient ($\sim$ 10 G $\mathrm{nm^{-1}}$). The cantilever oscillates when the direction of spins is flipped periodically. The amplitude of the oscillation is then read out via laser interferometry. Thermal motions of the cantilever fundamentally limit the magnetic field sensitivity. From a simple thermodynamic analysis, the noise power spectrum is given by

$$S_f = \frac{2k}{\omega_0 Q} k_B T, \tag{1.10}$$

where k, ω_0, and Q are the spring constant, resonance frequency, and quality factor of the cantilever, respectively. The shot noise of the photons reflected from the cantilever for tip displacement detection is almost always smaller than the thermal noise, and thus can be neglected. In addition, when small spin ensembles are considered, statistical fluctuations in the nuclear magnetization $\sigma_s \propto \sqrt{N}$, where N is the number of spins, is another important fundamental limitation, which has just recently been investigated in detail [120]. The spatial resolution of MRFM is proportional to the magnetic field gradient, which decreases as the apparatus size L increases. Taking advantage of the small size of the ferromagnetic tip and precise control of scanning probe microscopy, MRFM offers unprecedentedly high spatial resolution (< 10 nm), which is useful for imaging nanoscale samples, such as viruses [61]. However, it is also known that signal-to-noise decreases with the square root of the size, setting a fundamental limit on spatial resolution.

GMR/AMR magnetometry – Giant magnetoresistance (GMR) and anisotropic magnetoresistance (AMR) are a family of magnetoresistance effects [18, 32, 177]. The GMR structure consists of an ultrathin conductive, nonmagnetic (e.g. Cu) interlayer sandwiched between two ferromagnetic layers. Because of antiferromagnetic exchange interaction, these layers have opposite magnetic moment directions. Under this spin configuration, electron scattering increases significantly and the interlayer becomes highly resistive. When an external magnetic field is present, however, the magnetic moments of the two ferromagnetic layers are aligned, and the interlayer resistance decreases drastically. The AMR is another approach, which makes use of permalloy (Ni 80% Fe 20%), whose magnetization direction is dependent on the external magnetic field. The resistance of permalloy decreases as the magnetization rotates away from the direction of

electric current. These techniques provide $\sim$ 1 nT $\text{Hz}^{-\frac{1}{2}}$ sensitivity and micrometer scale resolution under ambient conditions, and thus have been used as biosensors [23, 99, 180, 218]. Having been adopted gradually in microelectromechanical system (MEMS) and silicon integrated circuit (IC) processing technologies, GMR/AMR magnetometry will also find broad ranging applications in consumer electronics, such as smart phones and computer tablets [56].

NV diamond magnetometry– Spin-based magnetometry generally provides high spatial resolution. To overcome the limitations of low temperature operating conditions, researchers proposed to use spins in solid state systems [41, 249]. The electronic spin associated with nitrogen-vacancy (NV) color centers in diamond [112, 163] is of particular importance as it has long coherence time and can be read out optically under ambient conditions [19, 176]. In NV magnetometry, an external magnetic field shifts the ground state energy, which is read out via optically-detected magnetic resonance. The signal is thus obtained as a change of fluorescence intensity. As in atom vapor cell magnetometry, the NV center acquires precession phase proportional to the external field B. The phase is then projected onto the population difference. Thus, the signal becomes a sinusoidal function

$$f(B) \sim \cos(\gamma B \tau), \tag{1.11}$$

where γ is the gyromagnetic ratio and τ is the precession time. The responsivity $R \propto (\gamma\tau)^{-1}$ has a unit of $[\text{T}^{-1}]$. The photon shot noise sets a limitation on sensitivity $\eta = \delta B\sqrt{T} \propto (N\tau)^{-\frac{1}{2}}$, where N is the number of NV centers. In experiments, the shot noise scaling is modified as

$$\eta \propto \frac{1}{\sqrt{N}} \frac{\sqrt{\tau + \tau_{i/r}}}{\tau} \tag{1.12}$$

due to additional offset time, such as initialization and readout times $\tau_{i/r}$. It is also noted that one can reach the Heisenberg limit by several approaches (for example, quantum phase estimation protocols or non-classical states). Because of high spatial resolution, reasonably good sensitivity, and room temperature operating conditions, NV magnetometry has been applied to various magnetic systems in biology [150], geology [90], and condensed matter physics [250, 263]. The fundamental and technical limitations of spatial resolution, imaging speed, and dynamic range are discussed in more detail in the following sections.

1.2 Research Objective

In this section, for each of three experiments discussed in Chapter 3-5, I summarize (i) the fundamental & technical limitations of the existing technologies, (ii) reasons why the new approach taken in the thesis work is chosen, and (iii) how that approach improves the fundamental limits.

1.2.1 Wide-field magnetic imaging

The key concepts for high-throughput magnetic field imaging of nanoscale magnetic systems is detection parallelization as well as high spatial resolution.

Comparison between magnetic imaging techniques

Here electron holography and scanning SQUID magnetometry are compared with wide-field magnetic imaging with ensemble NV in detail (Table 1.2).

Electron holography is a holography imaging technique based on electron matter waves [75]. First, accelerated electrons are split into two beams. As the reference beam travels, its wave function acquires phase $\psi_0(\mathbf{r}) = \exp(i\mathbf{k}\cdot\mathbf{r})$. The

Table 1.1: Comparison of various types of magnetometers. (i) Atom-based: Alkali vapor cell magnetometry [41, 140] and BEC magnetometry [265]. (ii) Electron-based: SQUID magnetometry [12, 88, 124], fluxgate magnetometry [16], and scanning Hall probe microscopy [46, 196]. (iii) Spin-based: MRFM [225], GMR/AMR magnetometry [56], and NV diamond magnetometry [249].

	Sensitivity	Resolution	Operating conditions
(i) Atom			
Vapor cell	0.5 fT $Hz^{-\frac{1}{2}}$	< 1 mm	Ambient
BEC	0.1 pT $Hz^{-\frac{1}{2}}$	300 nm	High vacuum
(ii) Electron			
SQUID	1 fT $Hz^{-\frac{1}{2}}$	< 1 μm	Cryogenic
Fluxgate	1 pT $Hz^{-\frac{1}{2}}$	< 1 mm	Ambient
Hall probe	1 nT $Hz^{-\frac{1}{2}}$	300 nm	Ambient
(iii) Spin			
MRFM	1 fT $Hz^{-\frac{1}{2}}$	< 10 nm	Cryogenic
GMR/AMR	< 1 nT $Hz^{-\frac{1}{2}}$	< 1 μm	Ambient
NV diamond	1 pT $Hz^{-\frac{1}{2}}$	< 10 nm	Ambient

other beams passes through a sample and its wave function acquires additional phase $\psi_s(\mathbf{r}) = \exp(i\mathbf{k}\cdot\mathbf{r} + \phi(\mathbf{r}))$ due to the Aharonov-Bohm effect. Here the extra phase is obtained as an integral of the longitudinal component of a vector potential A_z across the sample

$$\phi(x,y) = -\frac{e}{\hbar}\int A_z(x,y,z)dz. \tag{1.13}$$

Finally, they are combined together to produce an interference pattern on a camera

$$I = |\psi_0 + \psi_s|^2. \tag{1.14}$$

The point spread function of electron holography is a Fresnel zone pattern. The spatial resolution of electron holography is given by $\delta x \sim \lambda d/s$, where λ is electron wavelength, d distance between sample and screen, and s the separation between the first minimum points on each side of the sinc function, caused by a finite size of the detector. For a typical value of $\lambda = 0.1$ nm, $d = 10$ cm and $s = 10$ mm, the spatial resolution reaches ~ 1 nm. Recently, pulsed electron holography method has demonstrated acquisition of an image from ~ 1 μm field-of-view in an exposure time of ~ 50 μs [95]. In this pulsed regime, the imaging speed is only limited by the camera frame rate. One drawback of this technique is that the sample has to be in a vacuum, which precludes magnetic imaging of living biological samples.

Scanning SQUID magnetometry is another widely used magnetic imaging technique [210, 243]. Since SQUID is sensitive to a magnetic flux, its spatial resolution is limited by the SQUID loop size and large standoff distance between the sample and the loop. Nonetheless, it is still useful for magnetic field measurements of various biological magnetic samples because SQUID offers extremely

high sensitivity enabling fast data acquisition. One drawback of the SQUID is that it is difficult to operate multiple SQUID detectors in parallel like an imaging camera because if two sensor elements are placed close to each other, they can interfere. The imaging speed is mainly limited by a physical scanning of the SQUID loop. For example, a typical piezoelectric scanning system offers a scanning speed of ~ 100 nm s^{-1}.

Ensemble NV – What makes NV centers useful for wide-field magnetic imaging is twofold: (i) the NV center is considered as a point magnetic field sensor and (ii) its spin state can be read out optically. The first advantage means that NV centers can be packed closely and prepared over a wide area (ensemble NV). Furthermore, the fact that NV magnetometry can be operated under ambient conditions (room temperature and atmospheric pressure) means that the magnetic samples can be placed directly on top of a diamond chip. Each NV center with approximately 'zero' volume then senses the local magnetic field created by the sample. By mapping fluorescence from NV centers to an image sensor such as CCD or CMOS, one can construct a magnetic field pattern. These advantages allow, for example, imaging of living biological samples with nanometer scale spatial resolution [150], which is difficult for electron holography or scanning SQUID.

Limitations of NV wide-field magnetic imaging

The spatial resolution of NV magnetometry is limited by three things: optical diffraction, standoff distance between the sensor and sample, and NV layer thickness. The first one, optical diffraction limit, can be broken with superresolution techniques. However, to date, superresolution techniques generally suffer from slow imaging speed or system drift (see Section 1.2.2). The second one depends on the thickness of a mag-

netic sample. A thick biological sample (> 1 μm) needs to be sliced to achieve close to the diffraction-limited spatial resolution, which makes it challenging to study the sample under living conditions. The third one gives a trade-off between spatial resolution and sensitivity. If this is the dominant limitation, the spatial resolution δx is roughly proportional to the thickness of the NV layer L

$$\delta x \propto L. \tag{1.15}$$

For magnetic imaging with ensemble NV centers, the sensitivity is also dependent on the thickness of the NV layer through

$$\eta \propto \frac{1}{\sqrt{nL^3}}, \tag{1.16}$$

where n is the density of the NV centers.

There are also several other technical limitations in imaging speed and field-of-view. Parallel fluorescence detection using image sensors offers faster acquisition of magnetic field information from across the whole magnetic sample [97, 150, 205] compared to a scanning system. However, the frame rate and semiconductor well depth give new limitations on imaging speed. Another key technical challenge toward larger field-of-view is how to deliver wide-field laser illumination and homogeneous microwave excitation fields for simultaneous control of a large NV ensemble. It should also be mentioned that an external magnetic field is measured with magnetic resonance. Thus, for a typical ensemble NV sample with a density of $\sim 10^{16}$ cm^{-3}, small heterogeneity of NV density causes a variation of fluorescence intensity pattern (< 10 % over ~ 1 μm), leading to an inhomogeneous sensitivity. However, it doesn't affect the spatial resolution or parallelization very much.

Table 1.2: Comparison of three wide-field magnetometers in terms of spatial resolution, parallelism, field-of-view (FOV), and data acquisition time.

	Resolution	Parallelism	FOV	Imaging speed
Electron holography [75]	1 nm	Yes	1 μm	50 μs/image
Scanning SQUID [210]	$\sim$ 1 μm	No	30 μm	10 ns/pixel
Ensemble NV [150]	300 nm	Yes	100 μm	$\sim$ 1 s/image

Objective of wide-field magnetic imaging experiment

The goal of this project is to (i) develop a prototype of wide-field magnetic imaging system using an ensemble of NV centers and a camera, (ii) demonstrate optical magnetic imaging of living magnetotactic bacteria, and (iii) study the individual differences of magnetic moments that the bacteria grow in their bodies. It is also important to show that NV magnetic imaging with high spatial resolution and wide field-of-view is useful for studying various other magnetic systems, such as magnetically labeled cells [97] in biology and magnetized meteorites in geology [90]. Furthermore, this system can also be used for imaging electric field [68], temperature [55, 145, 258], and pressure [42] profiles.

1.2.2 Fourier magnetic imaging

As explained in the previous section, spatial resolution is a key figure-of-merit for magnetic imaging. One of the advantages of NV magnetometry is fluorescence readout (640 – 800 nm) because one can immediately achieve the optical diffraction-limited spatial resolution

$$\delta x \sim \frac{\lambda}{2\mathrm{NA}}, \tag{1.17}$$

where λ is the wavelength of fluorescence emission, and NA is the objective numerical aperture. In particular, a confocal laser scanning system offers $\sim$ 300 nm resolution. In the past few years, many experiments toward nanometer-scale NV magnetic imaging were proposed and demonstrated. These are classified into two categories: (i) real-space approach and (ii) transformed-space approach (Table 1.3).

Comparison between real-space approach and transformed-space approach

Examples of real-space approach are stimulated emission depletion (STED) microscopy [174, 260], deterministic emitter switch microscopy (DESM) [48], and scanning probe microscopy (SPM) [101, 168, 250].

Stimulated emission depletion microscopy – The general operating principle of STED is to acquire fluorescence from only a target fluorophore by selectively deactivating the other fluorophores around the target via a doughnut-shaped beam [117]. The spatial resolution depends on the intensity of the doughnut beam

$$\delta x = \frac{\lambda}{2\mathrm{NA}} \frac{1}{\sqrt{1 + I/I_s}}, \tag{1.18}$$

where I_s and I are the fluorophore saturation intensity and doughnut beam intensity, respectively. In 2010, this technique was combined with NV centers and demonstrated 38 nm spatial resolution [174]. The main technical limitations on resolution are doughnut beam intensity, imperfections of the doughnut intensity zero, and mechanical instability of imaging setup. The first one affects the resolution directly, and the last two lead to a contrast reduction. Further improvements in doughnut beam intensity and beam quality enabled 2.4 nm resolution in 2012 [272]. There are largely two drawbacks in this technique. First, a large beam intensity ($\sim$ 1 GW cm^{-2}) is required for doughnut beam to achieve nanometer-scale resolution. Second, imaging speed is relatively slow

(typically $\sim$ 10 s per pixel) [174]. These two disadvantages make it difficult to apply this technique to studying biological samples.

Deterministic emitter switch microscopy – In contrast to the STED technique, stochastic super-resolution techniques, such as photoactivated localization microscopy (PALM) [30] and stochastic optical reconstruction microscopy (STORM) [226] require smaller excitation intensity and allow parallel detection of fluorescence using a camera. In these techniques, photo-switchable fluorophores are sequentially activated for time-resolved localization. Recently, STORM demonstrated an image acquisition time of 30 s with a spatial resolution of 20 nm over $\sim 20 \times 20$ μm^2 field-of-view using a relatively lower excitation power of $\sim$ 15 kW cm^{-2}. In NV magnetometry, this concept was applied to imaging of nanodiamonds (DESM [48]). Since nanodiamonds are oriented in random directions, they exhibit different resonance frequencies. Using resonant microwaves as a photoswitch, one can selectively activate NV centers in the nanodiamonds. This technique achieved 12 nm spatial resolution over a field-of-view of 35×35 μm^2 with only $\sim$ 90 s total imaging time. The fundamental limit of signal-to-noise is set by photon collection efficiency, photon emission rate, photon acquisition time, and signal contrast. One important drawback is that this technique cannot be applied to ensemble NV centers in bulk diamond samples because only four orientations are available.

Scanning probe microscopy offers the best spatial resolution among many real-space techniques. This technique was combined with NV centers for the first time in 2011 [101] and offered $<$ 10 nm spatial resolution in all three dimensions. Since then, this technique has been successfully applied to studying various condensed matter systems [168, 223, 250]. Like MRFM, the fundamental limitation on spatial resolution is set by the finite tip size or random drift of the tip. Tech-

nically, it is important to isolate the microscope from environmental noise such as temperature fluctuations, system drift, and air turbulence. There are mainly two drawbacks in this approach. One is that a scanning tip produces a large magnetic field as well as gradient, and it can perturb the magnetic sample of interest. The other is that since the gradient falls off rapidly as a function of standoff distance, it becomes more difficult to achieve nanometer-scale resolution for deep (> 1 μm) NV centers.

In transformed-space approach, images are constructed in a different space such as Fourier-space and frequency space. Examples techniques of this category are microwave field gradient [164, 190, 231], frequency encoding gradient, and phase encoding gradient [14, 190, 231].

Microwave field gradient can be used to encode the position of NV centers to the Rabi frequency. For example, if two NV centers located at x_1 and x_2 are driven with a spatially varying microwave field $B_1(x)$, these NV centers will experience coherent oscillations with different Rabi frequencies $\Omega(x_1)$ and $\Omega(x_2)$. When fluorescence from these two NV centers is collected simultaneously, it is difficult to distinguish them in real space. However, if microwave duration τ is varied, the fluorescence signal will be modulated as

$$f(\tau) = \cos(\Omega(x_1)\tau) + \cos(\Omega(x_2)\tau). \tag{1.19}$$

This idea was tested with a few proximal NV centers ($\sim$ 100 nm separation) in 2010 [231]. One fundamental limitation of this approach is the breakdown of the rotating wave approximation for a large microwave field. This idea is also implemented with nuclear spins in MRFM to demonstrate 10 nm resolution at 4.2 K [190]. More recently, it has been shown that combining with a quantum

sensing algorithm based on logarithmic search, one can estimate the position with error scaling at the Heisenberg limit [164].

Frequency encoding gradient technique employs a static, uniform magnetic field gradient applied across a sample. This is used as a slice sectioning method in the conventional magnetic resonance imaging. In NV frequency encoding, a strong static magnetic field gradient G is used to split the resonance frequencies of the NV centers

$$\Delta\omega(G; x_i) = \gamma G x_i, \tag{1.20}$$

where x_i is the position of the i-th NV center, thereby enabling selective fluorescence imaging of individual NV centers via continuous spin state driving with microwaves whose frequency is tuned to resonance frequencies of the NV center of interest. The spatial resolution is given by the width of the resonance peak

$$\delta x \propto \frac{1}{\gamma G T_2^*} \tag{1.21}$$

where T_2^* is the dephasing time of NV centers. It is noted that the resolution is not limited by the fluorescence wavelength because the NV position is mapped into the resonance frequency space. The fundamental concept of this technique is very similar to that of the SPM technique in real-space approach because both employ static magnetic field gradients. However, the main distinction that makes the two techniques fall into different categories is that in the frequency encoding gradient, microwave frequency is varied to acquire an image, whereas in the SPM technique, the probe itself is scanned in real-space.

Phase encoding gradient is also used in the conventional MRI. Under a pulsed magnetic field gradient, spins acquire position-dependent precession phase. By varying the gradient amplitude, one can construct an image in the Fourier-space

or 'k-space'.

$$f(k) = \sum_i \cos(kx_i), \tag{1.22}$$

where $k = \gamma G \tau$ is constructed from the gradient and encoding time τ. The spatial resolution is

$$\delta x = \frac{1}{2k_{\max}} = \frac{1}{2\gamma G_{\max} \tau_{\max}}, \tag{1.23}$$

where $G_{\max}$ and $\tau_{\max}$ are the maximum value of gradient and sequence time, respectively. In Chapter 4, nanoscale magnetic field imaging using via phase encoding gradient is presented. This technique was chosen for several reasons. First, the transformed-space approach offers multiplex advantage [82] and compressed sensing speed-up [44] under certain conditions (sparse NV centers, detector noise limited). Second, phase encoding gradient can be combined with a spin echo sequence, which extends the coherence time to T_2. Third, slow magnetic fluctuations introduce less noise to the spin echo sequence than to CW-ESR or Rabi sequence [231]. As discussed below, the electrical breakdown of air and coherence time of the spin limit the k-space.

Limits on magnetic field gradient techniques

A key technical challenge for demonstrating nanoscale magnetic imaging using phase encoding is to create a strong pulsed magnetic field gradient. There are mainly three methods: (i) ferromagnets, (ii) macroscopic ($\sim$ 1 cm) coil and (iii) microscopic ($\sim$ 1 μm) coil (microcoil). Ferromagnets can produce the strongest gradient (> 10 G nm^{-1}) at short length scale (< 100 nm) [61, 170, 225]; however, switching the gradients relies on the slow mechanical motion of the magnet. Thus, the distinct advantage of electromagnets (macroscopic coil and microcoil) compared to the ferromagnet approach is that the strong magnetic field gradient can be modulated rapidly in the

Table 1.3: Comparison of six approaches for nanoscale magnetic imaging (STED: stimulated emission depletion, DESM: deterministic emitter switch microscopy, SPM: scanning probe microscopy, MFG: microwave field gradient, FEG: frequency encoding gradient, PEG: phase encoding gradient) in terms of spatial resolution and fundamental limitations.

	Resolution	Limitations
Real-space		
STED [272]	2.4 nm	Doughnut beam intensity
DESM [48]	12 nm	Shot noise
SPM [102]	< 1 nm	Finite tip size & Standoff distance
Transformed-space		
MFG [231]	37 nm	Rotating wave approximation
FEG	~ 10 nm	Coherence time & Air breakdown
PEG [14]	3.5 nm	Coherence time & Air breakdown

time domain. The conventional macroscopic anti-Helmholtz coils used in nuclear magnetic resonance imaging can create $< 10^{-3}$ G nm^{-1} ($= 100$ T m^{-1}) over 100 mm [98, 156]. Microcoils offer intermediate performance ($10^{-3} - 10^{-1}$ G nm^{-1}) [72, 152]. Also, macroscopic coils and microcoils allow switching gradients at a fast rate. In the Fourier magnetic imaging experiment, the microcoil method was chosen mainly because it can be created directly on a diamond, which cancels system drift significantly. The fundamental limitation of the gradient strength is set by the electrical breakdown. A pair of thin wires is connected in series in an anti-Helmholtz configuration, which introduces a non-negligible electric potential difference ΔV between two wires separated by L, leading to a large electric field

$$E = \frac{\Delta V}{L} \sim \frac{IR}{L}, \tag{1.24}$$

where the electric current and resistance of the microcoil circuit are typically $I \sim 1$ A and $R \sim 10\ \Omega$, respectively. The electric field between them should not exceed the breakdown field (air: 3×10^6 V m^{-1}, diamond: 2×10^9 V m^{-1}, vacuum: 10^{18} V m^{-1}).

The gradient field needs to be turned off to avoid perturbation to the magnetic sample. Thus, the switching rate imposes a limit on the spin control timescale, which should be shorter than the coherence time. To investigate the performance of the microcoil, the maximum available gradient strength and current switching rate need to be measured. First, the maximum current that the microcoil can support is determined by measuring the temperature rise as a function of electric current. The switching rate of the gradient pulse is determined by measuring the rising Rabi signal contrast as a function of the delay between the initiation of d.c. gradient pulse and $\pi/2$ pulse. Using impulse response function theory, the 3 dB switching frequency is given by

$$f_{3\mathrm{dB}} = \frac{1}{2\pi T_r}(\ln(0.9) - \ln(0.1)), \tag{1.25}$$

where T_r is the $10-90$ % rise time. It is also important to estimate the limit of the spatial dynamic range of a magnetic field gradient. Let L be the length scale across which the strong gradient is produced. For a microcoil, L is determined by the separation between two wires. Since the gradient strength decreases quadratically as the coil separation increases ($dB/dx \sim I/L^2$), the electric current I should be increased quadratically $I \sim L^2$ to maintain the gradient. However, the current ramping speed is also limited by the switching bandwidth, $I \sim BW^{-1}$. Consequently, the bandwidth and dynamic range are related via $L \sim BW^{-\frac{1}{2}}$.

Objective of Fourier magnetic imaging experiment

The goal of Fourier magnetic imaging is to (i) demonstrate nanometer-scale magnetic field imaging using phase encoding gradient applied to NV sensors and (ii) show multiplex advantage and higher data acquisition rates with compressed sensing. It is also important to explore applications of strong magnetic field gradient using microcoils. The flexibility of microcoil design allows integration with microfluidic channels, Hall sensors, and MEMS [89, 153]. These advantages might make microcoils useful for many applications, ranging from atomic manipulation [73, 128], and actuation of a ferrofluid droplet [31], to manipulation of magnetotactic bacteria [154, 235] and DNA [52, 53].

1.2.3 Geometric phase magnetometry

The field dynamic range $B_{\max}$ is defined by the maximum detectable magnetic field. This section discusses three NV magnetometry protocols: (i) continuous-wave electron spin resonance (CW-ESR), (ii) Ramsey-interferometry, and (iii) Berry-interferometry.

Comparison of three magnetometry protocols

CW-ESR is an approach to drive a spin continuously via microwaves. The frequency of the microwave is varied to find a resonance. A d.c. magnetic field can be measured as a shift of the resonance frequency. The linewidth of the resonance peak is given by the microwave amplitude, or Rabi frequency Ω. For a small Rabi frequency, the linewidth is fundamentally limited by the dephasing time T_2^*. Thus, dynamic range is thus given by

$$B_{\max} \propto \Omega. \tag{1.26}$$

Similarly, the sensitivity also depends on the Rabi frequency

$$\eta \propto \Omega. \tag{1.27}$$

As a result, there arises a trade-off between the dynamic range and sensitivity

$$\eta \propto B_{\max}. \tag{1.28}$$

The upper limit of Rabi frequency is set fundamentally by the rotating wave approximation ($\Omega/D \ll 1$), where $D = 2.87$ GHz is the zero field splitting, and technically by a microwave driving circuit ($\Omega \sim 100$ MHz is achievable relatively easily). The lower limit is coming from the dephasing time T_2^*.

Ramsey is an alternative method for detecting a d.c. magnetic field. It employs an interferometry-based sensing protocol. A $\pi/2$ pulse tips the sensor spin on the equator. The spin acquires a precession phase proportional to the external magnetic field and interaction time: $\phi \propto \gamma BT$. However, because of the periodicity of phase, the dynamic range that one can determine without modulo 2π

phase ambiguity is limited to

$$B_{\max} \propto \frac{1}{T}. \tag{1.29}$$

In this approach, the sensitivity is also dependent on the interaction time

$$\eta \propto \frac{1}{T^{\frac{1}{2}}}. \tag{1.30}$$

Thus, the Ramsey approach also exhibits a trade-off between the dynamic range and sensitivity

$$\eta^2 \propto B_{\max}. \tag{1.31}$$

The interaction time is fundamentally upper limited by dephasing time T_2^*. By use of a spin echo sequence or dynamical decoupling sequence, one can extend coherence time. However, the spin is not sensitivity to d.c. magnetic fields. The lower limit is usually set by the speed of pulse shaping instruments. The quantum phase estimation algorithm [36, 191, 267] or quantum metrology [35, 96] can extend dynamic range and resolve the trade-off; however, they require either additional overhead resource time or long-lived multi-particle non-classical states.

Berry – In this thesis, a new approach for d.c. magnetic field sensing via geometric phase is introduced (Chapter 5). In particular, Berry phase is considered. Unlike the above-mentioned two, this approach has three control parameters: Rabi frequency Ω, winding number N and interaction time T. The 2π phase ambiguity is unwrapped by a nonlinear dependence of the signal on the external magnetic field. Sensitivity and dynamic range are decoupled via the three parameters.

$$B_{\max} \propto \Omega N^{\frac{1}{2}} T^0. \tag{1.32}$$

$$\eta \propto \frac{\Omega T^{\frac{1}{2}}}{N}. \tag{1.33}$$

Limits on dynamic range of geometric phase magnetometry

Since three control parameters are used in geometric phase magnetometry, there are several fundamental limits that need to be discussed. One important assumption of dynamic range enhancement and decoupling of sensitivity from dynamic range is adiabaticity condition

$$A \sim \frac{N}{\Omega T} \ll 1. \tag{1.34}$$

To satisfy this condition, one need to choose $N \ll \Omega T$. The breakdown of rotating wave approximation and the geometric phase coherence time T_{2g} set fundamental limits on Rabi frequency $\Omega \ll D$ and interaction time $T < T_{2g}$.

Objective of geometric phase magnetometry experiment

The goal of this experiment is to show (i) extension of dynamic range and (ii) decoupling of sensitivity from dynamic range. One scientific question that needs to be investigated is how the geometric phase coherence time depends on A. This will give an important insight in understanding the ultimate limit of magnetic field sensitivity in the non-adiabatic regime.

1.3 Thesis Outline

This thesis presents a series of quantum manipulation experiments using NV centers of various concentrations for improving the performance of magnetic field sensing in three different directions (Fig. 1-1). Chapter 2 summarizes important concepts in NV magnetometry, which form the basis for the following chapters.

The first direction, presented in Chapter 3, is the enhancement of the field-of-view via a parallel manipulation and readout of an ensemble of NV centers [150]. The diamond sample used in this demonstration had an ensemble of NV centers implanted in a 2D layer structure. Wide-field laser illumination as well as CCD-based parallel detection enable fluorescence imaging of the NV centers. By CW-ESR using homogeneous microwave irradiation, one can use the NV centers as a local magnetic probe to map the magnetic field pattern created by the magnetized sample of interest. The wide-field magnetic imaging offers approximately x100 larger field-of-view along one dimension compared to the confocal laser scanning microscopy with a given measurement time. Thus, it is a powerful tool for imaging various natural magnetic systems. In particular, this technique is applied to the study of living magnetotactic bacteria.

Described in Chapter 4 is the second direction, improvement of spatial resolution via phase encoding of multiple NV centers using strong pulsed magnetic field gradients [14]. The diamond sample contains multiple NV centers confined in a nanoscale diamond pillar prepared by e-beam lithography and reactive ion etching. Under magnetic field gradients applied during a Hahn-echo sequence, the NV centers acquire a position-dependent phase. When the gradient strength is swept, the information about the location of the NV centers as well as the local magnetic field is mapped onto Fourier space. This phase encoding technique provides an approximately 100-fold improvement in spatial resolution compared to the optical diffraction limit. Taking the advantage of sparse NV sample, compressed sensing demonstrates additional 10-fold speed-up in nanoscale imaging and sensing.

Chapter 5 introduces a new approach of geometric spin control for the third direction – high dynamic range magnetometry (K. Arai *et al.* in preparation). In this experiment, a single NV center acquires geometric phase as a result of off-resonant microwave fields whose phase is varied linearly in time. The nonlinear dependence

of geometric phase on the external magnetic field extends the dynamic range by approximately 100 times compared to the conventional dynamic phase approach. The new geometrical control parameters also allow decoupling of sensitivity and field dynamic range. Furthermore, the geometric manipulation technique is used to study the robustness of geometric phase against the environmental noise, which has not been discussed extensively in the literature.

Finally, Chapter 6 concludes the thesis by discussing the outlook of these three techniques for a broad range of other quantum applications.

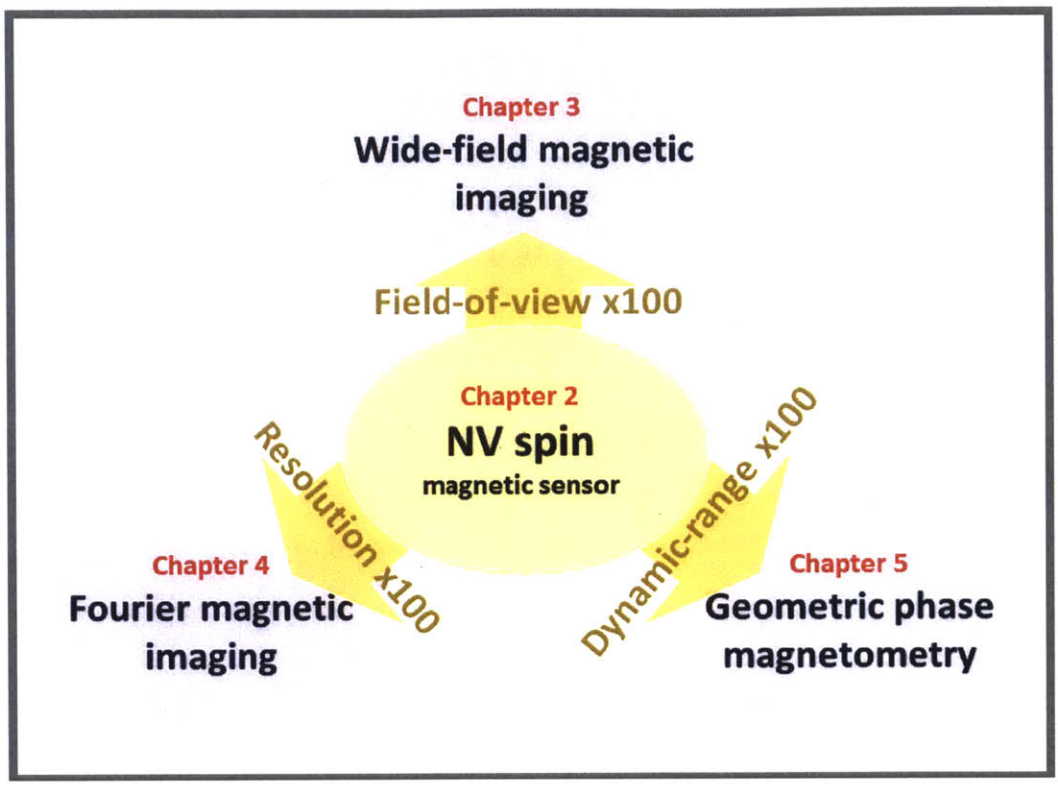

Figure 1-1: Description of this thesis. The central theme is the development of high precision magnetic field sensing and imaging techniques via quantum manipulation of electronic spins associated with NV centers in diamond. Chapter 2 introduces NV spins as a high-precision magnetic field sensor (yellow circle) and explains previous work on improving the sensitivity. The main body consists of three experimental demonstrations (blue circles), which improve the performance of NV magnetic field sensing in three directions: field-of-view (Chapter 3), spatial resolution (Chapter 4), and field dynamic range (Chapter 5). Chapter 6 discusses the potential and new movements of combining these techniques for other quantum applications.

Chapter 2

The Nitrogen-Vacancy Center in Diamond

Unique aspects of the NV spin system include the feasibility of NV preparation in large two-dimensional arrays with flexible concentration and nanometer-scale precision [24, 194, 259], coherent addressability enabled by microwave and static magnetic fields [50, 125, 199], and availability of long spin coherence as well as photo-stability even under ambient conditions [20, 22, 123]. Among many solid-state spin systems, NV centers thus have been gaining prominence as a leading platform in many branches of modern quantum technologies [51], ranging from nanoscale sensing [68, 145] and imaging [102, 150, 250] to quantum computation [28, 118, 189, 255] and simulation [9, 43, 131]. This section provides an overview of NV properties.

2.1 Crystallographic Structure and Charge States

The NV center is one of numerous diamond defects [280] consisting of a nearest-neighbor pair of a substitutional nitrogen atom and a lattice vacancy (Fig. 2-1). Depending upon the relative positions of the nitrogen atom and vacancy, the sym-

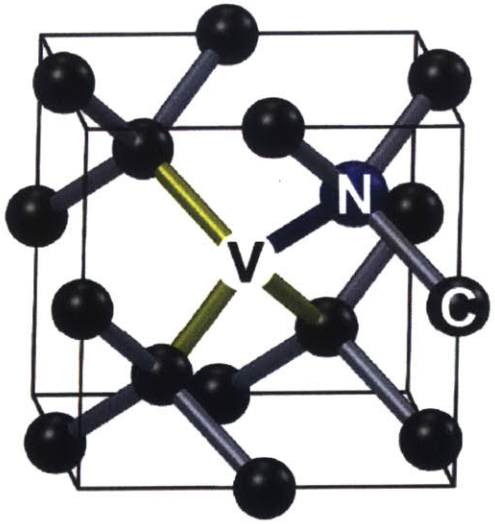

Figure 2-1: The structure of diamond crystal with an NV center. The diamond belongs to the $Fd\bar{3}m$ space group with a lattice constant of $a = 3.567$ Å at 300 K. The bond angle between the carbon (C) atoms is 109.28°. The NV center consists of a substitutional nitrogen atom (N) adjacent to a vacancy (V) in the diamond lattice. The direction along the nitrogen atom and the vacancy defines the symmetry axis of the NV center (blue rod). The NV center can primarily take one of two electric charge states, the neutral NV^0 and the negative NV^- [163]. Throughout this work the negatively charged state is considered.

metry axis can lie along one of four possible crystallographic orientations within the diamond lattice. This NV symmetry axis gives the quantization axis of the spin states. Usually, these four classes of NV centers have an equal probability of abundance. However, some diamonds grown with a chemical vapor deposition (CVD) method have preferential orientation [204].

The NV center exists in either of the neutral (NV^0) and negatively-charged (NV^-) states. The three nearest-neighbor carbon atoms and the nitrogen atom provide totally five electrons to form the NV^0 state. If the NV center captures one more electron from another defect in the lattice, it becomes the NV^- state[1]. As described below, the NV^- state presents many useful properties, and thus is used throughout this work.

2.2 Diamond Preparation

It is often necessary to control the spin concentration of diamond samples depending on the application. There are mainly two widely used techniques to create NV centers with controllable concentrations: CVD and nitrogen ion implantation.

The CVD is the primary synthesis technique for high-density NV diamond samples ([NV]$\sim 10^{15}$-10^{18} cm^{-3}) [3, 47, 248]. In a CVD chamber filled with hydrogen gas, a diamond crystal grows from methane at a growth speed of ~ 1 nm/s. When nitrogen gas is injected during the growth, the crystal incorporates nitrogen impurities, whose density can be controlled with high precision. This technique can also introduce other chemical impurities [2, 78, 160]. In this process, only less than 1% of nitrogen impurities meet vacancies and become NV centers. The conversion efficiency is limited by the small abundance of natural vacancies. Implantation with other atoms (H, C)

[1]A study of charge state conversion by ionization has revealed that the fidelity of charge state readout reaches 99% [230]. Thus, the charge state dynamics has recently become an important research topic.

or irradiation with electrons increases the conversion efficiency since these particles create more vacancies in the diamond lattice. Recently, researchers have succeeded in confining NV centers in a nanometer-scale layer by introducing nitrogen gas for only a short period of time during growth process (delta-doping) [194].

Nitrogen ion implantation [186, 200] is used largely to prepare relatively low NV density samples ([NV]$\sim$ 10^6-10^{11} cm^{-2}). An undoped CVD diamond is often chosen as a substrate. After creating nitrogen defects, an annealing process follows to mobilize vacancies. The nitrogen implantation energy and dose determine the NV depth and density, respectively. NV centers can be created only a few nanometers from the surface [63]. Such shallow NV centers are particularly useful for nanoscale magnetic resonance sensing and imaging of surface nuclear spins [63, 229, 245]. The implantation technique also provides nanometer-scale precision in the lateral direction [192, 197] when combined with a focused ion beam [178] or an implantation mask fabricated on the diamond by e-beam lithography [201].

2.3 Electric and Magnetic Dipole Transitions

The negatively charged NV state possesses six electrons, of which two unpaired electrons form a ground state spin-triplet (see Fig. 2-2) [217]. The $|0\rangle$ and $|\pm 1\rangle$ Zeeman sublevels are split by $D = 2\pi \times 2.87$ GHz due to spin-spin interaction. In an external magnetic field B_z along the quantization axis, the energy level of the $|\pm 1\rangle$ states shift by $\pm\hbar\gamma B_z$, where $\hbar$ is the Planck's constant and $\gamma = 2\pi \times 2.8$ MHz G^{-1} is the gyromagnetic ratio of NV electronic spin. Thus, a two-level system can be defined by the $|0\rangle$ and either of the $|\pm 1\rangle$ states. The ground state Hamiltonian is given by

$$H/\hbar = DS_z^2 + \gamma \boldsymbol{B} \cdot \boldsymbol{S}, \tag{2.1}$$

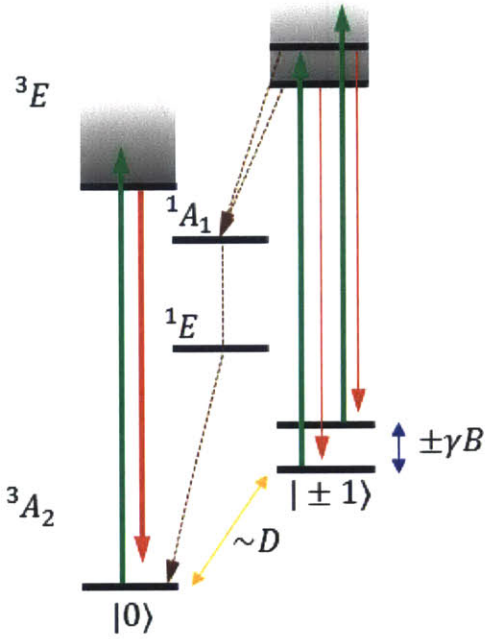

Figure 2-2: NV center energy level diagram. The ground state of the NV center is a spin-triplet with a $D = 2\pi \times 2.87$ GHz zero-field splitting between the $|0\rangle$ and $|\pm 1\rangle$ spin states [163]. An applied magnetic field B defines a quantization axis and Zeeman-splits the $|\pm 1\rangle$ states by $\pm\gamma B$ (blue arrow), where $\gamma = 2\pi \times 2.8$ MHz G^{-1} is the gyromagnetic ratio of the NV center. Under optical excitation at 532 nm (green arrows), the NV center undergoes spin-state-preserving transitions between the electronic ground ($^3A_2$) and excited states (^3E), emitting fluorescence in the 640-800 nm band (red arrows) with a life time of $\sim$ 13 ns. There is also a non-radiative decay pathway (brown arrows) from the $|\pm 1\rangle$ excited states to the $|\pm 0\rangle$ ground state via metastable singlet states ($^1A_1$ and ^1E) with a lifetime of $\sim$ 300 ns [5, 221, 222]. The splitting between the two metastable states is 1043 nm (ZPL). Under continuous green laser illumination, the NV spin is eventually polarized to the $|0\rangle$ state. The level of polarization is typically $\sim$ 80 % and can reach $\sim$ 95 % under certain conditions [255].

where $\boldsymbol{B} = (B_x, B_y, B_z)$ is the magnetic field vector and $\boldsymbol{S} = (S_x, S_y, S_z)$ are the spin 1 operators given by

$$S_x = \frac{1}{\sqrt{2}} \begin{pmatrix} 0 & 1 & 0 \\ 1 & 0 & 1 \\ 0 & 1 & 0 \end{pmatrix}, \quad S_y = \frac{1}{\sqrt{2}} \begin{pmatrix} 0 & -i & 0 \\ i & 0 & -i \\ 0 & i & 0 \end{pmatrix}, \quad S_z = \begin{pmatrix} 1 & 0 & 0 \\ 0 & 0 & 0 \\ 0 & 0 & -1 \end{pmatrix}. \tag{2.2}$$

Magnetic fields along the x and y axes introduce spin state mixing, leading to a reduction of fluorescence contrast and intensity [146, 251, 263].

Experimentally, microwaves and green lasers are used to manipulate and readout the ground states. Microwave fields induce magnetic dipole transitions between these ground states. Optical illumination causes electric dipole transitions between the ground and excited states, entailing spontaneous emission [57]. The zero-phonon line (ZPL) of the electric dipole transition appears at 637 nm. At room temperature, this line accompanies a broad phonon-sideband from 640 nm to 800 nm. Another important property of NV centers is a non-radiative decay channel from the $|\pm 1\rangle$ excited states to the $|0\rangle$ ground state, which enables initialization and readout of spin state via continuous laser excitation and spin-state-dependent fluorescence detection, respectively.

2.4 Magnetic Impurities

In a natural diamond sample, there are many other spin impurities, such as ^{13}C, ^{14}N and ^{15}N. In high sensitivity magnetometry, these are the main noise source, while in quantum computation, these can be used as a qubit memory or reporters. The most abundant carbon isotope is ^{12}C (98.9 %, $I = 0$), where I is the nuclear spin. The second abundant is ^{13}C (1.1 %, $I = 1/2$). If there are ^{13}C atoms near an NV center, they further split the NV energy levels due to a dipolar hyperfine

coupling [83, 94]. Oftentimes, the nitrogen density is not as large as that of carbon, however, the electronic spin of nitrogen defects (P1 center) plays an important role in decoherence [21, 25] because the electron gyromagnetic ratio is three-orders-of-magnitude larger than the nuclear gyromagnetic ratio. Additionally, the nitrogen nuclear spin of NV center itself also affects the NV energy levels via hyperfine coupling. The most abundant nitrogen isotope is ^{14}N (99.6 %, $I = 1$) and the second is ^{15}N (0.4 %, $I = 1/2$). Their concentrations can be easily modified during the NV diamond preparation process [211]. For ^{14}N, the NV center Hamiltonian is written as

$$H/\hbar = DS_z^2 + \gamma B S_z + \boldsymbol{S} \cdot \boldsymbol{A} \cdot \boldsymbol{I} + P I_z^2 - \gamma_N \boldsymbol{B} \cdot \boldsymbol{I}, \tag{2.3}$$

where $P = -2\pi \times 4.95$ MHz [115, 241] is the quadrupole splitting constant, $\boldsymbol{A} = (A_\parallel, A_\perp)$ is the hyperfine coupling tensor with $A_\parallel = -2\pi \times 2.16$ MHz [241] and $A_\perp = -2\pi \times 2.7$ MHz [83], and γ_N is the ^{14}N nuclear gyromagnetic ratio.

2.5 Characteristic Timescales

The coherence time of NV spins has been one of the most intensively studied research topics since coherent manipulation of NV centers is a key challenge for many applications. There are three important time scales T_2^*, T_2, and T_1, each being associated with dephasing, decoherence, and relaxation. The spin impurities (^{13}C and P1) discussed in Section 2.4 are generally randomly polarized and create magnetic field fluctuations at the location of an NV center. For ensemble NV measurements, this leads to an inhomogenous broadening of transitions. For single NV measurements, this is equivalent to randomly time-varying field (ergodic theorem). In either case, the NV spins subject to the magnetic field fluctuations lose the coherent information about the relative phase between the two states (dephasing). T_2^* is the time scale

that characterizes an exponential decay due to dephasing. In the Bloch sphere picture (Appendix A.2), the dephasing process is regarded as the reduction of the Bloch vector in the (x, y) direction. The main source of dephasing is slow fluctuations. As explained in Section 2.6, when an echo operation is applied, these slow fluctuations can be removed. Consequently, the coherence time improves significantly to T_2. The relaxation is depicted as the reduction of the Bloch vector in the z direction. The exponential decay of polarization is characterized by T_1 time scale. The spin relaxation is primarily caused by an interaction with lattice photons (spin-lattice relaxation). Thus, T_1 relaxation time depends strongly on the lattice temperature.

2.6 NV Characterization Protocols

There are five steps for characterizing the basic properties of an NV center. The first step is to determine the resonance frequency of the NV center using continuous wave electron spin resonance (CW-ESR). In CW-ESR, the fluorescence from the NV center is collected continuously during the simultaneous green laser and microwave excitation (Fig. 2-3a). The microwave frequency is varied across the resonance. When the microwave frequency is on resonance with the transition frequency, the population transfers between the two states and the fluorescence decreases. Once the transition frequency is determined, the next step is to calibrate the microwave pulse width via Rabi nutation experiment as shown in Fig. 2-3b. When microwave pulse width is increased, the NV center experiences coherent population oscillation between the two states. The π pulse duration is defined at the point which gives the first minimum fluorescence. The $\pi/2$ pulse duration is half of π pulse duration. The third step is to determine the dephasing time using a Ramsey interferometry sequence (Fig. 2-3c). A spin echo sequence (Fig. 2-3d) can remove dephasing caused by slow fluctuations because an additional π pulse in the middle of the Ramsey sequence flips the spin

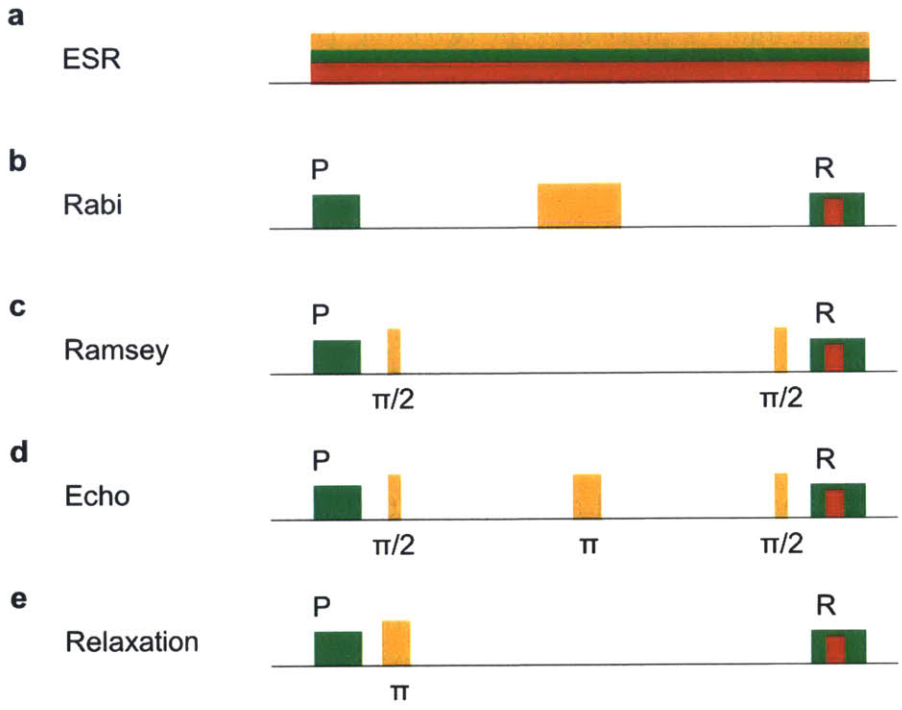

Figure 2-3: Pulse sequences of NV characterization protocols. Green laser illumination (green box), microwave excitation (yellow box), and fluorescence detection (red box) are illustrated. In green pulses, P and R stand for polarization and readout pulse, respectively. **a**, ESR. The microwave frequency is swept and resonance frequency is measured. **b**, Rabi nutation. The microwave pulse width is varied and π and $\pi/2$ pulses are determined. **c**, Ramsey interferometry. The time interval between two $\pi/2$ pulses is varied and T_2^* dephasing time is characterized. **d**, Spin echo. The time interval between microwave pulses is varied to measure T_2 decoherence time. **e**, Relaxation. The time interval between π pulse and readout pulse is varied to measure T_1 relaxation time.

state, which effectively reverses the time evolution. However, high frequency noise still causes decoherence. The fourth step is to measure the characteristic time scale T_2 by sweeping the interaction time interval. Finally, a pulse sequence shown in Fig. 2-3e can be employed to measure the relaxation time. The NV center is first prepared in the $m_s = 0$ state, and a π pulse flips the two level. During the time interval between the π pulse and readout pulse, the NV center experiences relaxation.

2.7 Magnetic Field Sensing using NV Centers

In this thesis, magnetometry is the primary application of the coherent NV spin control. The basic principle behind the NV magnetometry is to measure the energy splitting between the two ground states [19, 176, 249]. One of the most important figures-of-merit is the magnetic field sensitivity. The sensitivity measures the minimum detectable field in a unit time. Let $P(B)$ be the NV magnetometry signal as a function of an external field B. Then the general expression of the sensitivity is [249]

$$\eta = \frac{\sigma_B}{|dP/dB|_{\max}}\sqrt{T_{\mathrm{m}}}, \tag{2.4}$$

where T_{m} is the total measurement time, and σ_B is the measurement uncertainty. The signal form depends on which of the magnetometry schemes is employed.

There are mainly three schemes to measure external magnetic fields: (i) CW-ESR, (ii) Ramsey, and (iii) spin echo. CW-ESR is used to measure d.c. magnetic fields. When a d.c. magnetic field B is applied, the resonance frequency shifts by $\delta f = (2\pi)^{-1}\gamma B$, and the CW-ESR magnetometry signal is given by

$$P = I\left[1 - \alpha\mathcal{F}\left(\frac{f_0 + \delta f}{\Gamma}\right)\right], \tag{2.5}$$

where I is the fluorescence emission rate, $\mathcal{F}$ is a function characterizing the resonance lineshape, α is the signal contrast, Γ is the full-width-half-maximum linewidth of the resonance peak, and f_0 is the initial resonance frequency in the absence of the external magnetic field to be measured. The resonance lineshape is a Voigt function due to a competition between the natural decay (Lorentzian) and microwave power broadening (Gaussian). The best magnetic field sensitivity is given by

$$\eta \propto \frac{1}{\alpha\sqrt{\beta}} \frac{1}{\sqrt{T_2^*}}, \tag{2.6}$$

where β is the number of photons collected per measurement. In Ramsey magnetometry, the NV center acquires an additional phase due to a d.c. external field present during the interaction time T between the $\pi/2$ pulses. The Ramsey signal is

$$P = \alpha \cos(\gamma B T) \tag{2.7}$$

and the best sensitivity is again given when $T \sim T_2^*$ as in Eq. (2.6). In spin echo magnetometry, since the NV population is flipped by the π pulse, the NV center is most sensitive to an a.c. magnetic field whose frequency matches the echo interaction time T between the two $\pi/2$ pulses and phase is locked to the sequence $B(t) = B\sin(2\pi t/T)$. The spin echo magnetometry signal is given by Eq. (2.7). The time scale that gives the best sensitivity is replaced by $T \sim T_2$.

$$\eta \propto \frac{1}{\alpha\sqrt{\beta}} \frac{1}{\sqrt{T_2}}. \tag{2.8}$$

Numerous works have investigated various approaches to improve the signal contrast α [92, 179, 204], photon collection efficiency β [55, 151], and coherence times T_2^* and T_2 [22, 60, 203].

Table 2.1: Description of three experiments in terms of three perspectives: number of sensor spins, ground state driving scheme, and achieved performance improvement.

	Experiments	Number of spins	Scheme	Performance
Chapter 3	Wide-field	Ensemble	Longitudinal	Field of view
Chapter 4	Fourier	Multiple	Transverse	Resolution
Chapter 5	Geometric phase	Single	Hybrid	Dynamic range

2.8 Interrelation between Three Experiments

To clarify the relation between the experiments, Table 2.1 provides the summary of each experiment classified in terms of the number of sensing spins, control schemes, and achieved performance improvement.

Number of spins It is of importance to choose a diamond sample with a proper concentration of spins depending on target applications.

Ensemble spins – Over the past few years, researchers have developed ensemble-NV-spin control techniques for exquisite demonstrations, ranging from the nano-scale sensing of multiple nuclear spin species [64] to magnetic imaging of living bacteria [150] and meteorites [90] across a large field-of-view.

Multiple spins – More recently, a smaller ensemble, or multi-spin system, has also gained prominence since such spin system is crucial for high-spatial resolution magnetic imaging [14, 101, 174] as well as scalable quantum simulation and information processing [70, 189, 278].

Single spin – At the other end of the spectrum, investigations on the behavior

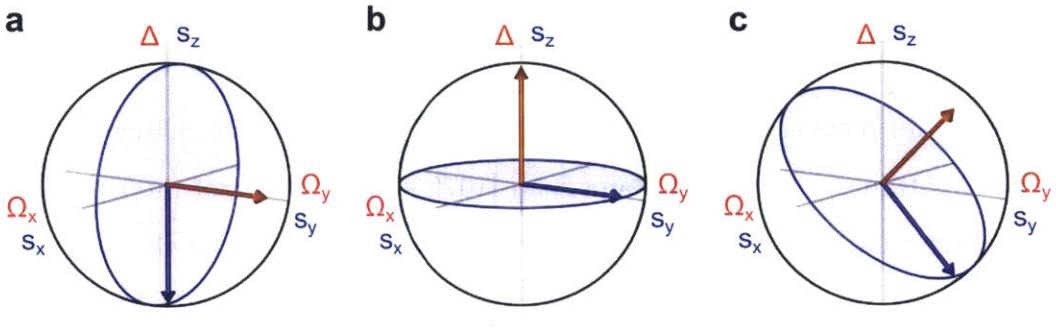

Figure 2-4: Three NV center driving schemes. Overlaid are the Bloch vector $\boldsymbol{s} = (s_x, s_y, s_z)$ (blue arrow) on the Bloch sphere and the Larmor vector $\boldsymbol{R}$ (orange arrow) on the control parameter space ($\Omega_x = \Omega\cos\rho, \Omega_y = \Omega\sin\rho$, $\Delta = \gamma B$). **a**, Polar rotation. A microwave field mixes the ground state population, corresponding to the rotation of the polar angle $\alpha = \arcsin\sqrt{s_x^2 + s_y^2}$ of the Bloch vector. For CW-ESR, the average of population is measured. When the microwave is on resonant $\Delta = 0$, the average population is equally distributed between two levels. **b**, Azimuthal rotation. The spin undergoes free precession on the equator under a static field, resulting in the change of the azimuthal angle $\beta = \arctan(s_y/s_x)$. **c**, Hybrid rotation. When a static field and a microwave field are combined, the spin experiences off-resonant driving. The angle between the Bloch vector and Larmor vector depends on the initial condition. Shown here is an example of $\boldsymbol{s} \perp \boldsymbol{R}$.

of individual spins have also opened new directions [40, 76, 91]. Examples include the creation of entangled states [255], realization of universal quantum gates [283], test of quantum estimation algorithms [191, 267], and detection of a single electric charge [68] or nuclear spin [245].

Driving scheme Quantum manipulation protocols explored in this thesis can be classified into the following three regimes (Fig. 1-3):

Polar rotation – A microwave excitation pulse drives the spin state. When the applied microwave frequency is in resonance with either of the $|0\rangle \leftrightarrow |\pm 1\rangle$ state transitions, some of the NV state population is transferred from the $|0\rangle$ optically-pumped state to a superposition state, and consequently, the fluorescence rate

changes. This polar rotation picture describes continuous wave electron spin resonance (CW-ESR) [105] and Rabi experiments [212].

Azimuthal rotation – Alternatively, one can exploit interferometry techniques, such as Ramsey [216] and Hahn-echo [107]. The key idea of interferometry is to make a superposition state between two ground states, and then let the spin acquire relative phase during free precession. Additional external fields may be used to modulate the relative phase. Finally, a microwave $\pi/2$ pulse projects the phase onto a population difference.

Hybrid rotation – As a combination of the above-mentioned two, off-resonant microwave pulses make the spin evolve in a more complicated fashion. This scheme can be employed in various situations, for example, when the spin needs to be parked at a particular point on the Bloch sphere (spin locking [114]), and when the spectral bandwidth of the control sequence needs to be engineered (rotary echo [237]).

2.9 Summary of Concepts and Related Theses

There are a collection of theses about many aspects of NV diamond research. In Table 2.2 and 2.3, I summarize important concepts of NV spin control for precision magnetic sensing and some of the related theses.

Table 2.2: Some of the related theses.

Year	Author	Supervisor	Institution	
2006	Childress, L.	Lukin, M.	Harvard University	[49]
	Popa, L.	Wrachtrup, J.	University of Stuttgart	[207]
2009	Jiang, L.	Lukin, M.	Harvard University	[126]
	Steiner, P.	Wrachtrup, J.	University of Stuttgart	[240]
2010	Maze, J.	Lukin, M.	Harvard University	[175]
2011	Acosta, V.	Budker, D.	UC Berkeley	[4]
	Togan, E.	Lukin, M.	Harvard University	[254]
2012	De Lange, G.	Kouwenhoven, L.	Delft University of Technology	[59]
	Neumann, P.	Wrachtrup, J.	University of Stuttgart	[187]
	Van der Sar, T.	Kouwenhoven, L.	Delft University of Technology	[262]
2013	Pham, L.	Walsworth, R.	Harvard University	[202]
2014	Aiello, C.	Cappellaro, P.	MIT	[7]
	Chu, Y.	Lukin, M.	Harvard University	[54]
	DeVience, S.	Walsworth, R.	Harvard University	[63]
	Dolde, F.	Wrachtrup, J.	University of Stuttgart	[69]
	Grinolds, M.	Yacoby, A.	Harvard University	[102]
	Maurer, P.	Lukin, M.	Harvard University	[173]
	Ohno, K.	Awschalom, D.	UC Santa Barbara	[193]
	Shields, B.	Lukin, M.	Harvard University	[230]
	Waldherr, G.	Wrachtrup, J.	University of Stuttgart	[266]
	Yao, N.	Lukin, M.	Harvard University	[277]
2015	Blok, M.	Hanson, R.	Delft University of Technology	[33]
	Hirose, M.	Cappellaro, P.	MIT	[121]

Table 2.3: Summary of important concepts.

Section	Concept	Thesis
2.1	Crystallographic structure	[4, 175]
	Charge states	[230, 266]
2.2	CVD	[194]
	Implantation	[194]
2.3	Energy level	[4, 175]
	Optical properties	[54, 254, 262]
2.4	Carbon impurity	[49, 126, 187, 207, 266]
	Nitrogen impurity	[59, 266, 277]
2.5	Characteristic timescales	[49, 59, 202, 207]
2.6	Characterization protocols	[49, 202, 207]
2.7	Magnetometry sensitivity	[59, 175, 202]
	Contrast enhancement	[202]
	Coherence improvement	[59, 63, 202]
	Photon collection	[202, 262]
2.8	Hybrid rotation	[7, 121]
	Superresolution -SPM	[102]
	Superresolution -STED	[173]
	Electric field sensing	[69]
	Temperature sensing	[173]
	Coherent coupling	[33, 50, 69, 126, 187, 240, 277]
	Quantum estimation	[33, 266]

Chapter 3

Wide-Field Magnetic Imaging

Magnetic imaging is a powerful tool for probing biological and physical systems. However, existing techniques either have poor spatial resolution compared to optical microscopy and are hence not generally applicable to imaging of sub-cellular structure (for example, magnetic resonance imaging [157]), or entail operating conditions that preclude application to living biological samples while providing submicrometer resolution (for example, scanning superconducting quantum interference device microscopy [88], electron holography [75] and magnetic resonance force microscopy [61]). In this chapter, we demonstrate magnetic imaging of living cells (magnetotactic bacteria) under ambient laboratory conditions and with sub-cellular spatial resolution (400 nanometers), using an optically detected magnetic field imaging array consisting of a nanometer-scale layer of nitrogen-vacancy color centers implanted at the surface of a diamond chip. With the bacteria placed on the diamond surface, we optically probe the nitrogen-vacancy quantum spin states and rapidly reconstruct images of the vector components of the magnetic field created by chains of magnetic nanoparticles (magnetosomes) produced in the bacteria. We also spatially correlate these magnetic field maps with optical images acquired in the same apparatus. Wide-field microscopy

allows parallel optical and magnetic imaging of multiple cells in a population with submicrometer resolution and a field of view in excess of 100 micrometers. Scanning electron microscope images of the bacteria confirm that the correlated optical and magnetic images can be used to locate and characterize the magnetosomes in each bacterium. Our results provide a new capability for imaging bio-magnetic structures in living cells under ambient conditions with high spatial resolution, and will enable the mapping of a wide range of magnetic signals within cells and cellular networks [109, 205].

3.1 Introduction

3.1.1 Wide-field NV magnetometry

Nitrogen-vacancy color centers in diamond enable nanometer-scale magnetic sensing and imaging under ambient conditions [19, 176]. As recently shown using a variety of methods [168, 205, 242], NV centers within room-temperature diamond can be brought into close proximity (a few nanometers) of magnetic field sources of interest while maintaining long NV electronic spin coherence times (of the order of milliseconds), a large (about one Bohr magneton) Zeeman shift of the NV spin states, and optical preparation and readout of the NV spin. Recent demonstrations of NV-diamond magnetometry include high-precision sensing and submicrometer imaging of externally applied and controlled magnetic fields [151, 168, 205, 242]; detection of electron [112] and nuclear [50, 169, 239] spins; and imaging of a single electron spin within a neighboring diamond crystal with $\sim$ 10 nm resolution [100]. However, a key challenge for NV-diamond magnetometry is submicrometer imaging of spins and magnetic nanoparticles located outside the diamond crystal and within a target of interest. Here we present the first such demonstration of NV-diamond imaging of the

magnetic field distribution produced by a living biological specimen.

3.1.2 Magnetotactic bacteria

Magnetotactic bacteria (MTB) are of considerable interest as a model system for the study of molecular mechanisms of biomineralization [81, 113] and have often been used for testing novel biomagnetic imaging modalities [75, 147, 209, 210]. MTB form magnetosomes, membrane-bound organelles containing nanoparticles of magnetite (Fe_3O_4) or greigite (Fe_3S_4), that are arranged in chains with a net dipole moment, allowing the bacteria to orient and travel along geomagnetic field lines (magnetotaxis) [81, 113]. Magnetic nanoparticles produced in the magnetosomes are chemically pure, single-domain monocrystalline ferrimagnets, with species-specific morphologies and strikingly uniform size distributions [81, 113]. These features, combined with the ease of biofunctionalization and aqueous dispersion afforded by the magnetosome membrane [172], make synthesis of magnetic nanoparticles by MTB an attractive research area for various biomedical applications[81, 172], including magnetic labeling, separation and drug delivery, as well as local hyperthermic cancer treatment and contrast enhancement in magnetic resonance imaging. For the NV-diamond bio-magnetic imaging demonstrations presented here (see Fig. 3-1), we used *Magnetospirillum magneticum* AMB-1, an MTB strain that forms magnetic nanoparticles with cubo-octahedral morphology and an average diameter of $\sim$ 50 nm. (Figure 3-1c shows a transmission electron microscopy image exhibiting the characteristic morphology of *M. magneticum* AMB-1, including a chain of magnetic nanoparticles distributed over the length of the cell. Gaps between nanoparticles are common in AMB-1 [71].)

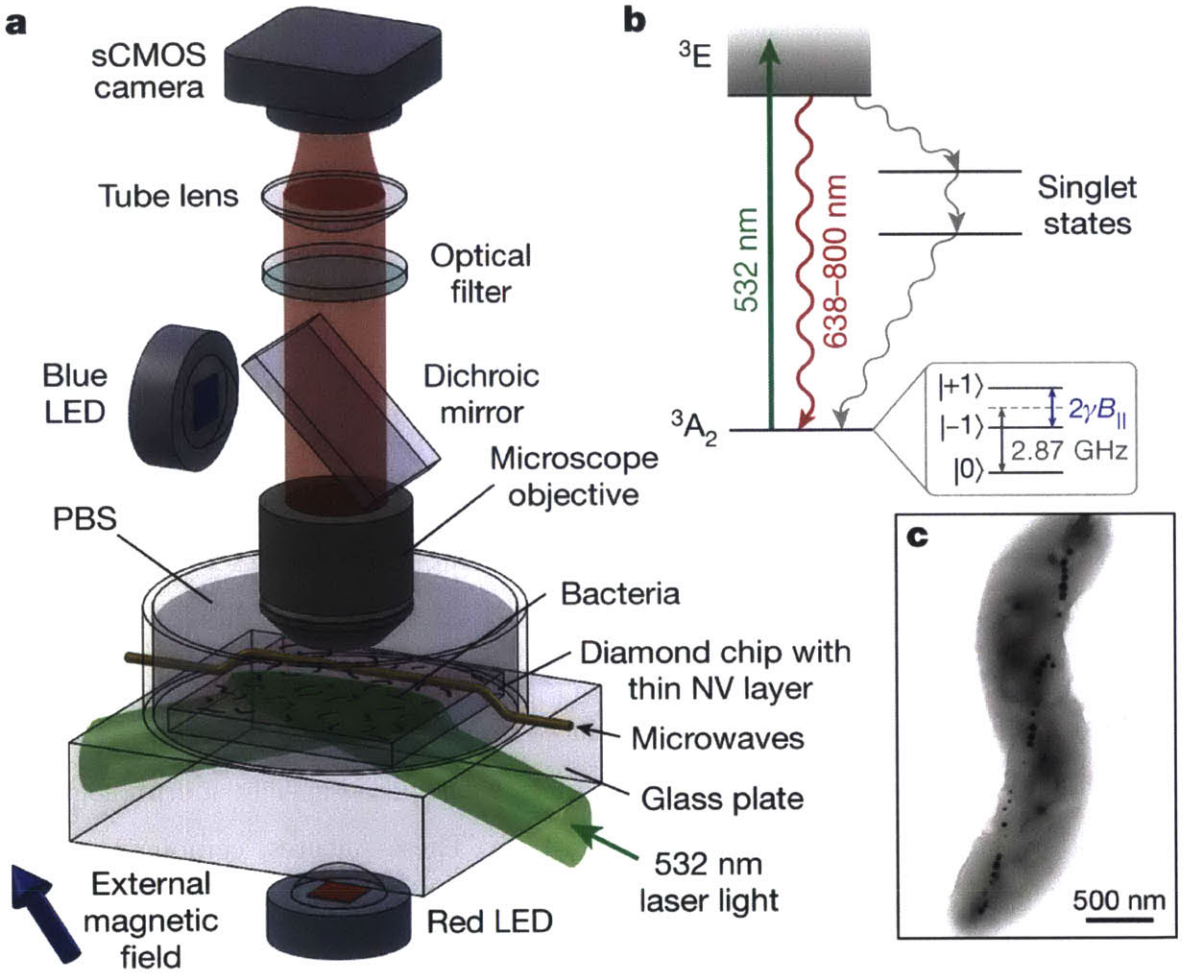

Figure 3-1: Wide-field magnetic imaging microscope. **a**, Custom-built wide-field fluorescence microscope used for combined optical and magnetic imaging. Live magnetotactic bacteria (MTB) are placed in phosphate-buffered saline (PBS) on the surface of a diamond chip implanted with nitrogen-vacancy (NV) centers. Vector magnetic field images are derived from optically detected magnetic resonance (ODMR) [19, 168, 242] interrogation of NV centers excited by a totally-internally-reflected 532 nm laser beam, and spatially correlated with bright field optical images. See text for details. LED, light-emitting diode. **b**, Energy-level diagram of the NV center; see Section 3.7 for details. **c**, Typical transmission electron microscope (TEM) image of an *M. magneticum* AMB-1 bacterium. Magnetite nanoparticles appear as spots of high electron density.

3.2 Wide-Field Magnetic Microscope

We acquired correlated magnetic field and optical images of populations of MTB using the NV-diamond wide-field imager depicted schematically in Fig. 3-1a [205]. The system was operated in two distinct configurations, one optimized for rapid magnetic imaging of living cells in a liquid medium, and the other for high-precision measurements of stable magnetic field patterns produced by dry bacteria on the diamond surface. In both cases, magnetic imaging was carried out using a pure diamond chip doped with a 10-nm-deep surface layer of NV centers. NV electronic spin states were optically polarized and interrogated with green illumination (wavelength $\lambda = 532$ nm), coherently manipulated using resonant microwave fields, and detected via spin-state-dependent fluorescence in the red (Fig. 3-1b). NV electronic spin resonance frequencies are Zeeman-shifted in the presence of a local external magnetic field (such as from magnetic nanoparticles in an MTB), allowing NV-fluorescence-based magnetometry by optically detected magnetic resonance (ODMR) [19, 168, 242]. Four independent ODMR measurements enabled determination of all vector components of the magnetic field within each imaging pixel (see Section 3.7). For imaging of live samples, the green excitation beam was directed into the diamond chip at an angle greater than the critical angle for the diamond-water interface, resulting in total internal reflection of high-intensity green light within the diamond, while low-intensity red NV fluorescence passed freely to the objective and was imaged onto the sCMOS (scientific complementary metal-oxide semiconductor) camera (Fig. 3-1a). Cells at the diamond surface were thereby decoupled from high optical intensity, allowing NV magnetic imaging times up to several minutes while maintaining cellular viability. For magnetic imaging of dry bacteria, the green excitation beam could be configured in the same manner as for live/wet samples, or be allowed to pass directly through the sample, normal to the diamond surface, with comparable optical and magnetic

imaging results.

3.3 Wide-Field Magnetic Imaging of Magnetotactic Bacteria

We obtained optical images of the magnetic field distributions produced by multiple cells on the diamond surface across a wide field of view (100 μm $\times$ 30 μm) and with high spatial resolution ($\sim$ 400 nm) using a sCMOS camera (Fig. 3-2). We concurrently acquired bright-field optical images using red (λ = 660 nm) LED illumination to enable correlation of cell positions and morphology with the observed magnetic field patterns. Immediately following magnetic imaging, the MTB were stained and imaged in fluorescence under blue (λ = 470 nm) LED excitation to perform a bacterial viability assay (see Section 3.7), using a conservative viability threshold that excluded non-viable bacteria with 99% certainty (see Appendix B.1). Under appropriate imaging conditions, the magnetic field patterns produced by the MTB could be measured within 4 min with minimal cellular radiation exposure, such that a significant fraction of the MTB remained alive after magnetic and bright-field imaging. For example, $\sim$ 44% of the MTB in the field of view shown in Fig. 3-2a, b were found to be viable after magnetic and bright-field imaging, compared to 54 % viability for cells directly from culture. Many of these living MTB produced magnetic field signals with large signal-to-noise ratios ($\sim$ 10). For high-precision characterization of the bacterial magnetic fields and comparison to electron microscope images, we also carried out a series of measurements using dried MTB samples on the diamond surface, imaged using a high-numerical-aperture (high-NA) air objective (Fig. 3-2c, d). Relaxing the requirement of maintaining cellular viability allowed for longer magnetic image averaging times, with concomitant reduction in photon shot-noise. Also, elimination of

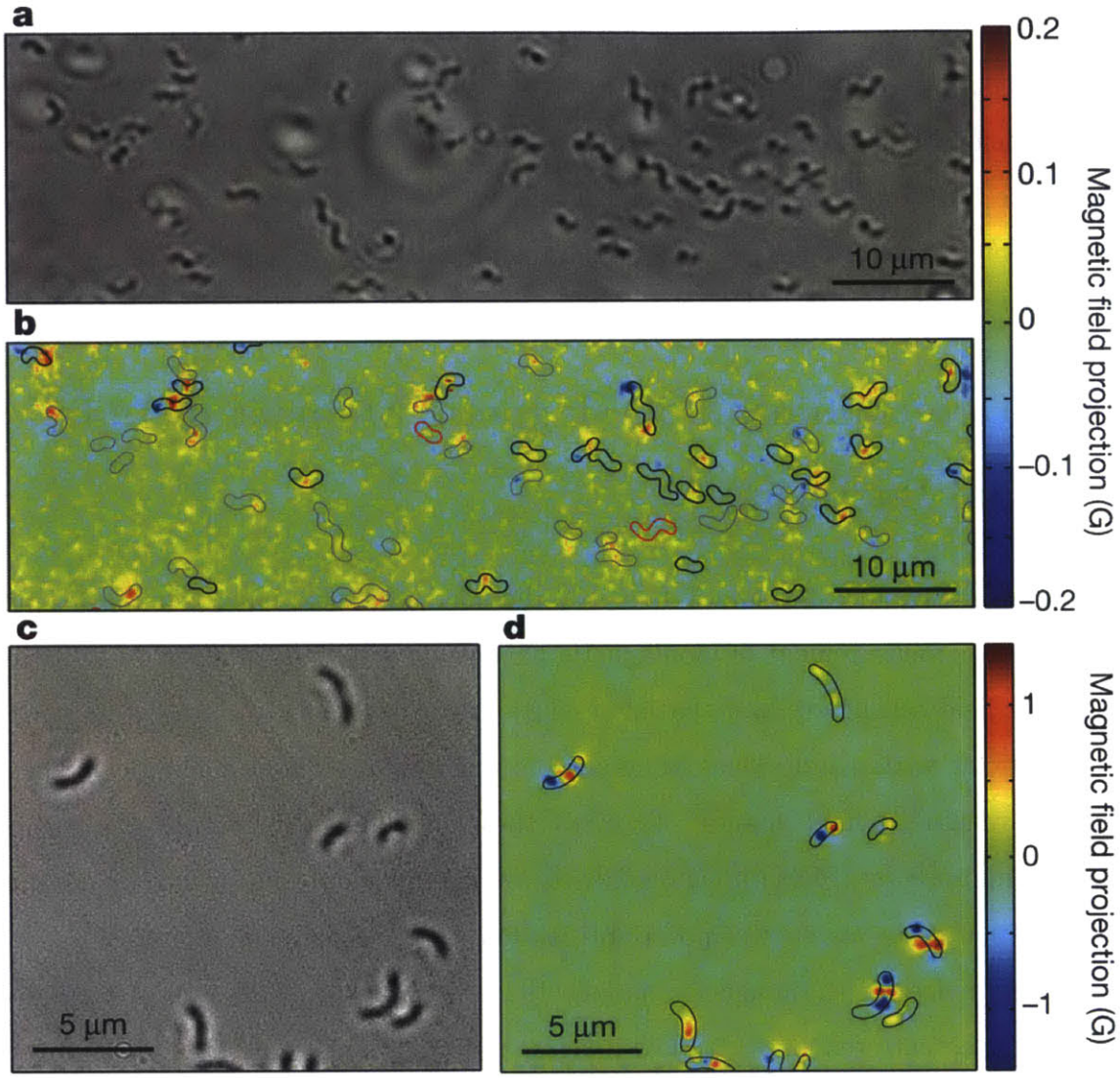

Figure 3-2: Wide-field optical and magnetic images of magnetotactic bacteria. **a**, Bright-field optical image of MTB adhered to the diamond surface while immersed in PBS. **b**, Image of magnetic field projection along the [111] crystallographic axis in the diamond for the same region as **a**, determined from NV ODMR. Superimposed outlines indicate MTB locations determined from **a**. Outline colors indicate results of the live-dead assay performed after measuring the magnetic field (black for living, red for dead, and grey for indeterminate). **c**, Bright-field image of dried MTB on the diamond chip. **d**, Image of magnetic field projection along [111] for the same region, with outlines indicating MTB locations determined from **c**.

both the poly-L-lysine adhesion layer (see Section 3.7) and residual cellular Brownian motion in liquid brought the cells closer to the diamond substrate and improved their spatial stability, resulting in higher time-averaged magnetic fields at the layer of NV centers near the diamond surface. We thus expect that the dried cell technique may be the preferred approach for biological applications that do not require sustained imaging of magnetic fields produced by developing cells.

3.4 Determination of Magnetic Moment of Individual Bacteria

As shown in Figs 3-2, 3-3, and 3-4 the NV-diamond wide-field imager enables rapid, simultaneous measurement of biomagnetic particle distributions in many MTB, with magnetic field sensitivity and spatial resolution sufficient both to localize magnetic nanoparticles within individual MTB and to quantify the MTB magnetic moment from the magnetic field images. To verify these capabilities, we recorded scanning electron microscope (SEM) images of dried MTB in place on the surface of the diamond chip after the magnetic and bright-field imaging had been completed. Positions and relative sizes of the magnetic nanoparticles within each MTB were determined from the backscattered electron SEM images, and used to calculate the expected vector magnetic field pattern from the MTB (up to a normalization constant equivalent to the total magnetic moment of the particles - see Section 3.7). The magnetic field patterns that we calculated (from SEM data) and measured (with the NV-diamond imager) were in excellent agreement (Fig. 3-3a-h), across a wide variety of magnetic nanoparticle distributions within the MTB (Fig. 3-4). We also determined the total magnetic moment of each MTB (for example, $(1.2 \pm 0.1) \times 10^{-16}$ A m^2 for the MTB in Fig. 3-3a-h) by numerically fitting the modelled field distribution to the measured

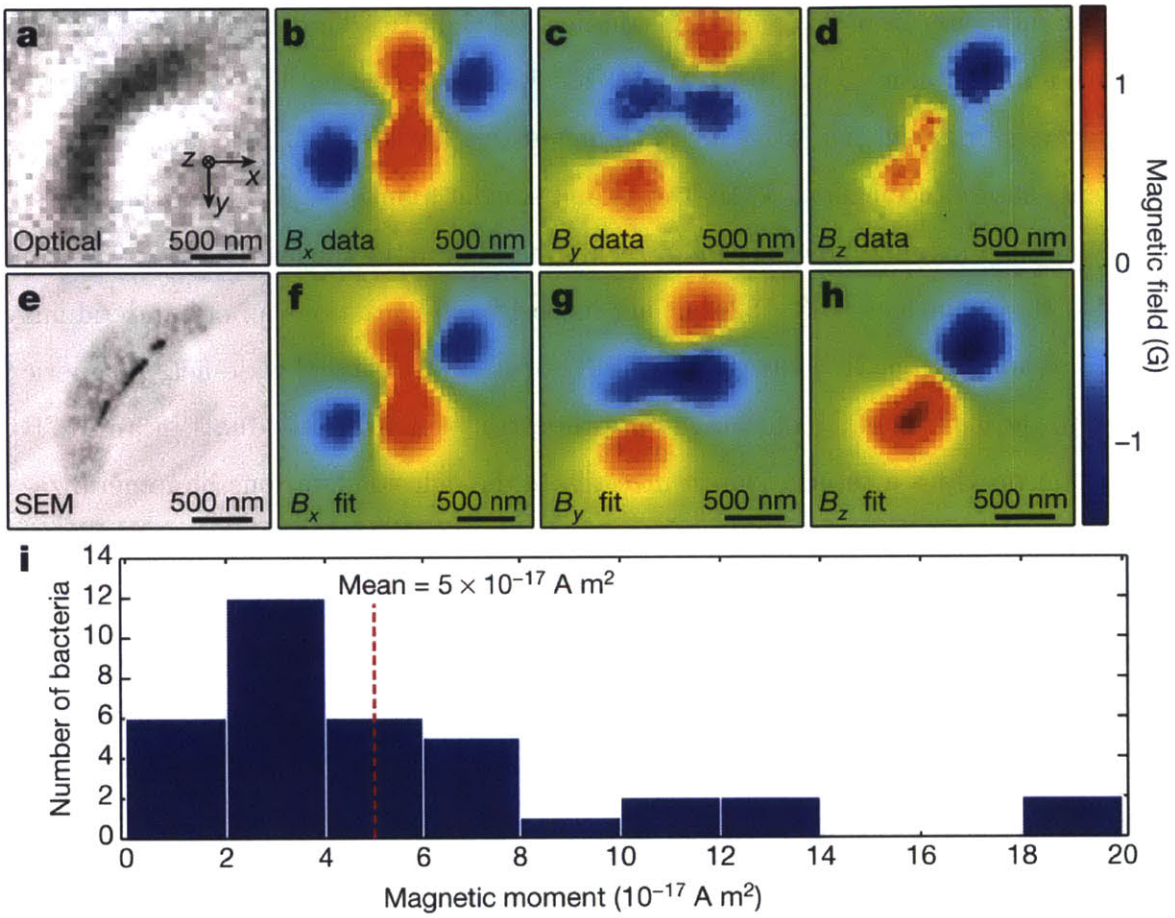

Figure 3-3: Determining magnetic moments of individual bacteria from measured magnetic field distributions. **a**, Bright-field image of an MTB. **b-d**, Measured magnetic field projections along the x axis (B_x; **b**), y axis (B_y; **c**) and z axis (B_z; **d**) within the same field-of-view. **e**, Scanning electron microscope (SEM) image of the same bacterium. **f-h**, Simulated magnetic field projections along the x axis (**f**), y axis (**g**) and z axis (**h**), assuming that magnetic nanoparticle locations match those extracted from **e**. The total magnetic moment was determined from the best fit of the calculated field distribution to the measurement (see Section 3.7 for details). **i**, Magnetic moments of 36 randomly-sampled MTB, as determined from optical magnetic field images and modelled field distributions.

distribution, leaving the standoff distance and magnetic moment as free parameters. From such optical magnetic field measurements, we determined the distribution of magnetic moments from 36 randomly-sampled MTB on the diamond surface (Fig. 3-3i), with a mean value (0.5×10^{-16} A m^2) that was consistent with previous estimates of the average moment per MTB for *M. magneticum* AMB-1 [143], although our measurements showed that most AMB-1 cells had smaller moments. Note that most previously applied magnetic measurement techniques determine the average properties of large MTB populations [143, 182] but are insensitive to variations among individuals within the population. In contrast, the ability of the NV-diamond wide-field magnetic imager to measure rapidly the magnetic properties of many individuals in an MTB population provides a robust tool to investigate the defects of various biomineralization mutants, making it possible to distinguish between defects that equally affect all cells in a population versus those that disproportionately disrupt magnetosome formation in a subset of cells. The *M. magneticum* AMB-1 bacteria studied here provided high signal-to-noise ratio magnetic imaging data, even though the typical magnetic moments of these bacteria are an order of magnitude smaller than many commonly studied MTB strains [209, 75]. This suggests that NV magnetic imaging will be applicable to a broad variety of MTB.

3.5 Localization of Magnetic Nanoparticle Chains

Furthermore, we were able to determine the positions of magnetic nanoparticle chains in individual MTB from the magnetic field distributions measured with the NV-diamond imager, even without the use of correlated SEM data, by noting that the magnetic nanoparticle chain endpoints occurred at locations of maximum field divergence (yellow bars in Fig. 3-4). Distinct groups of magnetic nanoparticles could be resolved if their separation was more than the 400 nm diffraction-limited resolution of

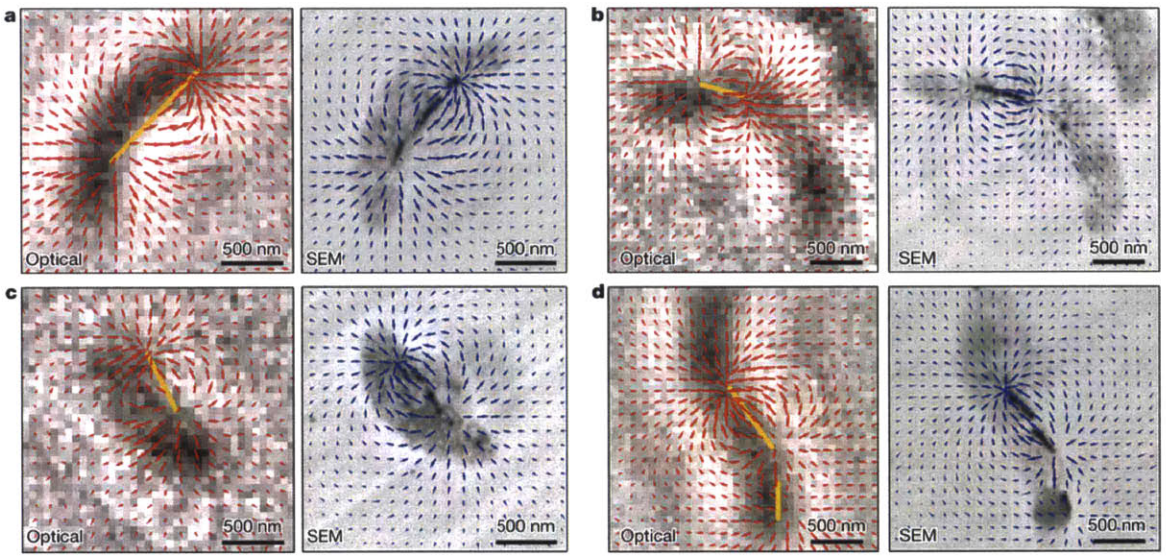

Figure 3-4: Localization of magnetic nanoparticle chains using magnetic field measurements. **a**, Vector plots of the measured (red arrows, left panel) and simulated (blue arrows, right panel) magnetic field projections in the $x - y$ plane, for the same MTB as in Fig. 3-3a-h, superimposed on the optical and backscattered electron images, respectively. The estimated location of the magnetic nanoparticle chain inside the MTB (yellow bar, left panel), as determined from the divergence of the measured magnetic field, coincides well with the magnetic nanoparticle positions found by SEM. **b-d**, The same information as presented in a, but for three different MTB. In **d**, two distinct magnetic nanoparticle chains are identified (yellow bars, left panel).

our optical magnetometry measurements (for example, Fig. 3-4d), and endpoints of single, well-isolated magnetic nanoparticle chains could be localized to within < 100 nm (for example, Fig. 3-4b). Using the chain positions and a simplified model for the magnetic nanoparticle field-source distribution, we estimated the total magnetic moments of individual MTB from the magnetic field data alone (without correlated SEM measurements). The magnetic moments determined using this analysis procedure (for example, 0.9×10^{-16} A m^2 for the MTB in Figs 3-3a-h and 3-4a, using the estimated chain position in Fig. 3-4a) agreed well with the values derived using the more detailed SEM-based models when the magnetic nanoparticles were arranged in long chains.

3.6 Discussions

The NV-diamond wide-field imager provides powerful new capabilities that could shed light on unanswered questions regarding the development of MTB magnetic properties [81, 113]. Some existing methods can probe the internal magnetic structure of a single MTB [75, 147], or measure the magnetic field [210] or field gradient [209] near a single MTB, but only NV magnetic imaging provides direct magnetic field measurements with sub-cellular resolution under ambient environmental conditions – opening the way to real-time imaging of magnetic nanoparticle formation and chain dynamics in single living MTB. Real-time magnetic measurements will enable observation of the transition of magnetic nanoparticles from superparamagnetic to permanent, single-magnetic-domain states as the nanoparticles grow [81]. The ability to locate chains of nanoparticles from the magnetic images will make it possible to measure the movement of magnetosome chains across the cell-division cycle of individual MTB.

The measurements presented here are also directly applicable to studying the formation of magnetic nanoparticles in other organisms [208]. Such formation is of

interest for MRI contrast enhancement [284], and has been linked with neurodegenerative disorders [66]; it has also been proposed as a mechanism for magnetic navigation in higher organisms [77, 181, 208]. In particular, there is great current interest in identifying potential vertebrate magnetoreceptor cells [77], which are believed to have a magnetic moment that is comparable to or larger than found in MTB, suggesting that high-throughput NV-diamond magnetic imaging could be a valuable tool for localizing magnetic cells in a broad range of tissue samples. More generally, with further improvements in detector sensitivity and the use of spin-echo techniques for the detection of time-dependent fields [151, 176, 205], NV-diamond magnetic imaging could be applied to a variety of biologically interesting systems, including firing patterns in neuronal cultures [109, 205], detection of free radicals generated by signalling or immune responses, and the localization of molecules tagged with specific spin labels.

3.7 Methods

3.7.1 Diamond samples

Magnetic field sensing was carried out using high-purity, single-crystal diamond chips. For imaging wet bacterial samples, we used an electronic-grade diamond (3 mm $\times$ 3 mm $\times$ 0.5 mm) grown using chemical vapor deposition (CVD) by Element Six Ltd. The diamond was implanted with $^{15}N^{+}$ ions at 14 keV energy and annealed at 1,200 ^{o}C to produce a 10-nm-thick layer of NV centers 20 nm beneath the surface of the diamond (as estimated using Stopping and Range of Ions in Matter (SRIM) software). The estimated NV surface density within the layer was 3×10^{11} NV per cm^2. For imaging dry bacterial samples, we used a high-purity, single-crystal diamond chip (1.5 mm $\times$ 1.5 mm $\times$ 0.3 mm) manufactured by Sumitomo Electric Industries using the high-pressure, high-temperature (HPHT) method. This diamond was implanted with

$^{15}N_2^+$ ions with 15 keV energy and then annealed at 800 °C to produce a 10-nm-thick layer of NV centers 10 nm beneath the surface of the diamond (as estimated using SRIM), with an estimated surface density of 1×10^{12} NV per cm^2.

3.7.2 Wide-field magnetic imaging microscope

NV centers were optically excited with a 532 nm laser (Changchun New Industries) switched on and off by an acousto-optic modulator (Isomet, M1133-aQ80L-1.5). A small fraction of the laser light was split off and directed onto a photodiode (Thorlabs), and the resulting signal was sent to a servo-lock system (New Focus) to amplitude-stabilize the excitation beam using the same acousto-optic modulator. For imaging of bacterial samples in liquid, laser light was coupled into the diamond from below through a polished glass cube (constructed from two right-angle prisms, Thorlabs), to which the diamond was affixed by optical adhesive (Norland). The peak intensity of the totally-internally-reflected laser light at the interior surface of the diamond was measured in this case to be ~ 1 kW cm^{-2}. We also note that for our angle of incidence at the diamond-water interface, $\theta_{dw} \approx 39°$, the calculated attenuation length for the evanescent wave intensity is $d_{dw} = 58$ nm. For imaging of dry samples, laser light could be configured in the same manner as for live/wet samples, or directed onto the bacteria from below, normal to the diamond surface. Dry sample data presented here were acquired using the latter method.

A 660-nm-wavelength LED (Thorlabs) was used to back-illuminate the sample for bright-field images. Excitation of fluorescence dyes used in the bacterial viability assays (see below) was carried out with a 470-nm LED (Thorlabs), directed onto the sample through the microscope objective. Optical fluorescence or transmitted red LED light was collected by the objective (Olympus, UIS2 LumFLN 60xW /1.1 NA for wet samples; Olympus, MPlan FLN 100x/0.90 NA for dry samples), passed

through a dichroic mirror (Thorlabs for wet samples; Semrock for dry samples) and an optical filter (Semrock for NV fluorescence and transmitted red light; emission filters as described below for fluorescence from bacterial viability assay dyes), and imaged onto a digital camera (Andor for wet samples; Starlight Xpress for dry samples). The output of a microwave synthesizer (SRS) was controlled by a switch (Mini-Circuits), then amplified (Mini-Circuits) and applied to the diamond with a wire. A permanent magnet was used to apply a uniform external magnetic field.

3.7.3 ODMR measurements

M. magneticum AMB-1 cells were grown statically in 1.5-ml microcentrifuge tubes filled with 1.5 ml of growth medium (described in ref.[139], but with 0.1 g l^{-1} of sodium thiosulphate). For measurements of wet samples, the diamond surface was prepared by placing a drop ($\sim$ 5 μL) of 0.01 % poly-L-lysine solution (Sigma molecular mass 70-150 kDa) on its surface, which was then allowed to dry. The bath around the diamond (contained in a chamber consisting of a cut microcentrifuge tube glued to the glass mounting surface, volume $\sim$ 200 μL) was filled with 50 μL of bacterial solution, and topped up with PBS. For dry measurements, a drop of bacterial solution was placed directly on the diamond above the NV layer, allowed to dry, rinsed with deionized water, and dried a second time. The sample was then placed in the imager with the active diamond surface facing the objective. A uniform 37 G external magnetic field was applied along a single NV axis to distinguish it from the other three NV axes. This magnetic field strength was an order of magnitude less than the coercive field typically required to flip the magnetic orientation of MTB [75, 209], and we found that the magnetization of the MTB described here remained fixed as the external field was varied.

ODMR [19, 168, 242] spectra were measured by imaging NV fluorescence from

the whole field-of-view at different microwave frequency values. The typical total fluorescence collection time was 4 min for both wet and dry bacterial samples. For each pixel, Lorentzian fits were applied to the ODMR spectra and the magnetic field shifts along the NV axis were extracted. This procedure was repeated with the external field applied along each of the four NV axes, which in turn allowed the vector magnetic field in the NV layer to be determined for all three Cartesian directions across the field-of-view. For magnetic fields B_1 to B_4, corresponding to measurements along axes 1 to 4, respectively, the fields in the Cartesian coordinates were calculated from

$$B_x = \frac{\sqrt{3}}{2\sqrt{2}}(B_2 - B_4) \tag{3.1a}$$

$$B_y = \frac{\sqrt{3}}{2\sqrt{2}}(B_1 - B_3) \tag{3.1b}$$

$$B_z = \frac{\sqrt{3}}{4}(-B_1 - B_2 - B_3 - B_4) \tag{3.1c}$$

3.7.4 Bacterial viability assay

Immediately after magnetic field imaging of wet samples, the viability of the bacteria was determined in place on the diamond surface using a standard fluorescence-based live-dead assay (Molecular Probes, BacLight kit). A mixture of the fluorescent nucleic acid stains SYTO 9 (final concentration 5 μM) and propidium iodide (final concentration 30 μM) was added to the bath, and bright-field images were immediately collected to verify that the positions of the bacteria on the diamond surface were not perturbed. The sample was then incubated in the dark for 15 min, and fluorescence images were collected by exciting with a LED at 470 nm (Thorlabs). Green SYTO-9 fluorescence and red propidium iodide fluorescence were collected successively using appropriate emission filters (Thorlabs for green; Chroma for red). Custom software was used

to co-register the resulting fluorescence images and perform rolling-ball background subtraction, and a peak-finding algorithm was applied to determine the positions of the bacteria. The ratio of red to green fluorescence intensity, integrated over each cell, was calculated and compared to a live/dead calibration performed previously under the same conditions (see Section B.1 for details). MTB with a fluorescence ratio less than 0.5 were taken to be alive, while those with a fluorescence ratio greater than 1.0 were assigned as dead. Bacteria with intermediate fluorescence ratios between 0.5 and 1.0 could not be assigned to either category with high certainty based on assay calibration measurements, and were therefore labelled as indeterminate in experimental data.

Before collecting the data displayed in Fig. 3-2, we carried out a series of preliminary live-dead assays, including the calibrations described in Appendix B.1. These assays revealed that, even after a full hour of exposure to $f \approx 2.88$ GHz microwave fields at the intensities used in our ODMR measurements, the fraction of bacteria remaining alive was essentially the same as that in unperturbed samples immediately after they were taken from culture. This suggests that any bacterial fatality during experiments was the result of residual evanescent coupling of laser light through the diamond surface. These observations were consistent with direct measurements of the bath temperature when microwave power was applied, which showed only a modest increase of 1-2 °C above room temperature.

3.7.5 Electron microscopy

After magnetic field measurements were completed on dried samples, imaging was performed with a field emission SEM (Zeiss Sigma). The diamond substrate and intact bacteria were carbon-coated in a thermal evaporator (Edwards Auto 306) and mounted on silicon wafers using copper tape. The bacteria were imaged without dehy-

dration or fixation. Images of magnetic nanoparticles were obtained using backscatter mode, at x30,000 magnification and with an accelerating voltage of 8 kV. The TEM image in Fig. 3-1c was recorded using the procedure outlined in ref. [183].

3.7.6 Fitting the magnetic field of an MTB

Magnetic field patterns of the bacteria were fitted with a constrained model using SEM measurements of the relative sizes and positions of the magnetic nanoparticles, with standoff distance from the diamond and magnetic moment scaling factors left as free parameters. First, a peak-finding algorithm was applied to locate magnetic nanoparticles in the image. Magnetic nanoparticle chains were determined by assigning two adjacent magnetic nanoparticles to the same chain if their separation was less than 120 nm. For each chain, the orientation of the magnetic moment in the plane of the diamond surface was determined using a linear fit to the magnetic nanoparticle positions. Gaussian curves were fitted to the SEM images of each magnetic nanoparticle along the direction perpendicular to the axis of the chain, and the fit amplitudes were used to assign relative magnetic moment densities along the chain. Each magnetic nanoparticle in a chain was assumed to act as a point dipole with the same magnetic moment direction as its chain. (This approximation was motivated by the observation of highly aligned magnetic nanoparticle dipoles in previous work (see, for example, refs [75, 147]). In some cases, individual magnetic nanoparticle were further than 120 nm from any chains; their dipole moment was estimated to be in the same direction as that of the nearest chain.

Next, a nonlinear fit routine using the Levenberg-Marquardt algorithm was performed to match simulated magnetic field images with those measured. The simulation first calculated the three components of the magnetic field on the diamond surface using the positions, directions and relative magnetic strengths of each mag-

netic nanoparticle. The ODMR signal for all NV axes was then calculated for each pixel, and these signals were convolved with a point-spread function (full-width at half-maximum of 400 nm) to create simulated ODMR fluorescence data. As in the case of the measured data, images of B_x, B_y and B_z were reconstructed on a pixel-by-pixel basis from the frequency shifts for the four NV axes extracted from Lorentzian fits. The algorithm was run independently to minimize x and y position offsets of the SEM images as well as the standoff distance from the diamond surface. Generally, Bx images were used for the fitting. Finally, the overall magnetic moment was calculated on a pixel-by-pixel basis for the best-fit geometry, and the optimal value was determined by least-squares fitting to the measured data. The best-fit magnetic moment did not depend strongly on the value of the best-fit standoff distance for typical distances of 100-200 nm, owing to convolution of the NV fluorescence signal with the $\sim$ 400-nm point spread function of the optical microscope. We note that this method cannot recover exact dipole orientations, particularly for isolated magnetic nanoparticles. Nevertheless, the overall magnetic moment is dominated by contributions from long chains, whose field patterns are well-described by this method.

3.7.7 Estimating magnetic properties directly from ODMR

In cases where magnetic nanoparticles were organized into ordered chains that were well-approximated by finite solenoids, the chain positions and magnetic moments could be determined even without comparison to SEM data. Chain locations and orientations were estimated from the measured magnetic field divergence in the diamond plane ($\partial B_x/\partial x + \partial B_y/\partial y$) by assigning chain endpoints to the local maxima and minima of the divergence. (The maximum precision of this estimate is given approximately by the diffraction-limited resolution of the ODMR measurement divided by the signal-to-noise ratio of the calculated magnetic field divergence, which

is approximately 40 nm.) The chain was then approximated as a continuous line of magnetic dipoles, which can be shown to have the same field as a magnetic source and sink separated by the chain length (that is, a narrow finite solenoid). This provided a simple way to calculate B_z just below the chain. The magnetic moment could then be determined directly by spatially integrating the absolute value of B_z across the diamond surface. This integrated value is independent of standoff distance when the chain length is much larger than the standoff distance and the diameter of the field-of-view is much larger than the chain length. Moreover, it is independent of the point-spread function of the microscope objective.

Chapter 4

Fourier Magnetic Imaging

Optically detected magnetic resonance using nitrogen-vacancy (NV) color centers in diamond is a leading modality for nanoscale magnetic field imaging [19, 176, 249], as it provides single electron spin sensitivity [100], three-dimensional resolution better than 1 nm [102] and applicability to a wide range of physical [90, 165, 169, 223, 239, 244, 245] and biological [150, 215] samples under ambient conditions. To date, however, NV-diamond magnetic imaging has been performed using 'real-space' techniques, which are either limited by optical diffraction to $\sim$ 250 nm resolution [205] or require slow, point-by-point scanning for nanoscale resolution, for example, using an atomic force microscope [168], magnetic tip [102], or super-resolution optical imaging [174, 272]. In this chapter, we introduce an alternative technique of Fourier magnetic imaging using NV-diamond. In analogy with conventional magnetic resonance imaging (MRI), we employ pulsed magnetic field gradients to phase-encode spatial information on NV electronic spins in wavenumber or 'k-space' [236] followed by a fast Fourier transform to yield real-space images with nanoscale resolution, wide field of view and compressed sensing speed-up.

4.1 Introduction

The key advantages of NV-diamond Fourier magnetic imaging, relative to real-space imaging, are (1) spatially multiplexed detection [79, 190], which enhances the signal-to-noise ratio (SNR) for typical NV center densities, (2) a high data acquisition rate that can be further boosted with compressed sensing [44, 166], and (3) simultaneous acquisition of signal from all NV centers in the field of view (FOV), which allows temporally correlated dynamics to be probed and provides isolation from system drift. Importantly, our technique achieves Fourier magnetic imaging via phase-encoding of the detector (the NV spins in diamond), which is more widely applicable to the diversity of nanoscale magnetic phenomena in condensed matter systems than existing Fourier magnetic imaging techniques, which perform phase-encoding on spins in the sample, for example, protons in organic solids [190]. As described in the following, we demonstrate one-dimensional imaging of individual NV centers with < 5 nm resolution, two-dimensional imaging of multiple NV centers with ~ 30 nm resolution, and two-dimensional imaging of nanoscale magnetic field patterns with a magnetic gradient sensitivity of ~ 14 nT nm^{-1} Hz$^{-1/2}$ and spatial dynamic range (FOV/resolution) of ~ 500. We also show that compressed sensing can accelerate the image acquisition time by an order of magnitude.

4.2 Phase Encoding Gradient

4.2.1 Fourier magnetic microscope

Schematic views of the Fourier magnetic microscope are presented in Fig. 4-1a,b. The diamond sample has a thin layer of NV centers at the surface, created by ion implantation (see Section 4.7.1). NV electronic spin states (Fig. 4-1c) are optically polarized with green illumination, coherently manipulated using resonant microwave

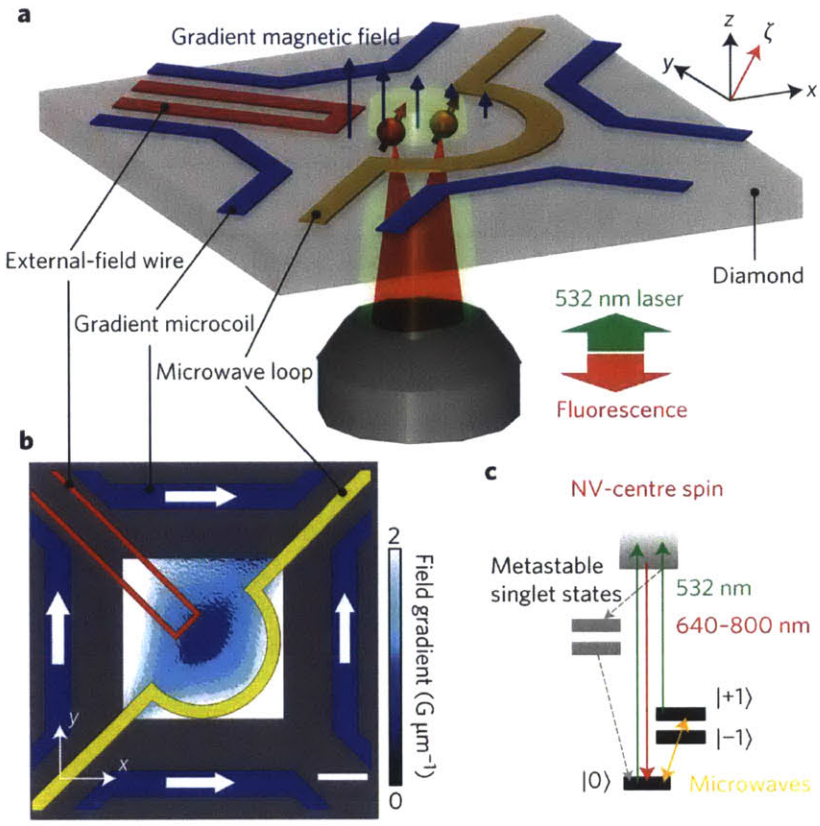

Figure 4-1: Fourier magnetic microscope. **a**, Schematic of the Fourier magnetic imaging microscope. NV-center magnetic sensors are located near the surface of a diamond chip (for example, as represented by spheres with arrows). NV spin states are initialized and read out with a green (532 nm) laser and coherently manipulated with resonant pulses using a microwave loop. Controlled magnetic field gradients for NV spin phase encoding are generated by sending currents through pairs of gold wires (gradient microcoils) separated by 100 μm and connected in an anti-Helmholtz configuration. An external-field wire is used to create a non-uniform d.c. or a.c. magnetic field for demonstrations of nanoscale Fourier magnetic imaging. The NV quantization axis, represented by ζ, is offset from the surface normal (z-axis) of the [100]-cut diamond sample and aligned with a static, uniform magnetic field of ~ 30 G created by a permanent magnet (not shown). **b**, Top-view schematic of the Fourier magnetic imaging microscope, as well as a simulation (using COMSOL Multiphysics) of the magnetic field gradient $\sqrt{(dB_\zeta/dx)^2 + (dB_\zeta/dy)^2}$ when a current of 1 A is sent through both microcoil pairs, with current directions indicated by white arrows. Scale bar, 20 μm. **c**, Energy-level diagram of the NV center (see Section 2.3 for details).

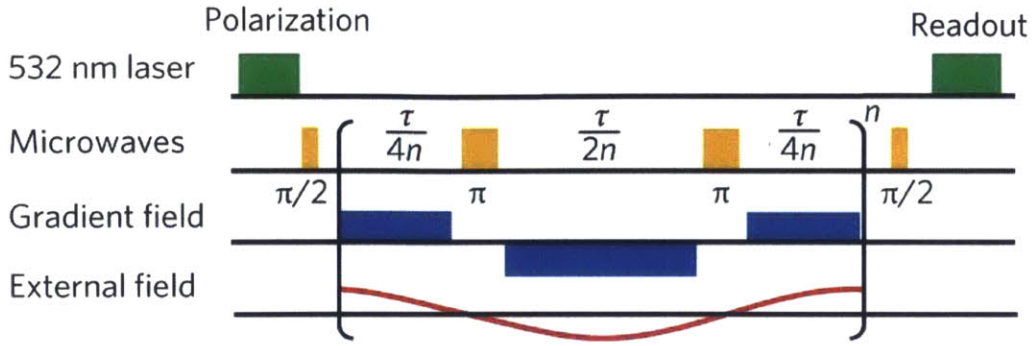

Figure 4-2: Fourier magnetic imaging experimental sequence. Spins are polarized into the $|0\rangle$ state with a green laser pulse. A microwave pulse sequence with $2n$ π pulses dynamically decouples NV centers from magnetic field noise from the environment. A pulsed magnetic field gradient of alternating direction is applied during each precession interval. Spins at different locations accumulate phase at different rates. A final $\pi/2$ pulse projects the spins into the $|0\rangle \leftrightarrow |1\rangle$ manifold, and state populations are read out optically via spin-dependent fluorescence. An a.c. magnetic field B_{ext} produced by current in the external-field wire can be sensed using the procedure described in Section 4.4.

fields applied by a microwave loop, and detected via spin-state-dependent fluorescence measurements. Strong, uniform magnetic field gradients for NV spin phase-encoding are generated by currents sent though pairs of gold wires (gradient microcoils). As a demonstration, another current sent through an external-field wire produces a non-uniform magnetic field pattern that can be imaged with the NV sensors in the sample. Figure 4-1b shows a simulation of the gradient produced by a current of 1 A sent through the gradient microcoils. At the center of the microcoils, the gradient magnitude projected onto the NV quantization axis ζ is $|dB_\zeta/dx| = |dB_\zeta/dy| \approx 0.7$ G μm^{-1} and varies by < 1 % over a 15×15 μm^2 region.

4.2.2 Fourier magnetic imaging and sensing protocol

The Fourier magnetic imaging pulse sequence consists of a laser initialization pulse, microwave dynamical-decoupling pulses for spin-state manipulation [60, 203] and a laser readout pulse (Fig. 4-2). A pulsed gradient field (dB_ζ/dx and/or dB_ζ/dy) for NV spin phase-encoding is applied during the microwave sequence. The sign of the gradient is switched during alternate free precession intervals to enable a.c. magnetic field sensing. The NV spin at position $\boldsymbol{r}_0$ thus acquires a position-dependent phase

$$\phi = 2\pi \boldsymbol{k} \cdot \boldsymbol{r}_0, \tag{4.1}$$

where $\boldsymbol{k} = (2\pi)^{-1}\gamma\tau(dB_\zeta/dx, dB_\zeta/dy)$ defines the imaged point in the two-dimensional Fourier or k-space. Here, $\gamma/2\pi = 2.8$ MHz G^{-1} is the NV gyromagnetic ratio and τ is the total precession time. The optical NV signal for this k-space point is proportional to the cosine of the acquired phase ϕ:

$$s(\boldsymbol{k}) \sim \cos(2\pi \boldsymbol{k} \cdot \boldsymbol{r}_0). \tag{4.2}$$

By incrementally stepping through a range of amplitudes for the applied magnetic field gradient, while keeping τ fixed, the NV signal is measured as a function of $\boldsymbol{k}$ to produce a k-space image. The real-space image is then reconstructed by Fourier transformation of the k-space image; that is,

$$S(\boldsymbol{r}) = F[s(\boldsymbol{k})], \tag{4.3}$$

where abs$[S(\boldsymbol{r})]$ gives the positions of the NV centers. The pixel resolution of the real-space image is $(2k_{\max})^{-1}$, where $k_{\max} = (2\pi)^{-1}\gamma\tau(|dB_\zeta/dx|, |dB_\zeta/dy|)_{\max}$ is the maximum k value used in the measurement.

4.3 Nanoscale NV Localization

4.3.1 1D imaging

As a first demonstration of NV Fourier imaging, we acquired a one-dimensional image of a single NV center in a sample with low NV density (sample A, see Section 4.7.1) by varying only the dB_ζ/dx gradient strength and using a four-pulse Carr-Purcell-Meiboom-Gill (CPMG) decoupling sequence with $\tau = 104$ μs. The initialization and readout times were both 5 μs. The image was acquired for k values between 0 and 0.144 nm^{-1} in $N_{\text{pix}} = 2,400$ steps. The sequence was repeated 30,000 times and the total data acquisition time per k value was $T = 3.42$ s. We observed oscillations with a period of 0.0025 nm^{-1} in the k-space image (Fig. 4-3a). Upon Fourier transformation, the k-space image produced a real-space image with a single peak indicating the single NV location. The peak width and amplitude correspond to a real-space pixel resolution of 3.5(6) nm and SNR = 13 (Fig. 4-3b). Thus, the data acquisition time to reach SNR = 1 was $T_{\text{SNR}=1} = T/\text{SNR}^2 \approx 20$ ms. We observed no significant broadening of the real-space signal peak at this image resolution, indicating an insignificant effect from technical issues such as gradient current instability, thermal fluctuations, mechanical vibrations and laser instability.

4.3.2 2D imaging

We next demonstrated two-dimensional Fourier imaging of multiple NV centers using a sample with high NV density (sample B, see Section 4.7.1). To create a regular pattern of NV centers to be imaged for this and later demonstrations, we fabricated arrays of nanopillars (400 nm diameter, 100 nm height, 1 μm spacing) on the diamond surface. We chose the implant dosage and nanopillar size such that there were, on average, two NV centers of the same crystallographic orientation per nanopillar.

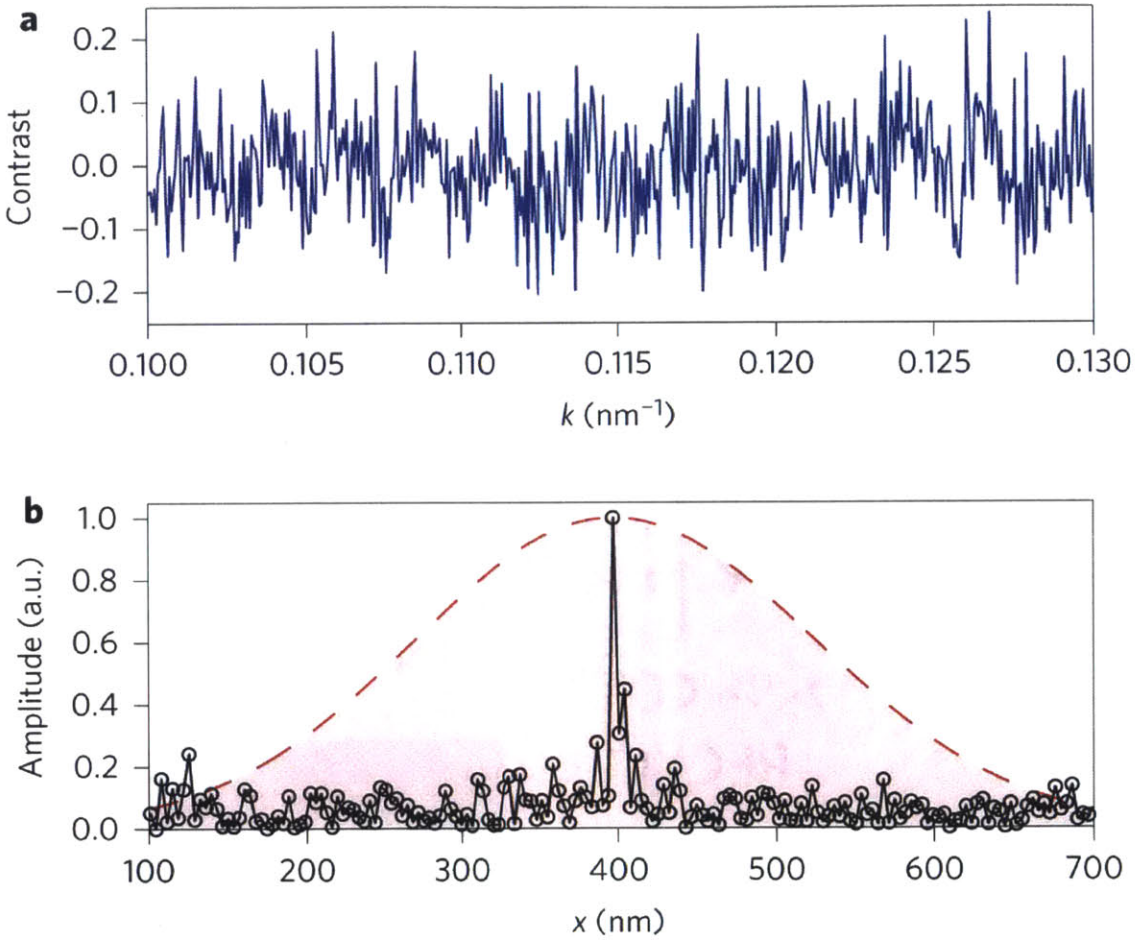

Figure 4-3: Fourier 1D imaging of NV centers with nanoscale resolution. **a**, One-dimensional k-space image of a single NV center in diamond (sample A) using a four-pulse CPMG sequence ($n = 2$). As the gradient strength dB_ζ/dx is incrementally stepped by varying the current through the microcoil, the NV fluorescence shows sinusoidal oscillations. Here, we show NV fluorescence normalized to a reference measurement of $|0\rangle$ state fluorescence and with a constant background level subtracted. **b**, One-dimensional real-space image data (black) obtained from the absolute value of the Fourier transform of the k-space data. For comparison, the diffraction-limited, real-space point spread function of the microscope is shown (pink shaded area, full-width at half-maximum of 300 nm).

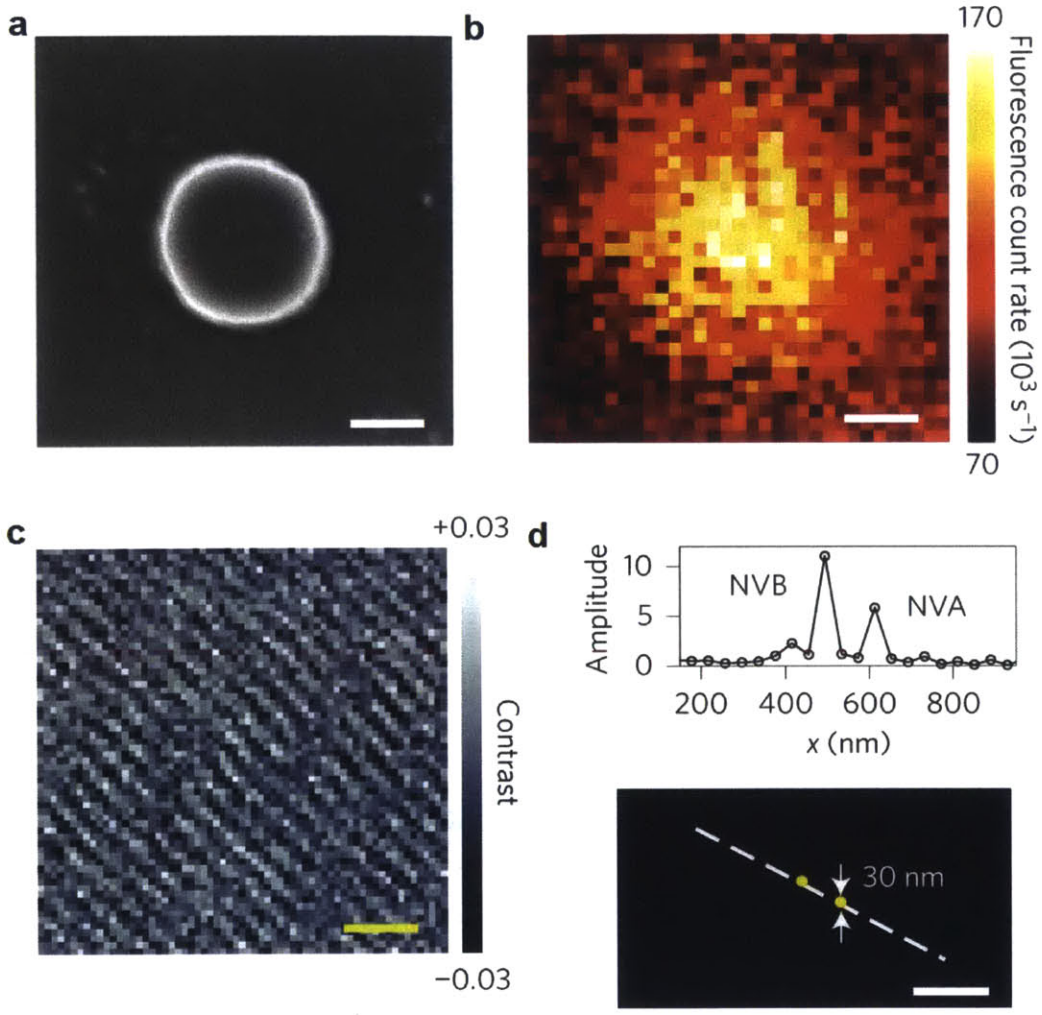

Figure 4-4: Fourier 2D imaging of NV centers with nanoscale resolution. **a**, Scanning electron micrograph of a 400-nm-diameter NV-containing diamond nanopillar fabricated on sample B. **b**, Scanning confocal fluorescence image of the same nanopillar (full-width at half-maxima of corresponding x and y profiles of $\sim$ 400 nm). **c**, Two-dimensional k-space image of two proximal NV centers inside this same nanopillar using a Hahn-echo sequence ($n = 1/2$). **d**, Bottom: Fourier-transformed, two-dimensional real-space image (absolute value) with a threshold set at 5σ above the noise level, where σ is the standard deviation of observed optical noise. Top: cross-section of the two peaks along the direction indicated by the white dashed line in the two-dimensional image. Two NV centers separated by 121(9) nm are clearly resolved. Scale bars: 200 nm (**a**,**b**,**d**) and 0.0066 nm^{-1} (**c**).

Scanning electron microscope and confocal microscope images of a typical nanopillar are shown in Fig. 4-4a and b, respectively. We used a spin-echo sequence and varied both the dB_ζ/dx and dB_ζ/dy gradient strengths to acquire a two-dimensional k-space image of the NV centers in this nanopillar (Fig. 4-4c). A Fourier transform of the k-space image, thresholded at 5σ above the noise level (see Appendix C.5), reveals two proximal NV centers separated by 121(9) nm with a pixel resolution of 30 nm (Fig. 4-4d). This resolution is consistent with the k-space spanned in Fig. 4-4c. For this two-dimensional Fourier image, the data acquisition time to reach SNR = 1 was $T_{\mathrm{SNR}=1} \approx 20$ ms.

4.4 Nanoscale AC Field Sensing

Once the locations of individual NV centers are determined precisely, they can be used as high-sensitivity probes of magnetic fields that vary on length scales smaller than the optical diffraction limit. To demonstrate such nanoscale Fourier magnetic imaging, we introduced a spatially inhomogeneous magnetic field over the FOV in the center of the gradient microcoils by sending an alternating electric current, phase-locked to the dynamical-decoupling microwave pulse sequence (Fig. 4-2), through the external-field wire shown in Fig. 4-1a,b. NV centers within this region were thus exposed to different a.c. magnetic field amplitudes depending on their locations relative to the external-field wire. For a fixed value of alternating current, the k-space signal for a given NV at location $\boldsymbol{r}_0$ acquires a phase offset $\theta = \gamma B_{\mathrm{ext}} \tau$, where B_{ext} is the a.c. magnetic field amplitude (projected along the NV axis) at the site of the NV: that is,

$$s(\boldsymbol{k}) \sim \cos\left(2\pi \boldsymbol{k} \cdot \boldsymbol{r}_0 + \theta\right). \tag{4.4}$$

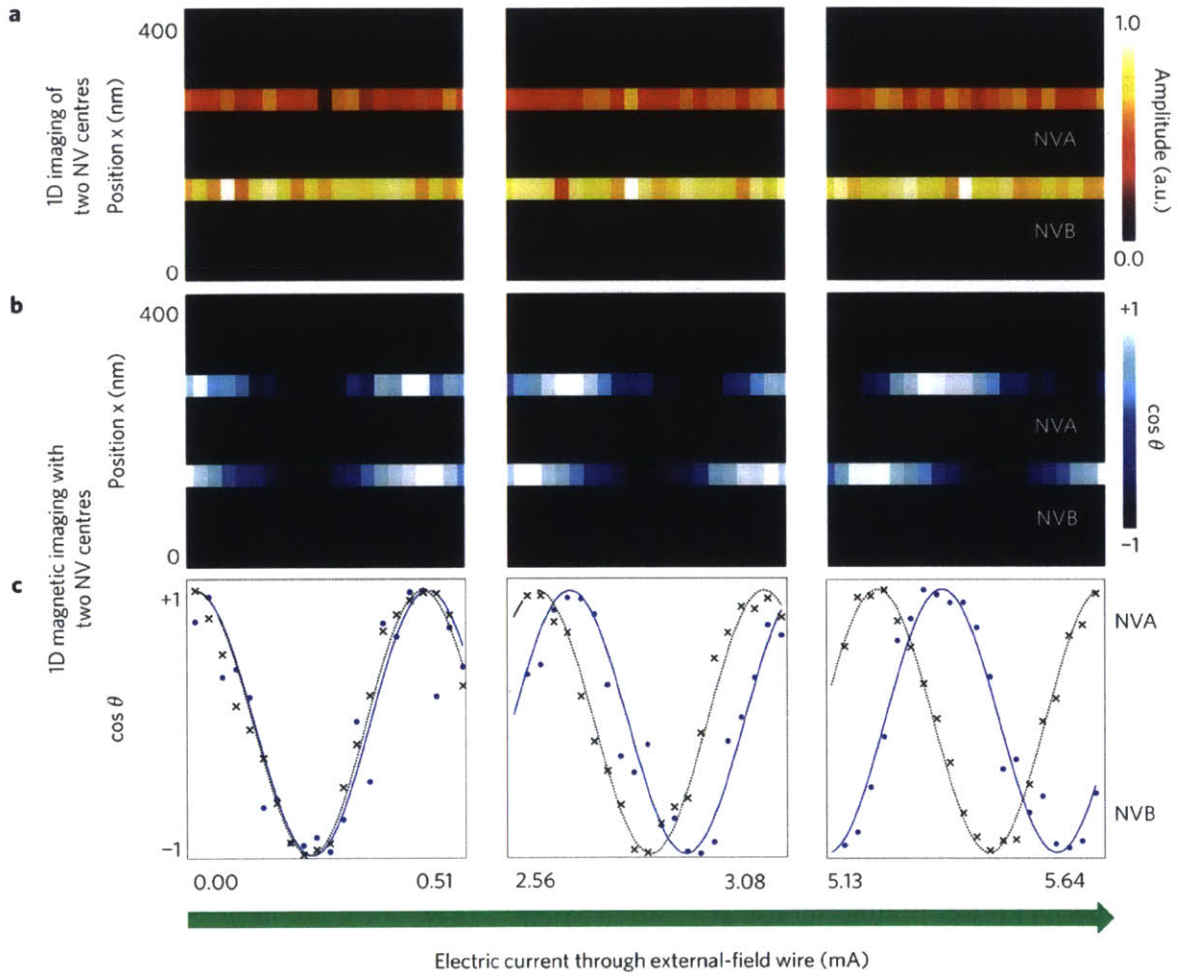

Figure 4-5: Fourier magnetic gradient sensing below the optical diffraction limit. (Continued on the following page.)

Figure 4-5: (Continued from the previous page.) One-dimensional k-space magnetic images for the two NV centers shown in Fig. 4-4d are acquired by incrementally stepping the dB_ζ/dx gradient strength for fixed values of a.c. current sent through the external-field wire. For each current value, the corresponding k-space image is Fourier-transformed and thresholded at 5σ to obtain a one-dimensional real-space image. **a**, Absolute value of the real-space image shows peaks corresponding to the two NV centers separated by 121(9) nm. The vertical axis is real-space position along the x direction and the horizontal axis corresponds to different ranges of a.c. currents at a frequency of 50 kHz, increasing from left to right: 0-0.51, 2.56-3.08 and 5.13-5.64 mA. **b**, Cosine of the argument of the real-space images of the two NV centers shown in a, for the same ranges of a.c. currents. **c**, Overlay of measured values for $\cos\theta$ (symbols) and corresponding fits (solids curves) as a function of a.c. current amplitude for the two NV centers, where $\theta = \gamma B_{\text{ext}}\tau$. The observed differential phase shift between the data for the two NV centers shows that these spatially separated NV centers measure a magnetic field difference ΔB_{ext} arising from a gradient in the external a.c. magnetic field magnitude B_{ext}.

As before, Fourier transforming the k-space image produces a real-space image with abs$[S(\boldsymbol{r})]$ showing a peak at $\boldsymbol{r} = \boldsymbol{r}_0$. Additionally, the argument arg$[S(\boldsymbol{r}_0)]$ yields the phase shift θ from which B_{ext} can be determined. Figure 4-5 shows how measured values for B_{ext} can be uniquely assigned to the two NV centers shown in Fig. 4-4d. For each value of applied alternating current we recorded a one-dimensional k-space image by incrementally varying the dB_ζ/dx gradient strength. Figure 4-5a shows the resulting values of abs$[S(x)]$ as a function of current through the external-field wire with a threshold set at 5σ. We consistently observe two distinct peaks (corresponding to the two NV locations) through the entire current range. The cosine of arg$[S(x_i)]$, where $x_{i=1,2}$ denotes the location of each peak, is shown in Fig. 4-5b,c. When the applied current is small (that is, weak B_{ext} gradient), the two NV centers are exposed to nearly the same value of B_{ext} and consequently there is little difference in the measured NV k-space phases (left panel of 4-5c). However, for a larger current of 5.13 mA (that is, stronger B_{ext} gradient, right panel of 4-5c), the measured NV k-space phase difference is $2\pi \times (2.6 \pm 0.4) \times 10^{-1}$ rad, which yields a magnetic field

difference of $\Delta B_{\text{ext}} = (6.5 \pm 1.1) \times 10^2$ nT between these two NV centers separated by 121(9) nm, equivalent to a magnetic gradient sensitivity of ~ 14 nT nm^{-1} Hz$^{-1/2}$ (Appendix C.7). The measured field and gradient values are consistent with those expected from simulations.

NV-diamond Fourier magnetic imaging can also be integrated with wide-field, real-space microscopy to realize a large spatial dynamic range: that is, magnetic imaging with both wide FOV and nanoscale resolution. As a demonstration of such hybrid real + k-space imaging, we scanned the Fourier magnetic microscope across a wide array of NV-containing nanopillars in sample B and performed both low-resolution real-space and high-resolution k-space NV imaging of magnetic field patterns produced by the external-field wire. Real-space image resolution is limited by optical diffraction, while nanometer-scale information is obtained via Fourier magnetic imaging. For example, we sent an alternating current of 5.13 mA and 50 kHz through the external-field wire and performed low-resolution real-space magnetic imaging on 167 nanopillars across 15×15 μm^2 near the edge of the wire (Fig. 4-6), from which we estimated the magnitude of the magnetic field gradient at each nanopillar location. We next performed high-resolution k-space imaging (followed by Fourier transforming into real space) of both the location of individual NV centers in several nanopillars with 30 nm spatial resolution, as well as the magnetic field difference ΔB_{ext} sensed by the NV centers within each nanopillar. As shown in Fig. 4-6, the resulting nanoscale maps of ΔB_{ext} are consistent with the local magnetic field gradient values obtained with low-resolution real-space imaging. Together, this hybrid real + k-space imaging demonstration provides a spatial dynamic range (FOV/resolution) of ~ 500. In future work we plan to integrate NV Fourier magnetic imaging with a wide-field real-space imager (for example, using a CMOS or charge-coupled device (CCD) camera) [90, 150, 205, 215], which would obviate the need for scanning and provide parallel and hence rapid real-space imaging across a wider FOV of > 1 mm [97], together with

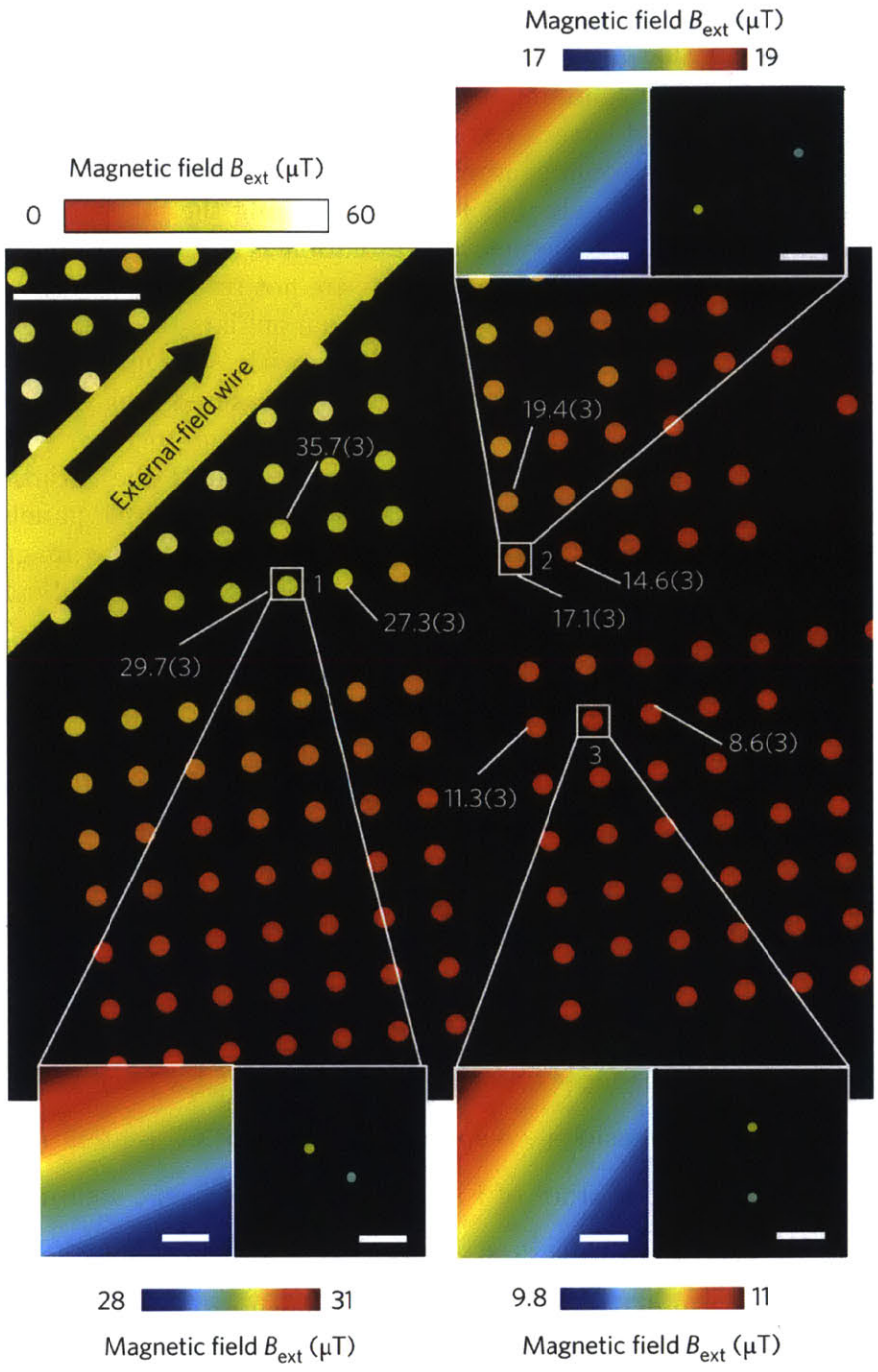

Figure 4-6: Fourier magnetic imaging with wide FOV and nanometer-scale resolution. (Continued on the following page.)

Figure 4-6: (Continued from the previous page.) The a.c. magnetic field produced by passing a 50 kHz, 5.13 mA electric current through the external-field wire (indicated by a thick yellow line at the top-left corner) is imaged using a hybrid real + k-space technique over a wide FOV spanning 167 diamond nanopillars. Imaged magnetic field amplitudes are indicated with a color scale, with numerical values (and associated uncertainties) given for some example nanopillars. A low-resolution real-space magnetic image is acquired over the full FOV by scanning the microscope across all nanopillars (see Section 4.7.2). The spatial resolution is limited by optical diffraction and NV centers within individual nanopillars are not resolved. Fourier (k-space) magnetic imaging is then performed on individual nanopillars to determine NV center positions and local a.c. magnetic field amplitudes with ~ 30 nm resolution (right boxes of inset panels). To check for consistency, the measured long-range magnetic field gradient provided by the low-resolution real-space image, together with the NV positions determined via Fourier imaging, are used to estimate the variation in a.c. magnetic field amplitude within each nanopillar (left boxes of inset panels). Good agreement is found between the measured and estimated values for the magnetic field difference between NV centers within each nanopillar (Appendix C.4). Scale bars: 2 μm (main figure) and 100 nm (insets).

nanoscale-resolution k-space imaging.

4.5 Compressed Sensing Speed-up

Finally, we have shown that the speed of NV Fourier magnetic imaging can be greatly enhanced by compressed sensing [44, 166]. We first acquired a fully sampled ($N = 2,048$ data points), one-dimensional, k-space image of two NV centers in sample B by sweeping the gradient (blue trace of Fig. 4-7a). In subsequent measurements we recorded data at $M = N/2^p$ ($p = 0, \ldots, 6$) randomly chosen k-space values, providing an N/M-fold speed-up (under-sampling) in data acquisition. For example, the red dots in Fig. 4-7a show data collected for $M = 128$ k-space values and hence a speed-up of $N/M = 16$. A Fourier transform of the fully sampled curve shows two NV centers separated by 116(4) nm (blue trace in Fig. 4-7b). The red traces in Fig. 4-7b

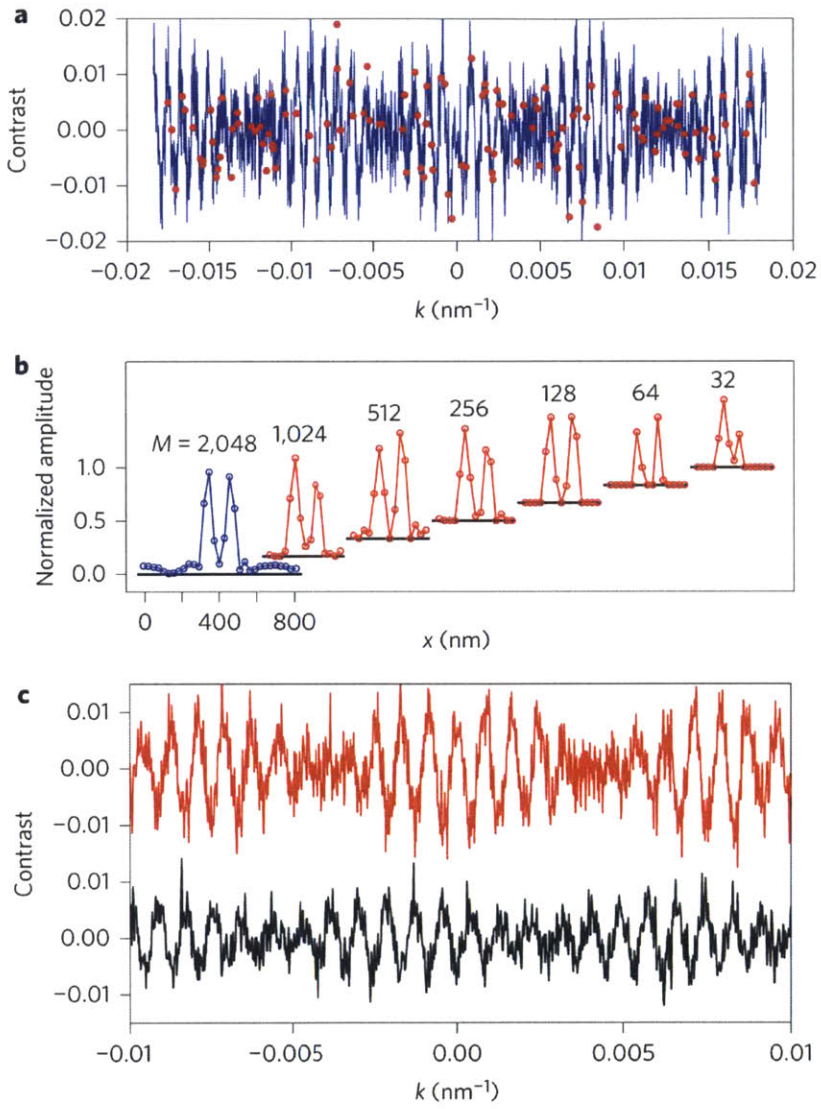

Figure 4-7: Compressed sensing speed-up of NV Fourier magnetic imaging. (Continued on the following page.)

Figure 4-7: (Continued from the previous page.) **a**, For two NV centers in sample B: fully sampled one-dimensional k-space signal with $N = 2,048$ data points (blue line) and randomly under-sampled k-space signal with $M = 128$ data points (red symbols). The under-sampling (speed-up) factor is $N/M = 16$. **b**, Blue trace: absolute value of the Fourier transform of fully sampled k-space data, indicating a real-space NV separation of 116 nm along the x axis. Red traces (offset for clarity): real-space signals reconstructed from under-sampled k-space data sets via compressed sensing techniques, in good agreement with fully sampled k-space data for $M \geq 128$. **c**, Inverse Fourier transform of data reconstructed via compressed sensing for $M = 128$ with (black trace) and without (red trace) an a.c. current (50 kHz, 10.26 mA) sent through an external-field wire. The observed phase shift between the data sets provides a measure of the magnetic field difference between the positions of the two NV centers, in good agreement with the results from fully sampled k-space data, thereby showing that compressed sensing reconstruction retains reliable information about imaged magnetic fields.

show the absolute values of real-space signals reconstructed from the under-sampled data using the l_1-minimization algorithm (see Section 4.7.3). For $M \geq 128$ we observe two peaks that match well with the NV locations given by the fully sampled data. This result is consistent with the criterion for faithful signal recovery: that is,

$$M \geq CS \log_2(N), \tag{4.5}$$

where S is the signal sparsity (equal to 2 in the example above) and C is a constant of order 1, which in this case is found to be ~ 5. For our experiments $CS \log_2(N) \approx 110$ and thus the signal was not recovered with high probability for $M < 128$. Importantly, we also demonstrated that the reconstructed real-space signal retains information about the magnetic field sensed by each NV center. We sent an alternating current of 10.26 mA and 50 kHz through the external-field wire, recorded k-space data for $M = 128$ points, and reconstructed real-space signals as described above. From the phase of the reconstructed signals we determined the difference between the magnetic fields sensed by the two NV centers to be $(5.0 \pm 0.5) \times 10^2$ nT, in reasonable agreement

with the value of $(6.3 \pm 0.8) \times 10^2$ nT obtained using fully-sampled k-space data, but with the benefit of 16-fold speed-up. The retention of NV phase information in data reconstructed by means of compressed sensing can be made explicit by computing the inverse Fourier transform of the reconstructed signal. In Fig. 4-7c we compare k-space signals obtained via such inverse Fourier transformations with (black trace) and without (red trace) current in the external-field wire. The observed phase shift between the two traces provides a direct illustration and measure of the magnetic field difference between the two NV centers, consistent with the above results.

4.6 Discussions

Our demonstration of Fourier magnetic imaging provides the first method for mapping NV positions and local magnetic fields in wavenumber or 'k-space', which is then Fourier-transformed to yield real-space images with both nanoscale resolution and wide FOV. The distinct advantage of this approach relative to real-space imaging is the spatially multiplexed signal acquisition across the full FOV, which enhances the SNR for typical NV center densities, enables a higher data acquisition rate that can be increased by more than an order of magnitude with compressed sensing, and allows one to probe classical or quantum correlations in samples by conducting simultaneous measurements using multiple, spatially separated NV centers. We also emphasize the relative simplicity of the apparatus needed for Fourier imaging, with the gradient microcoils used for phase-encoding being easily integrated with an optical microscope. We expect that NV Fourier magnetic imaging, which employs phase-encoding of the NV detector spins rather than of the sample spins as in previous Fourier techniques [190], will be applicable to a broad range of systems that can be placed on or near the diamond surface. Example applications in the physical sciences include probing quantum effects in advanced materials, such as frustrated magnetic

systems with skyrmionic ordering; spin liquids where quantum spin fluctuations prevent the system from ordering; low-dimensional systems such as graphene, as well as antiferromagnetic and multiferroic materials and topological insulators with quantized spin-carrying surface states. In the life sciences, NV Fourier magnetic imaging may allow nanoscale NMR spectroscopy [64] and structure determination of individual biomolecules, MRI within living cells and real-time, non-invasive mapping of functional activity in neuronal networks with synapse-scale resolution ($\sim$ 10 nm) and circuit-scale FOV ($>$ 1 mm). Anticipated technical improvements of NV Fourier imaging include (1) enhanced magnetic field sensitivity via optimization of diamond samples [204], optical collection efficiency [151] and spin-state optical contrast; (2) a 30-fold increase in the $k_{\max}$ value, by stronger magnetic field gradients generated by smaller microcoils and larger current and the use of dynamical-decoupling pulse sequences to extend NV spin coherence times [21, 22, 203]; and (3) parallel real-space image acquisition with a wide-field CMOS or CCD camera, which will provide immediate improvement in the spatial dynamic range (FOV/resolution) and enable the study of long-range, real-time dynamics such as neuronal activity that span length scales from a few nanometers to millimeters. Although instrumentation instabilities such as thermal fluctuations may pose technical challenges, we expect that sub-1 nm resolution is feasible. Straightforward extensions of the present technique should also allow NV Fourier imaging of electric fields [68], temperature [145] and pressure (J. Barry *et al.*, manuscript in preparation) with nanoscale resolution, wide FOV and compressed sensing speed-up, as well as application to other solid-state quantum spin systems such as point defects in silicon carbide [138].

4.7 Methods

4.7.1 Fabrication of nanopillars and gradient microcoils

Samples A and B were electronic-grade, single-crystal diamond chips with natural isotopic concentration of ^{13}C (1.1%), which were grown using chemical vapor deposition (Element 6 Corporation). Sample A was implanted with ^{14}N ions (dosage, 1×10^{10} cm^{-2}; energy, 85 keV). From the stopping and range of ions in matter simulations, the NV centers were estimated to be 100 nm below the diamond surface. Sample B was implanted with ^{15}N ions (dosage, 1×10^{12} cm^{-2}; energy, 14 keV) and the estimated NV depth was 20 nm. The conversion efficiency from implanted N ions to NV centers in both samples was estimated to be $\sim$ 1%. Typical NV spin dephasing times were $T_2^* \approx 1$ μs (sample A) and 500 ns (sample B), and the typical Hahn-echo spin coherence times were $T_2 \approx 50$ μs (sample A) and 30 μs (sample B). The magnetic field gradients used in the Fourier imaging demonstrations did not significantly affect NV spin coherence properties across the imaging FOV [238]. To fabricate diamond nanopillars, sample B was spin-coated with a 100-nm-thick layer of electron-beam resist (Dow Corning, XR-1541-006). Arrays of 400-nm-diameter circles were then patterned using an Elionix ELS-7000 electron-beam writing system with exposure dosage and beam energy set at 8,000 μC cm^{-2} and 100 kV, respectively. Tetra-methyl ammonium hydroxide (25%) was used to develop the resist and form the etch mask. The diamond crystal was then placed in an inductively coupled plasma (ICP) reactive-ion etching system and etched for 45 s with 30 s.c.c.m. of oxygen gas, 700 W ICP power and 100 W bias power at a chamber pressure of 10 mtorr. These parameters gave an etch depth of $\sim$ 150 nm. The gradient microcoils, microwave loop and external-field wire were fabricated on a polycrystalline diamond coverslip ($10 \times 10 \times 0.3$ mm^3) for optimized heat dissipation. The coverslip was spin-coated

with LOR 20B (MicroChem, bottom layer, ~ 2 μm) and Shipley S1805 (Dow Electronic Materials, top layer, ~ 400 nm) photoresists, exposed using a mask aligner, and the pattern was developed in a CD26 bath. A 30 nm Ti layer and a 970 nm Au layer were then deposited in an electron-beam evaporator, followed by lift-off in MicroChem Remover PG solution. Electrical resistance measurements, performed using a four-probe station, gave a value of ~ 1 Ω for each gradient microcoil. The diamond coverslip was bonded to the NV-containing diamond sample with optical adhesive, and a copper heat sink was attached to the back surface of the diamond coverslip to enhance heat dissipation.

4.7.2 Data analysis

Fourier magnetic imaging signals were recorded in k-space using the techniques described in the main text. A tapered-cosine windowing function with the taper coefficient set to 0.1 was applied to the k-space data and a symmetric fast Fourier transform algorithm implemented with MATLAB was used to obtain real-space images. No zero padding was done on the k-space data. Real-space pixel resolution therefore matched the true resolution of the imaging system. The SNR of real-space images acquired with this method increased with the square root of the number of data points, confirming the multiplex advantage of the Fourier imaging technique (Appendix C.6). The real-space images in Figs. 4-4, 4-5, and 4-6 were thresholded at 5σ above the noise level (where σ is the standard deviation of the noise) and NV centers were represented by circles centerd at the positions of the thresholded peaks, with diameters equal to the pixel resolution. For the wide FOV image of Fig. 4-6, the k-space sampling rate and number of sample points were held fixed for all nanopillars. For the magnetic field sensing data of Fig. 4-6, a calibration procedure was first performed by recording NV fluorescence as a function of current through the external-field wire

for each nanopillar in the FOV without phase encoding. The resultant magnetometry curves revealed the functional dependence of the magnetic field on the applied current for each nanopillar. For a fixed current, the magnetic field so determined was used as an offset value for the high-spatial-resolution phase-encoded magnetic field data recorded from individual NV centers within the nanopillar of interest. Magnetic field sensitivity was calculated as $(\sigma_B/dS_B)T^{1/2}$, where σ_B is the measurement noise, dS_B is the slope of the magnetometry curve, and T is the total data acquisition time. For the NV centers and measurement protocols employed in this work, the magnetic field sensitivity was ~ 1 μT Hz$^{-1/2}$.

4.7.3 Compressed sensing

In compressed sensing, signals are sampled at random and at a sampling frequency that may be lower than the Nyquist rate. Under assumptions of signal sparsity, recovery algorithms based on convex optimization can then be used to reconstruct the signal in a transform domain with high fidelity. In the present compressed sensing demonstration, the under-sampled k-space data were windowed with a tapered-cosine function (taper parameter of 1). A Fourier transform sampling matrix A of size $M \times N$ was created by picking M rows (corresponding to the sampled points) from an $N \times N$ discrete Fourier transform matrix. The real-space signal was reconstructed from the under-sampled data sets by minimizing the l_1-norm of the real-space signal $||\boldsymbol{x}_1||$ subject to the constraint $\boldsymbol{k} = A \cdot \boldsymbol{x}$, where $\boldsymbol{x}$ and $\boldsymbol{k}$ are column vectors of size N and M representing real-space and k-space data respectively. The convex optimization routine was implemented using MATLAB library functions made available by CVX Research (www.cvxr.com).

Chapter 5

Geometric Phase Magnetometry

Magnetometry is a powerful technique for the non-invasive study of biological and physical systems. A key challenge lies in the simultaneous realization of high magnetic field sensitivity and dynamic range. In interferometry-based magnetometry, a quantum two-level system acquires a dynamic phase in response to an applied magnetic field. However, due to the 2π periodicity of the phase, the sensitivity can be improved only in exchange for the dynamic range. Here we introduce a novel route towards high dynamic range magnetometry via measurements of the geometric phase. Our approach enables unwrapping of 2π phase ambiguity, enhancement of dynamic range by 400 times, and decoupling of sensitivity from dynamic range. By studying how geometric phase decoherence depends on adiabaticity with the power spectral density theory, we also find additional improvement in sensitivity in the nonadiabatic regime. Our results indicate that geometric phase is versatile for quantum sensing applications using various two-level spin and atomic systems.

5.1 Introduction

The geometric phase [29, 271] plays a fundamental role in a broad range of physical phenomena [110, 253, 108]. Although it has been observed in many quantum platforms [282, 256, 246, 158] and known to be robust against certain types of noise [58, 87], applications of geometric phase to modern technologies are limited to quantum simulation [161, 130] and computation [281, 159, 283]. When applied to magnetic field sensing, one encounters various unique and attractive aspects of geometric phase. In particular, we experimentally demonstrate three advantages: (1) extension of the dynamic range by resolving the 2π phase ambiguity via nonlinear field dependence; (2) decoupling of the sensitivity and maximum field enabled by additional geometrical degrees of freedom leading to a 400-fold enhancement in the dynamic range; and (3) additional improvement of sensitivity in the non-adiabatic regime. By introducing a power spectral density theory [21], we also find that adiabaticity plays an important role in controlling the degree of coupling to the environmental noise.

5.2 Concept of Dynamic and Geometric Phase Magnetometry

In magnetometry using a two-level system, an unknown magnetic field B can be estimated by measuring the relative energy shift between two energy levels induced by that field (Section 5.7). A commonly used approach to detect this energy shift is to measure the dynamic phase accumulated in a Ramsey-type interferometry sequence consisting of oscillating field pulses as illustrated in Fig. 5-1a. The initial $\pi/2$ pulse prepares the system in a superposition state between two levels. In the presence of an external magnetic field B along the quantization axis, the state evolves under the

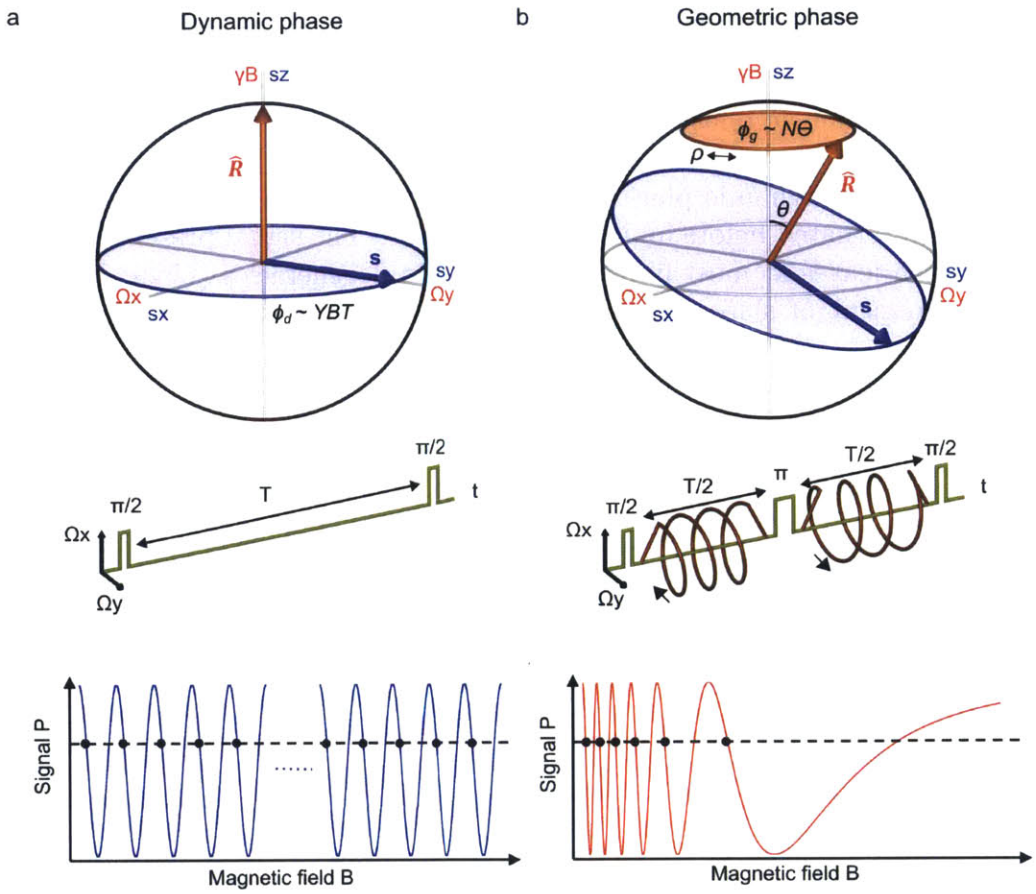

Figure 5-1: Concept of magnetometry using dynamic and geometric phase. (Continued on the following page.)

Figure 5-1: (Continued from the previous page.) **a**, Dynamic phase magnetometry. The Bloch vector $\boldsymbol{S} = (s_x, s_y, s_z)$ (blue arrow), initially prepared in a superposition state between two levels, precesses about the fixed Larmor vector $\boldsymbol{R} = (0, 0, \gamma B)$ (red arrow). During the interaction time T between two $\pi/2$ pulses, the spin accumulates a dynamic phase $\phi_d = \gamma BT$, proportional to the angle swept by the Bloch vector on the equator. The phase is mapped to a population difference signal $P = \cos\phi_d$. Due to the 2π phase periodicity, infinite number of magnetic field values (black dots) give the same signal, leading to an ambiguity problem. **b**, Geometric phase magnetometry. By additional off-resonant driving, the Larmor vector is made to rotate about the z-axis N times, $\boldsymbol{R}(t) = (\Omega\cos\rho(t), \Omega\sin\rho(t), \gamma B)$, where $\rho(t) = 4\pi Nt/T$. The state acquires a geometric phase $\phi_g = N\Theta$ proportional to the number of rotations N and the solid angle $\Theta = 2\pi(1 - \cos\theta)$ subtended by the trajectory of the Larmor vector. To cancel the dynamic phase and double the geometric phase, the direction of precession is alternated before and after the π pulse. The signal presents a chirped oscillation, which leaves at most finite magnetic field degeneracies (black dots). Additional measurement of slope resolves this ambiguity because the slope decreases monotonically.

Hamiltonian

$$H = \frac{1}{2}\hbar\gamma B\sigma_z, \tag{5.1}$$

where γ denotes the gyromagnetic ratio and σ_z the z-component of the Pauli spin vector. During the interaction time T, the Bloch vector $\boldsymbol{s}(t)$ depicted on the Bloch sphere precesses around the fixed Larmor vector

$$\boldsymbol{R} = (0, 0, \gamma B), \tag{5.2}$$

and acquires a dynamic phase

$$\phi_d = \gamma BT. \tag{5.3}$$

The next $\pi/2$ pulse maps this phase on to a population difference (Appendix D.1)

$$P = \cos\phi_d. \tag{5.4}$$

This dynamic phase approach possesses two well-known shortcomings. First, the sinusoidal nature of the population difference signal leads to a 2π phase ambiguity. Since the dynamic phase is linearly proportional to the magnetic field, for any measured signal P_{meas}, there are infinite magnetic field ambiguities:

$$B_m = (\gamma T)^{-1}(\cos^{-1} P_{\text{meas}} + 2\pi m), \tag{5.5}$$

where $m = 0, \pm 1, \pm 2 \cdots \pm \infty$. Thus, the dynamic range of magnetic field that one can determine without modulo 2π phase ambiguity is limited to one cycle of oscillation (Appendix D.2, Fig. D-2):

$$B_{\text{max}} \propto 1/T. \tag{5.6}$$

Second, a trade-off between sensitivity and dynamic range. The interaction time also restricts the shot-noise-limited magnetic field sensitivity:

$$\eta \propto 1/T^{1/2}. \tag{5.7}$$

Consequently, an improvement in dynamic range comes at the cost of a reduction in the sensitivity (Appendix D.3). The quantum phase estimation algorithm [36, 191] or non-classical states [35, 96] can alleviate these disadvantages; however, they require either large overhead resource time or realization of long-lived entangled or squeezed states.

The central idea of geometric phase magnetometry is to use the Berry sequence, introduced in ref. [158]. The sensor acquires a geometric phase due to additional off-resonant state mixing pulses with control parameters cycled along a closed path as illustrated in Fig. 5-1b. Three control parameters describe the Hamiltonian under a rotating wave approximation:

$$H = \frac{1}{2}(\Omega \cos\rho\sigma_x + \Omega \sin\rho\sigma_y + \gamma B\sigma_z), \tag{5.8}$$

where Ω is the Rabi frequency, ρ is the phase of driving field, and $\boldsymbol{\sigma} = (\sigma_x, \sigma_y, \sigma_z)$ is the Pauli spin vector. By sweeping the phase, the Larmor vector

$$\boldsymbol{R}(t) = (\sin\theta\cos\rho, \sin\theta\cos\rho, \cos\theta), \tag{5.9}$$

where $\cos\theta = \gamma B/(\Omega^2 + (\gamma B)^2)^{1/2}$, rotates around the z axis. The Bloch vector $\boldsymbol{s}(t)$ then undergoes precession around this rotating Larmor vector. If the rotation is adiabatic (i.e., adiabaticity parameter $A \equiv \dot{\rho}\sin\theta/2R \ll 1$), the system acquires a geometric phase proportional to the solid angle

$$\Theta = 2\pi(1 - \cos\theta) \tag{5.10}$$

subtended by the trajectory and the number of phase rotations N. We insert this rotation twice during each half of the interaction times in an echo sequence. By alternating the direction of rotation, the geometric phase doubles: (Section D.1)

$$\phi_g = 2N\Theta. \tag{5.11}$$

Importantly, the dynamic phase is cancèled because of an echo operation. Finally, the population difference signal becomes

$$P(B) = \cos\left[4\pi N\left(1 - \frac{\gamma B}{\sqrt{(\gamma B)^2 + \Omega^2}}\right)\right]. \tag{5.12}$$

The signal exhibits a chirped oscillation as a function of the external field. There are at most "finite" field ambiguities that give the same signal P_{meas}. Furthermore, it is

possible to resolve the ambiguity and determine the field uniquely by measuring the slope dP/dB (Appendix D.2, Fig. D-2). From the form of Eq. (5.12) it is evident that the signal and slope asymptotically reach unity and zero, respectively at large B. Hence, we define the dynamic range as the magnetic field value that gives the last minimum in the signal:

$$B_{\max} \propto \Omega N^{1/2} T^{0}. \tag{5.13}$$

If the magnetic field is below this value, one can make a measurement with the best sensitivity

$$\eta \propto \Omega^{-1} N T^{1/2} \tag{5.14}$$

by adding a phase offset [249], which can be, for example, realized by tuning the transition frequency of state-mixing field to the largest slope of the magnetometry signal (Appendix D.3).

5.3 Demonstration of Dynamic and Geometric Phase Magnetometry

Geometric phase magnetometry experiments are implemented with an electronic spin associated with the nitrogen-vacancy (NV) color center in diamond (Fig. 5-2). Among many magnetometers, NV centers offer particularly high spatial resolution under ambient conditions [249, 176, 19] and have therefore found wide-ranging applications in condensed matter physics [250, 168], microbiology [150, 97], and geology [90]. At an applied bias field of 96 G, the degeneracy of the $m_s = \pm 1$ levels is lifted. The two-level system in this work consists of the ground state magnetic sublevels $m_s = 0$ and $m_s = -1$, which can be coherently addressed by applied microwave fields. Hyperfine interaction between the NV electronic spin and the host ^{14}N nuclear spin further

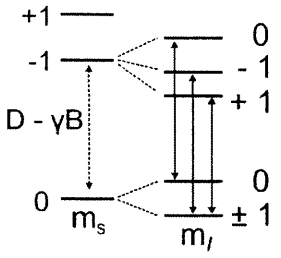

Figure 5-2: The energy diagram of NV center. The ground state of NV center is a spin triplet. The magnetic sublevels $m_s = 0$ and ± 1 are split by $D = 2\pi \times 2.87$ GHz. An external magnetic field introduces Zeeman splitting between the $m_s = \pm 1$ states with a gyromagnetic ratio of $\gamma = 2\pi \times 28$ GHz T^{-1}. The $m_s = 0$ and -1 states define the two-level system in this work. Due to interactions with the host ^{14}N nuclear spin, there are three hyperfine levels $m_I = 0, \pm 1$, split by ± 2.16 MHz.

splits the levels into three states, each separated by 2.16 MHz. Upon green laser illumination, the NV center exhibits spin-state-dependent fluorescence. Thus, one can measure the spin states by detecting the change in fluorescence (see Section 5.7 for more details).

To demonstrate how the choice of interaction time gives rise to interdependence between the sensitivity and dynamic range for the case of dynamic-phase magnetometry, we first conducted spin-control experiments using a Ramsey sequence. The NV fluorescence signal was recorded as a function of the interaction time T between the two microwave $\pi/2$ pulses. Signal contributions from the three hyperfine transitions of the NV spin result in the beating behavior seen in Fig. 5-3a. We fixed the interaction time at $T = 0.2, 0.5, 1.0$ μs and varied the external magnetic field. Because of the periodicity of signal, the measured signal gives rise to a 2π phase ambiguity. The oscillation period decreases as the interaction time is increased, which indicates a decrease in the dynamic range. On the other hand, the sensitivity, which depends on the maximum slope of the signal, improves as the interaction time increases. By fitting the result to a sinusoid, one can extract the oscillation period and slope, which are

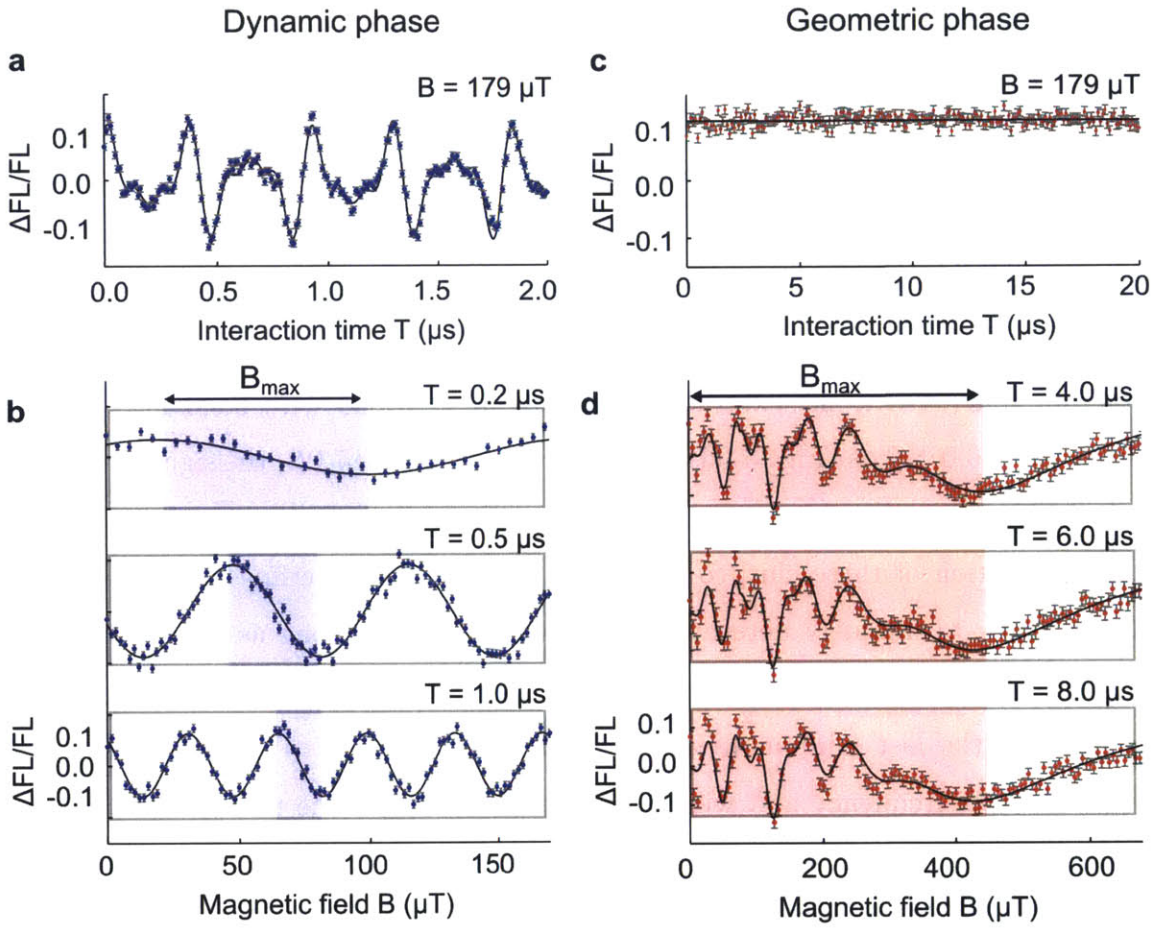

Figure 5-3: Demonstration of dynamic and geometric phase magnetometry using a single electronic spin qubit in diamond. **a**-**d**, Blue and red dots represent measured magnetometry data for dynamic phase (**a**, **b**) and geometric phase (**c**, **d**), respectively. The vertical axis is the signal, defined by the change of signal fluorescence count (ΔFL) normalized by the reference fluorescence count (FL). Error bars are 1σ photon shot-noise. Black lines show fit to a model provided in the main text. Blue and red shaded regions represent the dynamic range. The beating of three hyperfine oscillations is evident in **a**. In dynamic phase magnetometry, the oscillation period decreases as the interaction time increases, indicating a trade-off between the sensitivity and dynamic range (**b**). Geometric phase magnetometry signal in **c** shows independence of T. The dynamic range is defined at the last minimum (**d**).

used to calculate the sensitivity and dynamic range. We repeated this measurement and analysis for various T values and obtained $\eta \propto T^{-0.49(6)}$ and $B_{\max} \propto T^{-0.96(2)}$ as expected (Fig. D-3).

Next, we show the first advantage of geometric phase magnetometry i.e. the extension of dynamic range via 2π phase unwrapping using chirped oscillation signal. Presented in Fig. 5-3c is the geometric phase signal as a function of interaction time under fixed control parameters of $\Omega/2\pi = 5$ MHz, $N = 3$. It is clear from this result that the geometric phase, as opposed to the dynamic phase, doesn't depend on the interaction time. Next, the external magnetic field is varied with fixed interaction times $T = 4.0, 6.0, 8.0$ μs (Fig. 5-3d). As expected from Eq. (5.12), the signal exhibits identical chirped oscillations for all T values. Even though the signal comprises of a superposition of three chirped oscillations due to the hyperfine interactions, it is still possible to uniquely determine the magnetic field as long as the field value falls within the oscillatory range (Appendix D.2). Thus, the dynamic range can be defined at the last minimum point. By fitting the result to a model, one can extract the Rabi frequency and winding number, and determine the dynamic range and sensitivity. We also measure the dependence of geometric phase magnetometry signals on Ω and N and find that the scaling of sensitivity and dynamic range is $B_{\max} \propto \Omega^{0.9(1)} N^{0.52(5)} T^{0.02(1)}$ and $\eta \propto \Omega^{1.2(5)} N^{-0.92(1)} T^{0.46(1)}$ (Fig. D-1, D-2, D-3).

5.4 Sensitivity and Field Dynamic Range

To demonstrate the second advantage of geometric-phase magnetometry, we plot sensitivity and dynamic range against each other in Fig. 5-4. The sensitivity is measured directly at small B, whereas the dynamic range is calculated from the measured values of N and Ω. In the dynamic phase approach, since the interaction time is the only control parameter, all data points are plotted on a straight diagonal

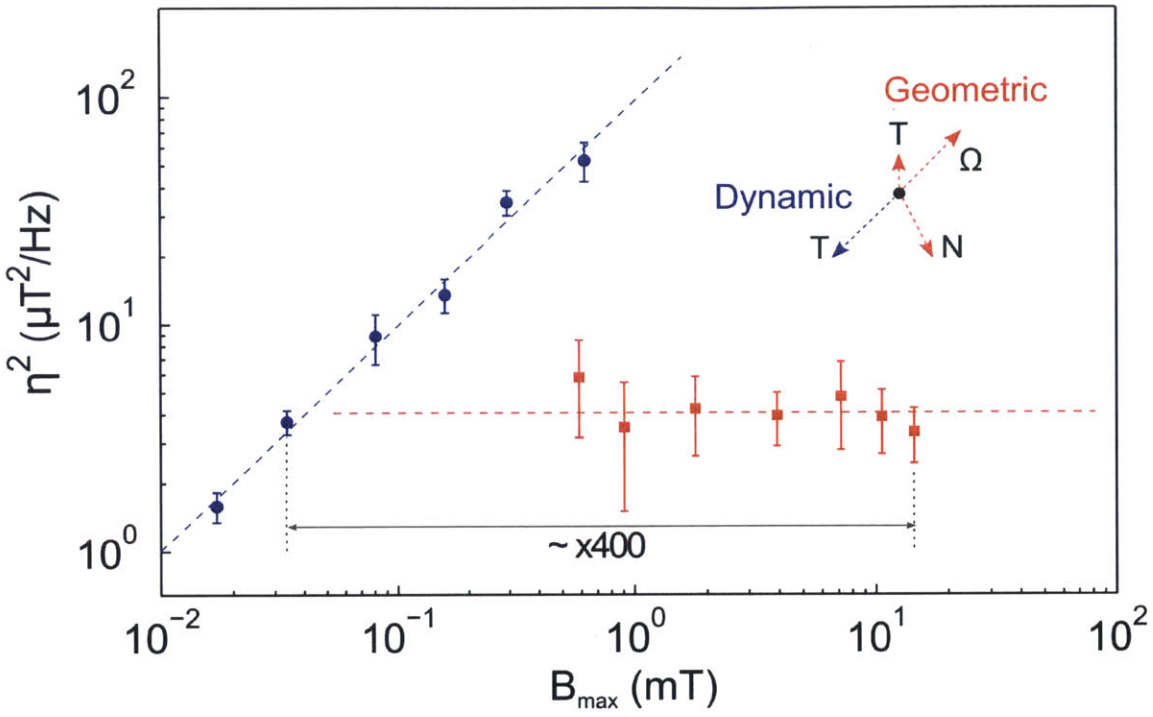

Figure 5-4: Decoupling of magnetic field sensitivity and dynamic range. Blue dots and red squares represent the measured dynamic and geometric phase magnetometry data, respectively. Dashed lines are linear fitting of the data. The sensitivity η is evaluated at the largest slope of magnetometry curves, and the dynamic range $B_{\max}$ is determined by the values of Rabi frequency and winding number extracted from fitting. Dashed arrows indicate the orientation of control parameters Ω, N, T behaving as independent vectors on the $(\eta^2, B_{\max})$ map. Since a Ramsey sequence has only a single control parameter (T), there is a unique relation between the sensitivity $(\eta \propto T^{-1/2})$ and field range $(B_{\max} \propto T^{-1})$: $\eta^2 \propto B_{\max}$. In contrast, three degrees of freedom are available for a Berry sequence, and thus the sensitivity $(\eta \propto \Omega^{-1} N T^{1/2})$ can be chosen independently of the dynamic rang $(B_{\max} \propto \Omega N^{1/2} T^0)$. For example, larger $B_{\max}$ with a constant η is obtainable by increasing Ω and N while keeping T and the ratio Ω/N fixed.

line parameterized by T. The T_2^* coherence time sets the maximum limit on the available interaction time. Geometric-phase magnetometry, in contrast, has three control parameters (T, N, and Ω), which behave like independent vectors on the $(\eta^2, B_{\max})$ plot. For example, as demonstrated in Fig. 5-4, the field range can be increased without changing sensitivity by increasing N and Ω while keeping the ratio N/Ω fixed. From these measurements, we demonstrate a 10-fold improvement in the sensitivity for an accessible field-range of $\sim$ 10 mT, and 400-fold enhancement in the dynamic range at a sensitivity of $\sim$ 2 μT Hz$^{-1/2}$. Similarly, the sensitivity can be improved without changing dynamic range by decreasing the interaction time. However, one cannot choose an arbitrary small value for interaction time because the adiabaticity condition ($A \approx N/\Omega T \ll 1$) needs to be satisfied (Fig. D-4).

5.5 Geometric Phase Coherence

The experiments described above were conducted in the adiabatic regime ($A \ll 1$). By going to the non-adiabatic limit, we observe the third advantage of geometric-phase magnetometry – additional improvement in sensitivity. Using the adiabaticity parameter $A \approx N/\Omega T$, the sensitivity can be recast as $\eta \propto A^{-1}T^{-1/2}$. This scaling motivates us to investigate the maximum available interaction time as a function of adiabaticity parameter. A noise spectral density analysis in the frequency domain is particularly useful for studying how environmental noise affects geometric phase coherence. The exponential decay of spin coherence $W(T) \sim \exp(-\chi(T))$ is characterized by the decoherence function $\chi(T)$, given by

$$\chi(T) = \int_0^\infty \frac{d\omega}{\pi} S(\omega) \frac{F_1(\omega T)}{\omega^2} + A^2 \int_0^\infty \frac{d\omega}{\pi} S(\omega) \frac{F_0(\omega T)}{\omega^2} \tag{5.15}$$

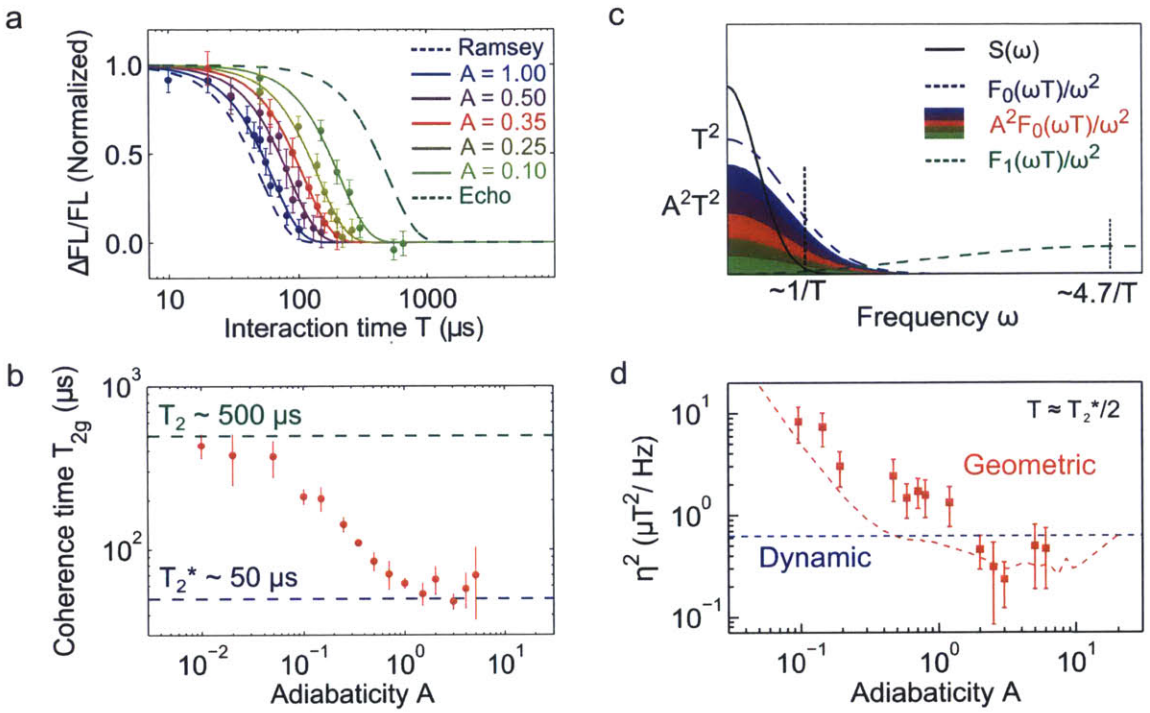

Figure 5-5: Geometric phase decoherence and sensitivity improvement in the nonadiabatic regime. **a**, Normalized geometric phase signal as a function of interaction time T for various adiabaticity parameter values. Color dots represent the measured data, and solid color lines are exponential fit $\sim \exp(T/T_{2g})^2$. The blue and green dashed lines indicate T_2^* and T_2 decay of dynamic phase signal measured with a Ramsey and Hahn-echo sequence, respectively. **b**, Measured coherence time T_{2g} as a function of adiabaticity parameter A. Three regimes appear: (i) For $A < 0.1$, $T_{2g} \sim T_2$, (ii) for $0.1 < A < 1.0$, $T_{2g} \sim 1/A$, and (iii) for $A \sim 1.0$, $T_{2g} \sim T_2^*$. **c**, Graphical representation of decoherence mechanism represented in the frequency domain. The decoherence function consists of noise spectral density function $S(\omega)$ (black), echo sequence filter function $F_1(\omega T)/\omega^2$ (dashed green line), and geometric sequence filter function $A^2 F_0(\omega T)/\omega^2$ (filled color area, the same color-coding as in (**a**)), which vanishes in the limit $A \to 0$ and reaches the Ramsey sequence function $F_0(\omega T)/\omega^2$ (dashed blue line) in the limit $A \to 1$. **d**, Measured magnetic field sensitivity (red squares) plotted against adiabaticity parameter A using a fixed interaction time of $T \approx T_2^*/2$ (dashed blue line). The dashed red line shows the lower limited of the sensitivity calculated by a numerical simulation assuming the maximum signal contrast. The simulation doesn't include the contrast reduction due to the hyperfine modulation, whose relative amplitudes were indeterminable from the measurements.

where $S(\omega)$ is a spectral density function that describes the noise from the environment, $F_0(\omega T) = 2\sin^2(\omega T/2)$ and $F_1(\omega T) = 8\sin^2(\omega T/4)$ are the filter functions for geometric and dynamic phase (Appendix D.4). The first and second terms describe contributions to the spin decoherence from the dynamic and geometric phase accumulation, respectively.

Fig. 5-5a shows the decay of geometric phase signal as a function of interaction time T for adiabaticity values between $A = 0.1 - 1.0$. As shown in Eq. (5.15), the overlap integral between $S(\omega)$ and $A^2F_0(\omega T)/\omega^2$ gives the decoherence. Thus, we find that the adiabaticity parameter is responsible for tuning the degree of coupling to the environment. Figure 5-5b shows the geometric phase coherence time T_{2g} extracted by fitting $W(T) \sim \exp[-(T/T_{2g})^2]$ to the decay curves in Fig. 5-5a. We observe three regimes of decoherence mechanism in this experiment, which can be understood by using a simple diagram in Fig. 5-5c. First, for $A < 0.1$, the dynamic term of decoherence function is responsible for decoherence ($T_{2g} \sim T_2 = 500$ μs) because the geometric term is negligibly small. Second, for $0.1 \leq A < 1.0$, the coherence time is inversely proportional to adiabaticity ($T_{2g} \sim 1/A$), as expected from Eq. (5.15). Third, at $A \approx 1.0$, the geometric decoherence function equals that given by the Ramsey sequence ($T_{2g} \sim T_2^* = 50$ μs). Furthermore, in the non-adiabatic limit $A \gg 1.0$, the rotation of Larmor vector averages out and only the z-component of Larmor vector remains. Thus, the Berry sequence becomes a Hahn-echo sequence and the coherence time is expected to bounce back to T_2.

Finally, we study the limit of sensitivity in the non-adiabatic regime. Once the geometric manipulation becomes non-adiabatic, the Bloch vector no longer follows the Larmor vector, and the time evolution of the state is analytically unsolvable. Consequently, the expression of geometric phase signal and the scaling of sensitivity and dynamic range also become invalid. Nonetheless, the spin state evolution is deterministic, and magnetic field sensing is still feasible. In Fig. 5-5d, we plot the

sensitivity measured at the largest slope of magnetometry curve as a function of A. We find that the sensitivity of geometric phase magnetometry keeps improving in the non-adiabatic regime until surpassing that obtained by dynamic phase.

5.6 Discussions

In summary, we have demonstrated a new approach towards geometric-phase magnetometry. By resolving the 2π phase ambiguity using the nonlinear behavior of geometric phase magnetometry curve, the dynamic range is extended by two orders of magnitude. Two new geometrical parameters (N, Ω) then decouple the sensitivity and dynamic range. In the non-adiabatic regime, the geometric phase approach gives better sensitivity than the dynamic phase approach does. We also find that adiabaticity is a key parameter for controlling the coupling between the spin and environmental noise during geometric manipulation. Dynamical decoupling [60] would further extend the geometric phase coherence, which may then enable the probing of extremely slow dynamics in the environmental noise with high spectral resolution. Finally, the generality of this approach makes it directly applicable to the measurement of energy shift in other quantum systems, such as trapped ions, ultracold atoms, and solid state spins, which may open new avenues for practical application of the geometric phase.

5.7 Methods

5.7.1 NV diamond sample

The diamond chip used in this experiment is an electronic-grade single-crystal cut along the [110] direction into a volume of $4 \times 4 \times 0.5$ mm^3 (Element 6 Corporation). A

high-purity chemical vapor deposition (CVD) layer with 99.99 % ^{12}C near the surface contains preferentially oriented NV centers. The estimated N and NV densities are 1×10^{15} and 3×10^{12} cm^{-3}, respectively. The ground state of NV center consists of a spin triplet with the $m_s = 0$ and ± 1 Zeeman sublevels split by $2\pi \times 2.87$ GHz due to spin-spin interactions. The basis of the spin qubit in this work consists of the $m_s = -1$ and 0 ground states. Microwave irradiation allows coherent manipulation of the ground states. The coherence time scales are $T_1 \sim 1$ ms, $T_2 \sim 500$ μs, and $T_2^* \sim 50$ μs.

5.7.2 Confocal scanning laser microscopy

The geometric phase magnetometry measurements using single NV centers is conducted using a home-built scanning laser microscopy system (Fig. 5-6). A three-axis motorized stage (Micos GmbH) moves the diamond sample in three dimensions for confocal scanning. An acousto-optic modulator (Isomet Corporation) operated at 80 MHz allows time-gating of a 400 mW, 532 nm diode-pumped solid state laser (Changchun New Industries). An oil-immersion objective (100x, 1.3 NA, Nikon CFI Plan Fluor) focuses the green laser pulses onto the NV center. Red fluorescence from NV centers passes through the same objective and goes into a silicon avalanche photodetector (Perkin Elmer SPCM-ARQH-12) through a single-mode fiber cable with a mode-field-diameter of ~ 5 μm (Thorlab). The NV spin initialization and readout pulses are 3 μs and 0.5 μs, respectively. The change of fluorescence signal is calculated from $\Delta FL = FL_+ - FL_-$, where $FL_\pm$ are the fluorescence counts obtained after a spin projection using a microwave $\pi/2$-pulse along the $\pm x$-axis, respectively. For each measurement, the fluorescence count FL when the spin is in the $m_s = 0$ state is also measured as the reference. The temperature of the confocal scanning laser microscope system is monitored by a 10k thermistor (Thorlab) and stabilized

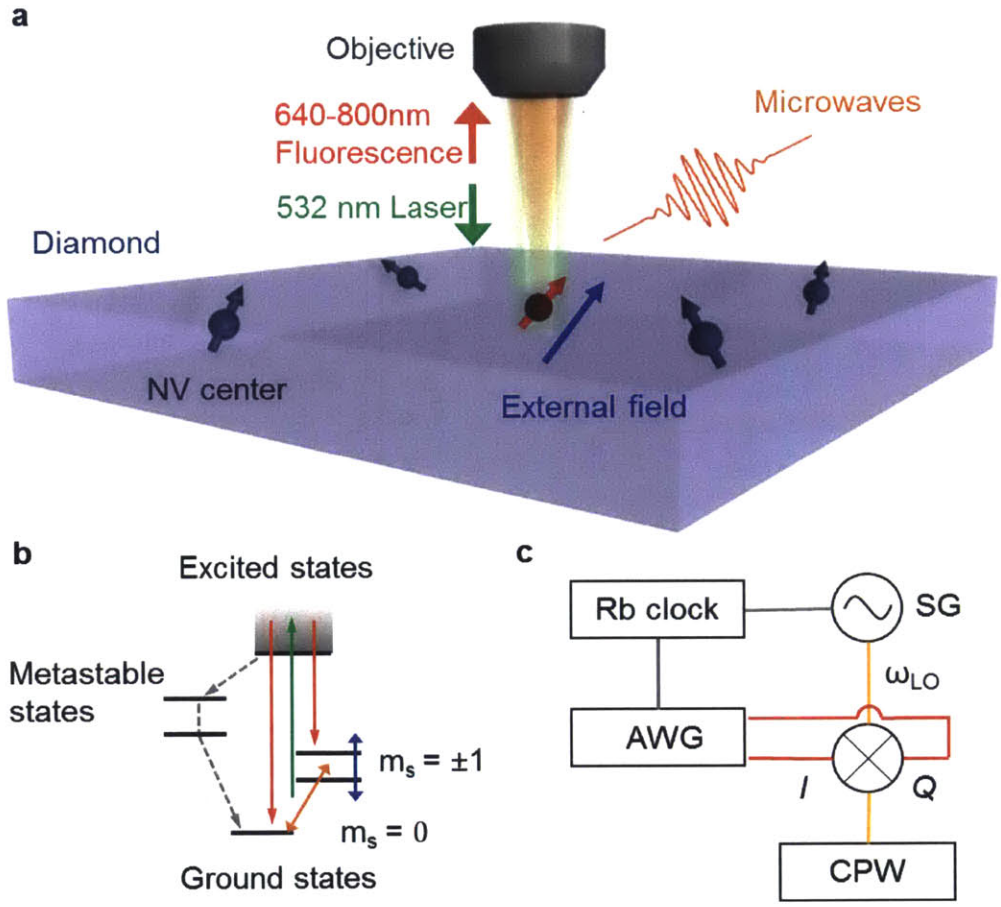

Figure 5-6: Geometric phase magnetometry setup. **a**, **b**, Schematic of geometric phase magnetometry setup. The diamond chip hosting NV centers is integrated into a confocal laser scanning microscope. Microwave fields (wavy orange line) produced by a gold coplanar waveguide coherently drive the $m_s = 0$ and ± 1 ground states, split by $D = 2\pi \times 2.87$ GHz. An external magnetic field (blue arrow) created by an electromagnetic coil introduces Zeeman splitting between the $m_s = \pm 1$ states. **c**, Schematic of the microwave delivery system. A signal generator (SG, Agilent E4428C) provides the carrier microwave signal with a frequency of $\omega_{\mathrm{LO}} \sim 3$ GHz (yellow lines). The microwave pulses for Berry phase magnetometry are generated by an arbitrary waveform generator (AWG, Tektronix AWG 5014C) and sent to the I/Q channels (red lines) of the IQ mixer (Marki IQ 1545 LMP). The output signal from the IQ mixer is delivered to a gold coplanar waveguide (CPW). To reduce the phase jitter noise, in-laboratory Rubidium clock (Stanford Research Systems FS725) phase-locks the signal generator and AWG at 10 MHz.

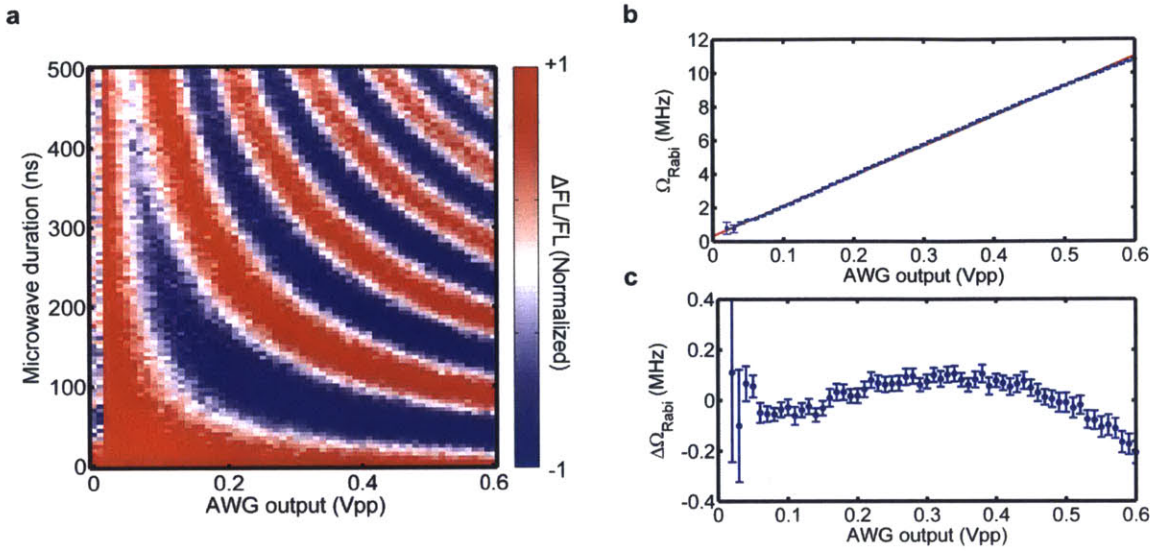

Figure 5-7: Calibration of Rabi frequency as a function of AWG output voltage. **a**, Normalized Rabi signal, measured as a function of the AWG output voltage and microwave pulse duration. **b**, Reduced Rabi frequency values $\Omega_{\text{Rabi}} = \Omega/2\pi$ in units of MHz obtained by fitting to a sinusoidal function at each voltage. The blue dots represent measurements, and the red line is a linear fit. **c**, To evaluate the nonlinearity of Rabi frequency as a function of AWG output voltage, the difference between the measured value and linear fit is plotted. The nonlinearity of the Rabi frequency is less than 0.2 MHz. This small nonlinearity can be attributed to the power compression by the I/Q mixer, whose 1 dB compression point is measured to be 1.0 Vpp.

to within 0.05 °C using a 15 W heater controlled with a PID algorithm.

5.7.3 Hamiltonian parameter control system

Rabi frequency, microwave phase, and magnetic field are key variables of this work. It is thus crucial to calibrate the microwave driving system and magnetic field control system beforehand. The microwave pulses for geometric phase magnetometry are generated by mixing high frequency ($\sim$ 3 GHz) local oscillator signal and low frequency ($\sim$ 50 MHz) arbitrary waveform signal using an IQ mixer (Fig. 5-6). The Rabi frequency and microwave phase are controlled by the output voltage of arbitrary

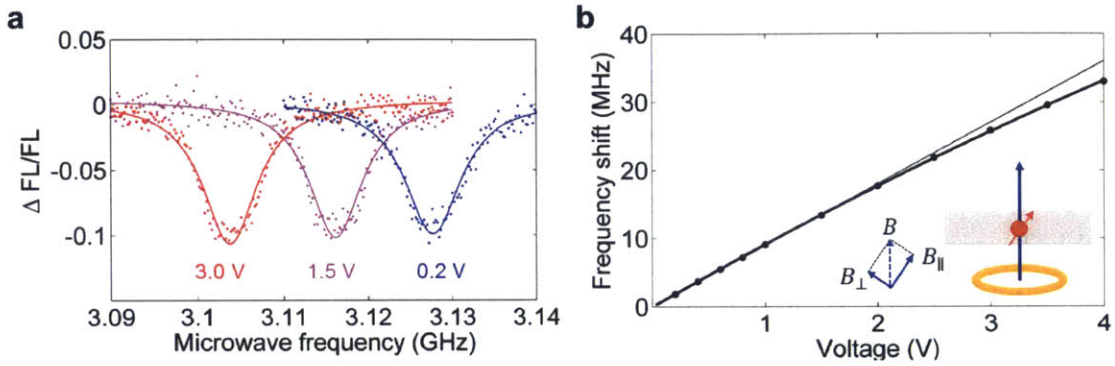

Figure 5-8: Magnetic field calibration with electron spin resonance. **a**, Continuous electron spin resonance (ESR) measurement under an external magnetic field. First, to split the $m_s = \pm 1$ states, a static field of $B_0 = 93$ G is applied along the [111] NV axis using a permanent magnet, which sets the $m_s = 0, +1$ resonance peak at 3.13 GHz. Next, an additional external field B is applied using a 40-turn electromagnetic coil placed $h = 0.5$ mm above the NV center. The coil is also connected to a 150 Ω resistor in series. A high-stability voltage controller provides a high-precision control of an electric current through the coil. An output voltage setting of 3.0 V gives $I = 0.02$ A, corresponding to a magnetic field of $B = \mu_0 NI/4\pi h \sim 16$ G in the direction perpendicular to the [100] diamond surface. ESR lines are measured for $V = 0.2, 1.5$, and 3.0 V (dots). The peak frequency is extracted by Gaussian fitting (solid lines). **b**, Absolute value of the measured frequency shift as a function of applied voltage (dots). The external field has the longitudinal and transverse components with respect to the NV axis: $\boldsymbol{B} = (B_\parallel, B_\perp)$. The diagram, the side-view of the magnetometry setup, shows the diamond (gray box), NV axis (red arrow), copper electromagnet (orange circle), and magnetic field line (blue arrow). The energy levels of $m_s = 0$ and $+1$ are obtained by solving the eigenvalue problem, $\det(H - \lambda I) = 0$, where $H/\hbar = (D + \gamma B_0 + \gamma B_\parallel)\sigma_z/2 + \gamma B_\perp \sigma_x/2$ is the two-level system Hamiltonian. Thus, for $\gamma B \ll D$, the measured frequency shift exhibits a quadratic term as a perturbation: $B_\parallel + 2\gamma B_\perp^2/(D + \gamma B_0)$ (thick solid curve). For small B, a linear fitting gives $\Delta B/V = 0.5$ G V^{-1} (thin line).

waveform generator (Fig. 5-7). The microwave pulses are amplified (Mini-circuits ZHL-16W-43-S+) and sent through a gold coplanar waveguide (10 μm gap, 1 μm height) fabricated on a glass coverslip by the photo-lithography technique. An external magnetic field for magnetometry demonstration is created by sending an electric current through a copper electromagnetic coil (4 mm diameter, 0.2 mm thick, $n = 40$ turns, $R = 0.25$ Ohm resistance) placed $h = 0.5$ mm above the diamond surface. The electric current is provided by a high-stability DC voltage controller (Agilent E3640A). To enable a finer scan of electric current with a limited voltage resolution, another resistor with 150 Ohm is added in series. Thus, a DC power supply voltage of 3 V approximately corresponds to $I = 0.02$ A, which creates an external field of $B = \mu_0 nI/4\pi h \sim 16$ G. One can determine the change of external magnetic field as a function of DC power supply voltage $\Delta B(V)$ by measuring the shift of resonance peak Δf in the continuous electron spin resonance (ESR) spectra using $\Delta f = \gamma \Delta B$. The obtained result is $\Delta B/V = 0.5$ G V^{-1} (Fig. 5-8). The Joule heat produced by the coil is $P = I^2 R = 10^{-4}$ W. The mass and heat capacity of the coil are 0.15 g and 0.06 J K^{-1}, respectively. Thus, the temperature rise is at most 2 mK s^{-1}. Since the temperature coefficient of resistivity for copper is 0.00386 K^{-1}, the change of resistance due to Joule heat is negligible.

5.7.4 Numerical methods for geometric phase simulation

All simulations in this work are carried out by computing the time-ordered time evolution operator at each time step.

$$U(t_i, t_f) = \hat{T}\exp\left(-i\int_{t_i}^{t_f} H(t)dt\right) = \prod_{j=1}^{N} \exp\left[-i\Delta t H(t_j)\right], \tag{5.16}$$

where t_i and t_f are the initial and final time, respectively, $\hat{T}$ is the time-ordering operator, Δt is the time step size of the simulation, $N = (t_f - t_i)/\Delta t$ is the number of time step, and $H(t)$ is the time-dependent Hamiltonian (Eq. (5.8)). The algorithm is implemented with MATLAB.

Chapter 6

Outlook

This thesis work demonstrated three novel techniques for controlling electronic spins associated with the NV centers in diamond with a primary application in magnetic field sensing and imaging. This last chapter discusses the potential and new movements of employing these techniques to other quantum technologies. In particular, wide-field illumination for "quantum diamond microscopy" [150], presented in Chapter 3, is a key technique for high sensitivity quantum sensing of various samples; magnetic field gradient developed for phase encoding [14] in Chapter 4, provides a powerful approach for selectively controlling proximal spins in a scalable spin network for quantum computation; and geometric control, introduced in Chapter 5, offers a new modality for simulating various topological phenomena in condensed matter systems and constructing universal quantum gates that are robust against noise and errors.

6.1 Wide-Field Illumination

The magnetic field sensitivity scales as $\eta \propto n^{-1/2}$, where n is the number of NV centers in the detection volume [205]. Thus, an ensemble of NV centers used as a

magnetic sensor offers high sensitivity as well as large field-of-view. This section discusses various modalities of ensemble spin control for quantum sensing.

6.1.1 Quantum diamond microscopy

As discussed in Chapter 3, the prototype of quantum diamond microscope offered a field-of-view of 150 μm. The first experiment demonstrated optical magnetic imaging of living magnetotactic bacteria [150]. Several notable methodological advancements significantly improved the imaging speed and field-of-view [97]. Among those efforts are the speed-up of magnetic image recording via CMOS camera, creation of isotopically purified diamond substrates for narrower spectral line width, and correction of magnetic bias field inhomogeneity using $|0\rangle \leftrightarrow |\pm 1\rangle$ transitions.

These upgrades have opened a broader utility of the quantum diamond microscope. In biology, it provides co-registered optical and magnetic images of cells labeled with magnetic nanoparticles [97], which can address many problems associated with the homeostasis of magnetic nanoparticles by various types of cells under different conditions. In geology, the diamond quantum microscope offers a valuable approach to imaging the magnetization of meteorites and earth rocks with unprecedented spatial resolution, enabling the detailed study of the solar system and earth history [90].

6.1.2 Single-pixel magnetic sensing

To improve the sensitivity even further, one may integrate magnetic signal over larger field-of-view by use of a single-pixel detector instead of CCD or CMOS cameras. This ultrahigh-sensitivity, low-spatial-resolution system also allows the detailed study of (i) intra-diamond paramagnetic impurities using various sensing protocols (e.g. spectral decomposition [21] and correlation spectroscopy [141, 148]) as well as (ii) external magnetic samples, such as magnetic fields produced by neuron firing (J. Barry *et al.*

in preparation) and magnetic fluctuations from statistically polarized nuclear spins. For these demonstrations, introducing the imaging capability can also add more useful information. However, it is sometimes difficult to map fluorescence directly from NV centers to a camera in free space because of the geometrical complexity of the setup. In that situation, k-space readout via phase encoding can be a solution.

6.1.3 Temperature, electric field, and pressure sensing

The NV center is also a high-sensitivity probe for electric field [68], temperature [55, 145, 258], acceleration [8], and pressure sensor [42]. Temperature change causes a shift in the zero-field splitting with a coefficient of $dD/dT = -74$ kHz K^{-1} [5]. Electric fields behave like a strain, which also causes a shift in the zero-field splitting [67, 222]. By use of a "pressure-to-field converter" (e.g. magnetostrictive materials and soft conductive wires), one can also indirectly detect pressure and stress using NV centers [42].

6.2 Magnetic Field Gradient

In Chapter 4, magnetic field gradient was the key technique for phase-encoding the information about the location and local magnetic field to the spin state [14]. Thus, it is of natural interest to investigate the limit of the maximum achievable magnetic field gradient and its other utilities.

6.2.1 Limits on magnetic field gradient

The prototype of Fourier magnetic microscope produced a magnetic field gradient of 1 G $\mu\mathrm{m}^{-1}$. This gradient strength was enough to demonstrate the superresolution imaging of NV centers and local magnetic field profile. Two general approaches to-

ward stronger gradients are (i) to directly fabricate a microcoil on the NV-containing diamond and (ii) to reduce the coil separation. Using these approaches, we have achieved a gradient strength of greater than 0.1 G nm^{-1} over 1.2×8 μm^2 area (K. Arai *et al.* in preparation). Furthermore, the produced magnetic field gradient can be modulated at ~ 1 MHz. Gradients of comparable magnitudes over such large area and with high switching rates are difficult to achieve using ferromagnets [61, 170, 225]. An additional 10-fold improvement in gradient strength would be possible by increasing the electric current through the microcoil, matching the electric circuit impedance, and introducing an active temperature control system [72, 152]. This large gradient opens a new application – selective control of NV spins via frequency encoding.

6.2.2 Selective control of NV centers via frequency-encoding

Frequency encoding finds applications in MRI for slice sectioning with a millimeter-scale resolution [98] and has been recently employed in trapped-ion experiments to control coherently ions separated by a few microns [268]. In frequency encoding, magnetic-field gradients map the positions of NV spins at different locations in a diamond sample onto their Larmor precession frequency. The spins are then selectively driven by microwaves whose carrier frequencies match the resonance frequencies of the sites of interest.

One important prerequisite toward quantum computation is single-site addressability of NV centers prepared in large arrays with fast switching rate [214, 259, 278]. Previous experimental work on nanoscale NV-spin manipulation, however, has either involved only an isolated pair of NV sites [68, 188] or has required slow scanning of the probe across different NV sites [101, 174]. Frequency encoding with strong pulsed field gradients allows site-selective controlling of proximal NV centers with high fidelity and large spatial dynamic-range. In particular, a gradient field of > 1.0

G nm^{-1} would allow selective addressing of an array of dipolar-coupled NV centers spaced by ≈ 10 nm with $> 95\%$ fidelity.

6.2.3 Other applications

The flexibility of microcoil design facilitates integration into other systems, such as microfluidics and micro-electro-mechanical systems (MEMS). Also, the selective driving technique is compatible with other NMR pulse sequences involving NV centers and dark spins [102, 245] for magnetic field sensing. These advantages may open new directions of applications. Examples include the realization of quantum simulators for exotic quantum and topological phases [43, 131, 224], imaging of nanoscale nuclear spin diffusion and effusion in the cellular or microfluidic environment via q-space detection [45], and non-local probing of strongly correlated spins via k-space readout.

6.3 Geometric Control

Geometric manipulation also has a potential for other quantum technologies. This section overviews the history of extending Berry phase to the non-adiabatic and non-Abelian cases and introduces some recent attempts to use geometric manipulation for topological phase transition and holonomic quantum gates.

6.3.1 Non-adiabatic, non-Abelian geometric phase

In 1984, Berry showed that a system acquires a measurable phase shift when the system adiabatically travels a closed path in the parameter space [29]. In the same year, Wilczek and Zee [271] extended the concept of Berry phase to degenerate states and obtained non-Abelian geometric phase. In 1987, Aharanov and Anandan [6] proved that the adiabatic condition was not necessary. Samuel and Bhandari [227]

introduced further extensions to noncyclic and nonunitary cases. In 1988, Anandan [11] derived the non-Abelian geometric phase in a non-adiabatic process.

6.3.2 Topological quantum simulation

Topology [269] provides a theoretical basis for numerous physical phenomena exhibited in gapped quantum states, such as spin liquid [270], quantum Hall [253], and topological insulators [133]. The transition of topological phases has been of particular interest in condensed matter research [27, 167]. However, it is usually challenging to change the topological phases from one to another because topological states are robust against local perturbations. Recently, quantum simulation of topological phase transition using atomic systems has attracted attention because it is easy to evoke a topological transition using such systems via geometric manipulation [103]. For example, quantum simulation of Haldane model has been realized with ultracold atoms [130] and superconducting qubits [224]. The NV center is also potentially a good candidate for these applications (J. Lee *et al.* in preparation).

6.3.3 Holonomic quantum computation

The concept of holonomic quantum computation is to use the holonomy associated with an underlying fiber bundle structure of a quantum system [74, 281]. As opposed to dynamic phase gates, which are vulnerable to various imperfections and decoherences, geometric phase gates are considered to be robust against errors [127, 129]. Among many ideas, recently experimentally demonstrated is non-adiabatic, non-Abelian holonomic gates using three level solid-state qubit systems [1, 233, 283]. The next step toward scalable holonomic quantum computation would be to build an array of holonomic gates which are individually addressable. The frequency and phase encoding might provide one practical approach to this goal.

Appendix A

Spin 1/2 System and Bloch Sphere Representation

A.1 Brief History of Spin

The story of spin dates back in the 1920s [257]. Shortly after Bohr published the theory of hydrogen atom spectrum [34], physicists realized that three quantum numbers in his theory were not enough to explain the multiplet structures of alkali and alkaline-earth atoms. Sommerfeld, Landé, and Pauli were aware that the fourth quantum number was necessary. In 1923, they constructed a model based on an interaction between the electron and core, from which the multiplet structure arose qualitatively. However, their theory failed to give the correct interval between the doublet lines in alkali atoms. Discovered during these efforts was the Landé g-factor, which is one of the most precisely measured physical quantities to date [111]. Pauli, who had been looking for a theory that didn't need to rely on a model, then speculated that the origin of multiplet was not the core but the electron itself. In 1925, Kronig, Goudsmit, and Uhlenbeck proposed a spinning electron model to explain the fourth quantum

number with a classical picture [261]. Their idea immediately caused a controversy as the speed of rotation at the electron surface should exceed the speed of light. Moreover, the value of energy splitting calculated with this model was off by a factor of two, which was later resolved by Thomas by introducing a correct rotational frame (Thomas precession [252]).

Interestingly, the long debate about the fourth quantum number ended up in perhaps the strangest scenario. In 1927, Pauli concluded that the origin of spin was neither the core nor the spinning electron, but was simply indescribable by a classical picture [198]. Only a year later, Dirac derived the famous Dirac equation [65], which elegantly answered at least two questions: why the electron spin was half and how Thomas' theory could be quantized. The spinor formalism developed by Pauli and Dirac during this period may exemplify the peculiarity of quantum physics. In classical physics, vectors are defined as the set of physical quantities which transform in the same way as coordinates under rotation. Tensors are just an extension of this formalism [15]. This transformation leaves the equation of motion invariant. However, in quantum mechanics, vectors and tensors seem to be too inconvenient to express all the features of spinors. For the Schrödinger equation to be invariant, the spinor should transform with a unitary matrix. Surprisingly, the spinor does not come back to its original state after 2π rotations in this formalism. Around the time when Dirac and Pauli discovered electron spin, three molecular physicists, Hund, Hori, and Dennison, also discovered proton spin by studying the specific heat of the hydrogen molecule [62]. This strange new degree of freedom turned out to be a universal property of quantum particles.

Even today, the origin of spin remains a mystery. Nevertheless, the concept of spin degree of freedom has become the important foundation of various fields in modern physics and technology. In particle and nuclear physics, the mathematical description of spin is extended to a new quantum number, isospin , which classifies mesons

and baryons under strong interaction [276]. In optical and atomic physics, the narrow hyperfine transitions originating from spin-orbit coupling provide the precious resource for high precision measurements of space-time [80, 247], fundamental symmetries [10, 122, 206], and physical constants [37]. In condensed matter and statistical physics, the spin-spin interaction beautifully explains the origin of ferromagnetism[1], which is nowadays the main workhorse for a hard disk drive in computers [18, 32, 84]. In chemistry and medicine, nuclear magnetic resonance [213] provides the key principle for the medical imaging of the human body and the spectroscopic determination of chemical structure and dynamics in various materials [93, 144]. Spin-based processes also appear in various other diagnostic tools including magneto-optic Kerr effect [134], neutron scattering [232], and magnetic circular dichroism [39]. Recently, physicists have been investigating new directions of quantum applications (for example, quantum sensing [17, 35, 41, 225, 274], metrology [96, 136, 273], and computation [85, 132, 137, 162]). Indispensable for these applications is advanced spin manipulation in many aspects as discussed in the next section. Thus, it is an important subject to develop new schemes that push limits on precision in controlling spins.

A.2 Manipulation of Spins via Magnetic Resonance

A two-level spin-1/2 system, the simplest example, lives in the two dimensional Hilbert space. Two degrees of freedom are sufficient for constructing an arbitrary quantum state from the basis states $\{|0\rangle, |1\rangle\}$,

$$|\psi\rangle = \cos\frac{\alpha}{2}|0\rangle + e^{i\beta}\sin\frac{\alpha}{2}|1\rangle, \tag{A.1}$$

[1]Einstein and de Haas had already revealed experimentally that the origin of magnetism was the electron spin in 1915.

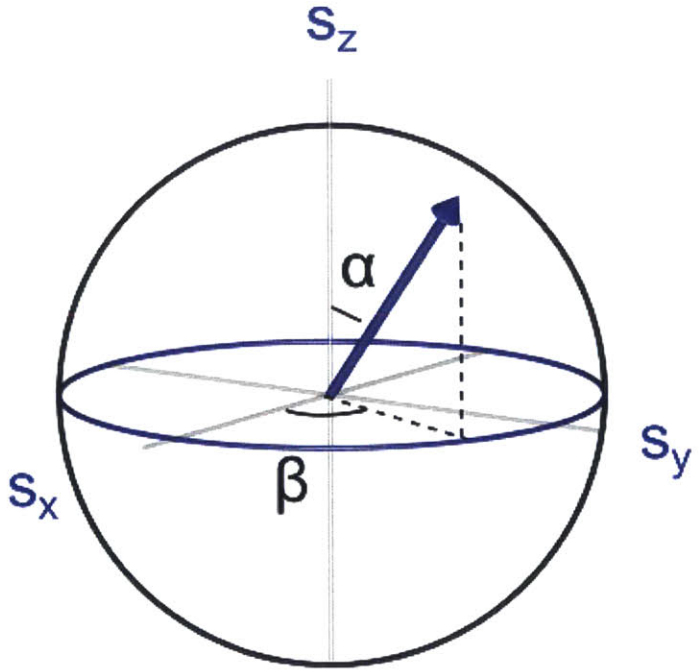

Figure A-1: Bloch sphere.

where $0 \leq \alpha \leq \pi$ and $0 \leq \beta < 2\pi$. In the Bloch sphere representation (A-1) [86], α and β define the polar and azimuthal angle on the surface of a unit sphere, and then the quantum state corresponds to a unit vector (Bloch vector) pointing from the origin to the surface

$$\boldsymbol{s} = (s_x, s_y, s_z) = (\sin\alpha\cos\beta, \sin\alpha\sin\beta, \cos\alpha). \tag{A.2}$$

In this vector form, the two-level system belongs to the three-dimensional orthogonal group O(3). Evolution of the quantum state is described by SU(2) rotations spanned by the Pauli matrices $\boldsymbol{\sigma} = (\sigma_x, \sigma_y, \sigma_z)$,

$$\sigma_x = \begin{pmatrix} 0 & 1 \\ 1 & 0 \end{pmatrix}, \quad \sigma_y = \begin{pmatrix} 0 & -i \\ i & 0 \end{pmatrix}, \quad \sigma_z = \begin{pmatrix} 1 & 0 \\ 0 & -1 \end{pmatrix}. \tag{A.3}$$

A general rotation[2] about the axis $\hat{n}$ by angle ϕ is

$$U_{\hat{n}}(\phi) = \exp\left(-i\phi\hat{n}\cdot\frac{\boldsymbol{\sigma}}{2}\right). \tag{A.4}$$

Two key ingredients for precise control of the spin 1/2 system are the static and oscillating fields. Let Ω be the Rabi frequency of the oscillating field perpendicular to the quantization axis, ρ the oscillation phase, and Δ the frequency detuning. Using a rotating wave approximation, the interaction Hamiltonian in the rotating frame is

[2]The state can also be represented in a matrix form as

$$\mathcal{M} = \boldsymbol{s}\cdot\boldsymbol{\sigma} = \begin{pmatrix} \cos\alpha & e^{-i\beta}\sin\alpha \\ e^{i\beta}\sin\alpha & -\cos\alpha \end{pmatrix}.$$

In this case, the state rotation is given by

$$\mathcal{M}' = U_{\hat{n}}^{\dagger}\mathcal{M}U_{\hat{n}}.$$

written as

$$H(t) = \frac{\hbar}{2}\boldsymbol{R}(t) \cdot \boldsymbol{\sigma}, \tag{A.5}$$

where

$$\boldsymbol{R}(t) = (\Omega \cos\rho, \Omega \sin\rho, \Delta) \tag{A.6}$$

is a Larmor vector constructed from the fields. Then the Schrödinger equation

$$i\partial_t|\psi(t)\rangle = H(t)|\psi(t)\rangle \tag{A.7}$$

governs the time evolution of the states under the Hamiltonian. Equivalently, a unitary operator obtained by integrating both sides of Eq.(A.7)

$$U_{\hat{R}}(t_i, t_f) = \hat{T}\exp\left(-i\int_{t_i}^{t_f} \boldsymbol{R}(t) \cdot \frac{\boldsymbol{\sigma}}{2}dt\right) \tag{A.8}$$

describes the state evolution $|\psi(t_f)\rangle = U_{\hat{R}}(t_i, t_f)|\psi(t_i)\rangle$. Here the time-ordering operator $\hat{T}$ is introduced to symbolically account for the non-commutativity of Pauli matrices. As an alternative perspective, the evolution of state can be made more explicit by deriving the differential equation for $\boldsymbol{s}$ from Eq. (A.7) and (A.2)

$$\frac{d}{dt}\boldsymbol{s}(t) = \boldsymbol{R}(t) \times \boldsymbol{s}(t). \tag{A.9}$$

Thus, the Bloch vector precesses around the rotation axis $\hat{R} \equiv \boldsymbol{R}/|\boldsymbol{R}|$ at a speed of $|\boldsymbol{R}|$.

Appendix B

Additional Details for Wide-Field Magnetic Imaging

B.1 Bacterial Viability Assay Calibration and Implementation

Assessments of bacterial viability after magnetic and bright-field imaging were carried out using a standard commercial kit (Molecular Probes, BacLight Kit, L7007). The assay uses competitive binding of two fluorescent nucleic acid stains (green-fluorescent SYTO 9 and red-fluorescent propidium iodide) at concentrations such that cells with intact membranes (alive) show predominantly green fluorescence, while those with damaged membranes (dead) show less green and more red fluorescence. In order to assess the expected relative fluorescence rates for the two stains in AMB-1 cells in our setup (including all emission filters for each of the two stains, and their relative excitation efficiencies at 470 nm), we initially performed a series of calibration measurements on samples in which either the majority of cells were known to be alive or all were dead. In each case, cells were applied to the diamond surface after it was

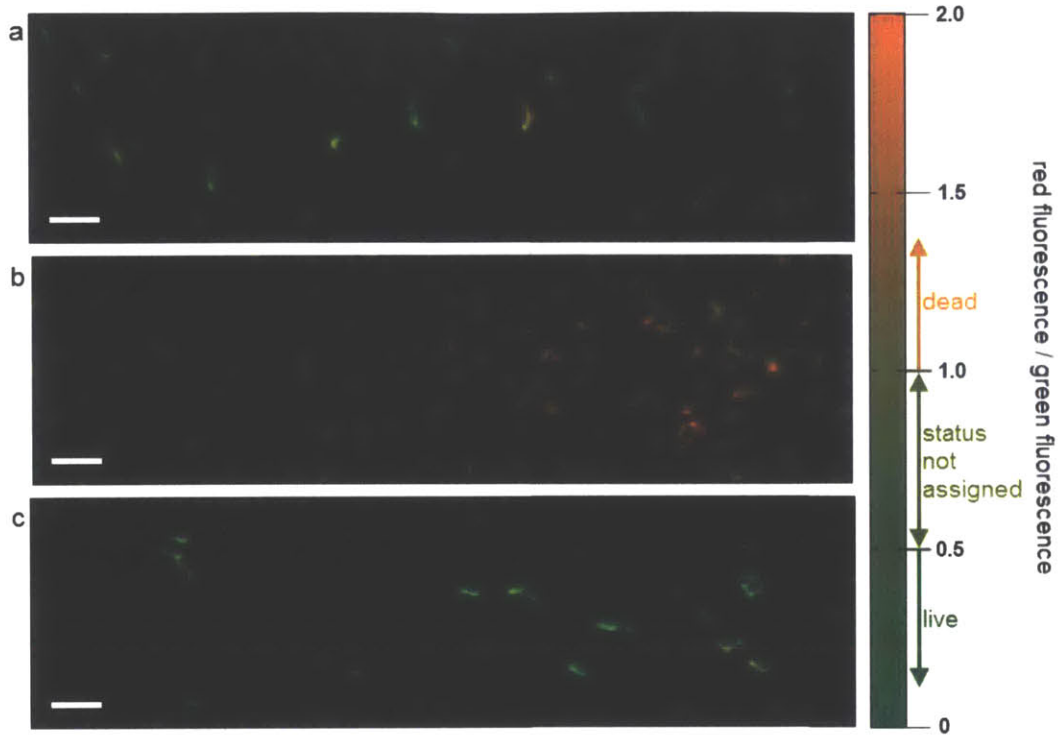

Figure B-1: Typical fluorescence data used to determine the viability of stained AMB-1 bacteria, for **a** bacteria taken directly from the culture, **b** bacteria that have been intentionally killed, and **c** the same bacteria as in Fig. 3-2a-b after performing magnetic field measurements. In each case, before measuring the fluorescence, the bacteria were incubated for 15 minutes in a mixture of stains from the BacLight bacterial viability kit (5 μM of green-fluorescent SYTO 9 and 30 μM of red-fluorescent propidium iodide). Red and green fluorescence images were recorded separately, and are shown above as overlapped images in the red and green channels respectively. A quantitative analysis of fluorescence data from many fields of view like those in **a** and **b** suggests that dead bacteria typically exhibit a red-to-green fluorescence ratio > 1, whereas a ratio < 0.5 indicates that a bacterium is very likely to be alive (see Fig. B-2). The viability of cells with intermediate fluorescence ratios is somewhat ambiguous, and these were consequently not assigned to either category. Most bacteria **a** taken directly from culture and **c** post-magnetometry appear to be alive or intermediate, although a small fraction of the bacteria in either case exhibit strong red fluorescence consistent with the dead bacteria in **b**. Note that in addition to the bacteria present in Fig. 3-2a-b, **c** also shows several bacteria that settled onto the diamond surface during the 15 minute incubation period. Scalebars are 5 μm.

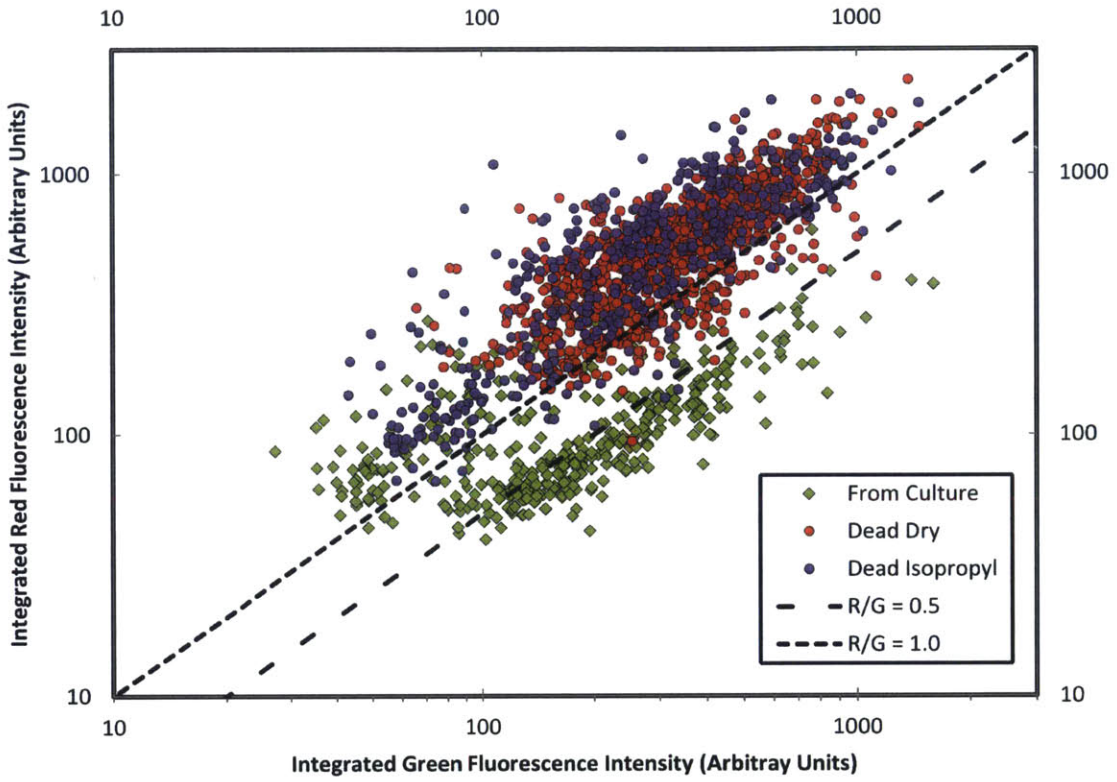

Figure B-2: Calibration data for BacLight staining of living and dead samples of *Magnetospirillum magneticum* AMB-1. The viable and non-viable populations divide into clusters identifiable by the ratio of integrated fluorescence in the red channel (vertical axis, R) to that in the green channel (horizontal axis, G). On the basis of these data, we assign cells with fluorescence ratio $R/G < 0.5$ to be alive, and those with $R/G > 1.0$ to be dead. The region of the plot with $0.5 < R/G < 1.0$ contains tails from both living and dead distributions in the calibration, and hence cells with fluorescence ratios in this range were left unassigned in the assays conducted after magnetic imaging experiments.

cleaned and prepared with a drop ($\sim$ 5 μL) of 0.01% poly-L-lysine (Sigma-Aldritch, P4707, mol. wt. 70-150 kDa), which was then allowed to dry. Samples containing live cells were taken from cultures of AMB-1 grown as described in Section 3.7. A 50 μL volume of bacterial solution was pipetted into the bath chamber containing the diamond and topped up with approximately 150 μL of phosphate buffered saline (PBS). The cells were left for 15 minutes to settle onto the diamond surface, and the assay was performed. Dead cell samples were prepared in one of two ways: In the first method (i) a drop ($\sim$ 5 μL) of bacterial solution was placed directly on the PLL-coated diamond surface and allowed to dry completely. Approximately 15 minutes after drying, the bath chamber was filled with 200 μL of PBS and the assay was performed. Alternatively (ii), a 50 μL volume of cells was added to the bath with 150 μL of PBS and allowed to settle for 15 minutes as for the live calibration samples. Once the cells had adhered to the PLL layer on the diamond surface, 50 μL of the bath was removed and replaced with an equal volume of isopropyl alcohol. The cells were incubated in the isopropyl solution for 30 minutes, after which the solution was gently removed and replaced with 200 μL of PBS, and the assay was performed.

Carrying out the assay consisted of adding the stains in appropriate concentrations (5 μM SYTO 9 and 30 μM propidium iodide), and incubating for 15 minutes in the dark. Fluorescence imaging was then performed using 470 nm excitation light from an LED (Thorlabs, M470L2), with appropriate emission filters to completely separate the green (Thorlabs FELH0500 and Thorlabs FES0550) and red (Chroma HQ640/120) channels. The image was carefully re-focused in each channel to account for chromatic aberration in the objective (Olympus UIS2 LumFLM 60xW / 1.1 NA), and exposure times were kept equal. Typical green and red fluorescence images are shown in Fig. B-1. (The image shown in Fig. B-1c corresponds to the sample and field of view depicted in Fig. 3-2a-b.) Fluorescence images were analyzed using home-made software written in MATLAB, in the following steps: (i) Gaussian filtering to remove high frequency

pixel noise; (ii) rolling-ball background subtraction; (iii) co-registration of the two images by maximizing their crosscorrelation; (iv) determination of bacteria positions by finding all local maxima above some threshold (usually > 10 standard deviations above background); (v) assignment of correspondence between identified bacteria in the two images according to minimum distance, with some checking to eliminate ambiguous pairings and duplicates; and (vi) integration of the fluorescence signal around each peak in a 3-pixel radius, which is approximately proportional to the average fluorescence intensity over the whole bacterium.

This procedure was carried out for several fields of view such that about ~ 500 individual bacteria were analyzed for each calibration sample (Fig. B-2). As expected, almost all cells in the two dead samples showed a relatively high ratio of red to green fluorescence. In the living sample, the majority of cells showed a comparatively low ratio of red to green fluorescence, although a distinct sub-population of these cells had a high fluorescence ratio comparable to that of the dead cells, likely indicating a non-viable cell fraction in the original bacterial solution. According to these calibration data, we defined a red to green fluorescence threshold $R/G < 0.5$ to correspond to viable cells in our setup. From our measurements we estimate that the probability for a cell with measured $R/G < 0.5$ to be alive is approximately 99.4%. Cells with $R/G > 1$ are clearly non-viable, while cells with $0.5 < R/G < 1.0$ are ambiguous and are not assigned to either population. (We note that cells in this intermediate range appear green to the eye in Fig. B-1. However, because the estimated probability from this calibration for a MTB with $R/G < 1$ to be alive is only $\sim 90\%$, we have conservatively chosen to leave cells with $0.5 < R/G < 1.0$ unassigned in order to avoid any significant probability of mischaracterization.) These thresholds were highly repeatable in calibration measurements performed on our setup over the course of several months, even when carried out with different AMB-1 cultures and different batches of the BacLight nucleic acid stains.

Appendix C

Additional Details for Fourier Magnetic Imaging

C.1 Fourier Magnetic Microscope

The Fourier magnetic microscope consists of a home-built scanning confocal microscope and a diamond coverslip on which gradient microcoils were photolithographically defined. Optical excitation for the confocal microscope is provided by a 400 mW diode-pumped solid state laser (Changchun New Industries) operating at 532 nm. An 80 MHz acousto-optic modulator (Isomet Corporation) controls laser pulses for spin initialization and read-out. A single-mode fiber is used to clean up the mode profile of the laser and the output of the fiber is sent to a 100x oil-immersion objective with a numerical aperture of 1.3 (Nikon CFI Plan Fluor). The NV-containing diamond sample is mounted on a three-axis motorized stage (Micos GmbH) that allows scanning of the sample in the focal plane of the objective. Fluorescence from NV centers is separated from the 532 nm excitation light with a dichroic beamsplitter (Semrock LM01-552-25). After filtering through a long-pass filter (Semrock

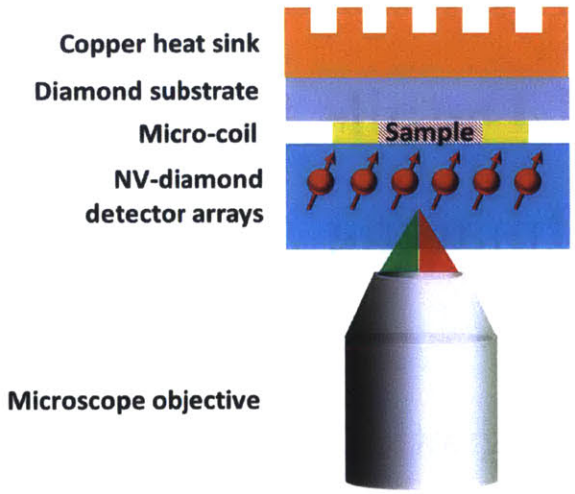

Figure C-1: Schematic of Fourier magnetic imaging microscope. The gradient microcoil is placed close to a shallow NV layer ($\sim$ 20 nm from the diamond surface) and UV-curing optical adhesive is applied between the microcoil and the NV-diamond chip to form physical and thermal contact. A sample to be magnetically imaged could be inserted between the NV-diamond surface and microcoil. A poly-crystalline diamond chip is used as the microcoil fabrication substrate for optimum heat dissipation. Furthermore, the diamond substrate is thermally attached to a copper heat sink under the condition of extra air flow.

LP02-633RS-25), the fluorescence is focused into a single-mode fiber with a mode-field-diameter $\sim$ 5 μm (which acts as the pinhole of the confocal microscope) and sent to a single-photon counting module (Perkin Elmer SPCM-ARQH-12). Pulses from the detector are read using the counter input of a DAQ card connected to a computer. Microwave excitation is provided by a signal generator (Agilent E4428C) whose output is amplified (Mini-circuits ZHL-16W-43-S+) and sent though a microwave loop defined on the diamond coverslip. Fabrication of the photo-lithographic patterns on the diamond coverslip is described in Section 4.7. Gradient pulses are defined using the arbitrary waveform function of a programmable signal generator (Stanford Research Systems SRS345) and amplified by an audio-frequency amplifier (Texas Instruments LM4780). The bandwidth of the gradient pulses is limited by the slew rate of the amplifier to approximately 1 MHz.

C.2 Thermal Effects of Gradient Microcoil Operation

Figure C-1 shows how the gradient microcoil is integrated into the Fourier magnetic imaging microscope. UV-curing optical adhesives are used to glue the NV-diamond detector to the gradient microcoil. As specified in Section 4.7, the microcoil is fabricated on the front surface of a poly-crystalline diamond substrate for optimum heat dissipation. The back surface of this diamond substrate is attached to a copper heat sink cooled by an air fan to further remove heat. The resistance of each gradient microcoil is 1.4 Ω, such that 1.4 W of heat is generated at a typical peak current of 1 A. To assess thermal performance under standard operating conditions, the system was modeled using COMSOL Multiphysics software. With a heat sink and fan cooling we estimate a steady-state temperature rise of the diamond sample of $<$ 10 K at 1 A

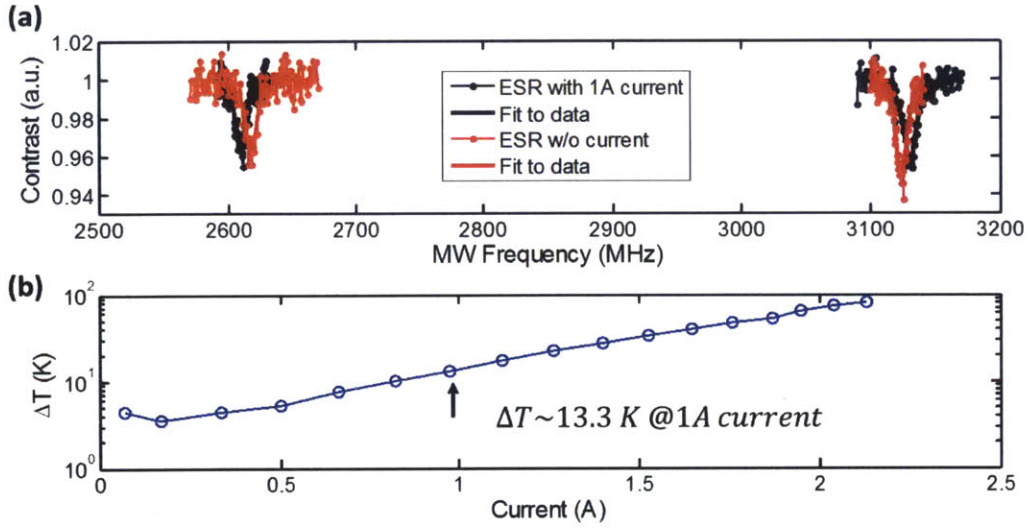

Figure C-2: Measurements of the NV-diamond sensor's temperature change due to steady current through the gradient microcoil. **a**, NV ESR spectral line shifts for 1 A current. The NV axial zero-field splitting parameter D varies with temperature T. By measuring the shift in D (midway between the $|0\rangle$ to $|\pm 1\rangle$ ESR frequencies), magnetic-field-induced (Zeeman) ESR line shifts can be removed and the diamond temperature change can be estimated. **b**, Measurement of microcoil resistance change with increasing current. Here, the temperature coefficient of resistance for gold $\approx$ 0.0034 K^{-1} is used. When 1 A current is applied, the estimated temperature increase $\approx$ 13 K, consistent with the result from ESR measurements.

peak current. An analytical model based on techniques described in ref. [104] gave similar temperature estimates.

The rise in temperature was experimentally determined using two techniques. In the first technique, electron spin resonance (ESR) measurements were performed on NV centers within a nanopillar, both with and without a steady current of 1 A in the gradient microcoil (the maximum current used in Fourier imaging experiments). The magnetic field produced by the gradient microcoil induced a Zeeman shift of the ESR resonance line (in addition to that caused by the static magnetic field). A temperature change of the NV-diamond sample due to current in the gradient microcoil also caused a decrease in the zero-field splitting of 74.2 kHz per degree rise in temperature [5]. From the observed 1 MHz shift in the zero-field splitting when a steady current of 1 A was sent though the microcoils, the temperature shift was estimated to be $\approx$ 13 K (Fig. C-2a). In the second experimental technique, the change in resistance of the gold microcoil was measured as a function of current. From the known value of the temperature coefficient of resistance of gold, the temperature rise at 1 A current was again estimated to be $\approx$ 13 K (Fig. C-2b). Note that the steady-state temperature rise of the integrated experimental assembly (NV-diamond sensor chip, microcoil, etc.) during Fourier magnetic imaging is estimated to be $\approx$ 5 K due to the finite duty cycle of the gradient pulse sequence, as shown in Fig. 4-2, and the variable gradient strengths employed (mostly less than from the maximum 1 A current).

The above measurements were performed to characterize steady-state temperature rise during maximum activation of the gradient microcoils. To assess dynamic thermal effects during application of pulsed magnetic field gradients, the analytical formula listed in ref. [104] was applied to estimate the microcoil's thermal time constant:

$$\tau_{\text{fast}} = \frac{C_W h}{\kappa - h j^2 \alpha \rho}, \tag{C.1}$$

where C_W is the heat capacity (per volume) of the microcoil, κ is the thermal conductance, ρ is the microcoil's (cold) resistivity with a linearly approximated temperature coefficient α, h is the microcoil thickness, and j is the applied current density. For typical experimental conditions, this yields $\tau_{\text{fast}} \sim 0.25$ μs, which is an order of magnitude shorter than the gradient switching period (~ 1 μs). The microcoil's thermal behavior is thus determined to be close to quasi-static during the gradient switching process, with insignificant effect from thermal shock. In addition, during a complete Fourier imaging experiment there is slow heating (related to heat dissipation within the substrate and heat sink) that was measured to be on the order of seconds, which is much slower than the gradient "on time" for phase-encoding (~ 100 μs NV interrogation time). Thus the gradient strength is stable during each k-space measurement and the overall system temperature increase during data acquisition (5 K, as noted above) is stable to $\sim$ 1 K after the initial few-second transient. In all, the thermal performance of the system was found to be well understood, with insignificant corruption of the Fourier imaging results.

C.3 Gradient Calibration

As described in Chapter 3, NV signals for a point in k-space have the form $s(\boldsymbol{k}) \sim \cos(2\pi \boldsymbol{k} \cdot \boldsymbol{r}_0)$, where $\boldsymbol{k} = (2\pi)^{-1}\gamma\tau(dB_\zeta/dx, dB_\zeta/dy)$. Thus, the magnitude of k is proportional to the magnetic field gradient, which is in turn proportional to the current I, and this current is proportional to the voltage V applied by the SRS345 programmable signal generator. The overall proportionality constant, which maps V to k, was estimated using the procedure described below.

A low-resolution one-dimensional phase encoding sequence was run sequentially on a set of 7 nanopillars along the x (and separately y) direction. The NV signal was measured as a function of SRS345 voltage V. The signal for each nanopillar

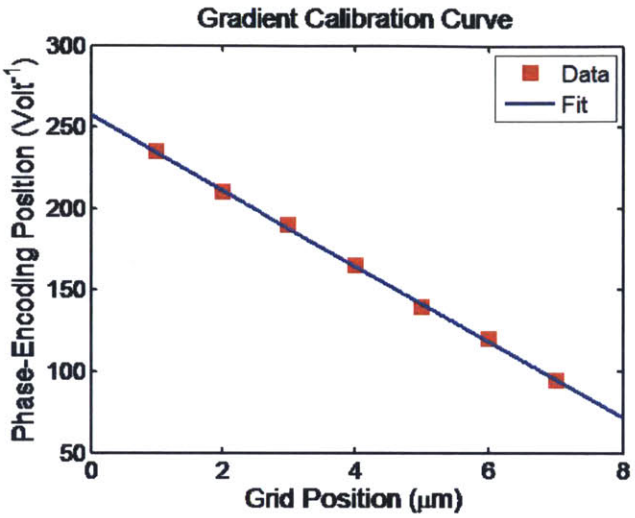

Figure C-3: 1D low resolution phase encoding measurements for the y micocoil gradient calibration. The slope of the blue line is -23 Volt$^{-1}\mu$m^{-1}. The SRS345 voltage is divided by this value to obtain k-space data in μm^{-1} units.

was then Fourier transformed to obtain a peak in "inverse voltage" space. The peak positions (in units of Volt^{-1}) were then plotted as a function of nanopillar positions. The inter-pillar spacing of 1 μm, known from the defined lithographic pattern (see Section 4.7.1), allowed conversion between Volt^{-1} units and distance units in microns. This calibration procedure made accurate determination of local gradients possible and also properly accounted for any misalignment between the diamond coverslip patterned with microcoils and the NV-containing diamond sample. Calibration data for the y micocoils is shown in Fig. C-3. Similar results were obtained for the x coils. In the previous section, systematic effects due to heating are discussed. Another potential source of systematic error in the gradient calibration is the variation of NV center positions in the nanopillars. If the NV centers are assumed to be randomly distributed in a nanopillar, then the root-mean-square deviation of NV position of a given crystallographic orientation, projected onto the x axis from the center of the nanopillar, is 140 nm, for the measured NV density in the sample. Since 7 nanopillars

are used for this gradient calibration, the total spacing between the leftmost and rightmost pillars is 6,000 nm. The estimated error of the magnetic field gradient field is thus 140 nm/6000 nm/$\sqrt{7}$ = 0.9 %. The factor of $\sqrt{7}$ is included because there are 7 data points (i.e., nanopillars) with uncorrelated variations in NV positions. The additional uncertainty introduced to the Fourier imaging resolution by this method of gradient calibration is 0.04 nm for 1D imaging and 0.3 nm for 2D imaging. To further reduce this uncertainty in future work, the gradient calibration could be extended to include additional rows of nanopillars.

C.4 Magnetic Field Estimates and Measured Values for Wide FOV Imaging

For the three example nanopillar magnetic images shown in Fig. 4-6, the AC magnetic field differences between NV center pairs, as determined from Fourier magnetic imaging, are $\Delta B_{J=1} = [6.5 \pm 1.1] \times 10^2$ nT, $\Delta B_{J=2} = [1.9 \pm 0.6] \times 10^2$ nT, and $\Delta B_{J=3} = [0.8 \pm 0.4] \times 10^2$ nT. A measure of the long-range magnetic field gradient is provided by the low-resolution real-space image:

$$\boldsymbol{\nabla} B(\boldsymbol{r}_J) = \left[\frac{B(x_{J+1}) - B(x_J)}{\Delta x}, \frac{B(y_{J+1}) - B(y_J)}{\Delta y} \right], \tag{C.2}$$

where $B(\boldsymbol{r}_J)$ is the spatially-averaged magnetic field magnitude at the J th nanopillar located at position $\boldsymbol{r}_J = [x_J, y_J]$, and $\Delta x, \Delta y = 1$ μm is the distance between adjacent nanopillars. The expected magnetic field difference between NV centers within the J th nanopillar is then given by:

$$\Delta B^{\text{exp}}(\boldsymbol{r}_J) = \nabla B(\boldsymbol{r}_J) \cdot (\boldsymbol{r}_l - \boldsymbol{r}_m), \tag{C.3}$$

where $\boldsymbol{r}_l, \boldsymbol{r}_m$ are the NV positions determined via Fourier imaging. For $J = 1$, for example, the local gradient is $(B(x_{J+1}) - B(x_J))/\Delta x = (32.2 - 29.7)\ \mu\text{T}/1\ \mu\text{m} = 2.5\ \mu\text{T}/\mu\text{m}$, $(B(y_{J+1}) - B(y_J))/\Delta y = (35.7 - 29.7)\ \mu\text{T}/1\ \mu\text{m} = 6.0\ \mu\text{T}/\mu\text{m}$, and the NV separation is $x_l - x_m = 90$ nm, $y_l - y_m = 60$ nm. The expected magnetic field differences between NVs in the three example nanopillars are thus: $\Delta B^{\text{exp}}_{J=1} = [5.9 \pm 1.4] \times 10^2$ nT, $\Delta B^{\text{exp}}_{J=2} = [2.0 \pm 1.1] \times 10^2$ nT, and $\Delta B^{\text{exp}}_{J=3} = [1.5 \pm 0.6] \times 10^2$ nT, which are in close agreement with the Fourier-measured values.

C.5 Noise Statistics and Thresholding

The noise in k-space signals was observed to be Gaussian in nature. Upon Fourier transformation, the noise in the real and imaginary parts of the real-space signal was also observed to be Gaussian, as shown in Fig. C-4. This is to be expected, as Fourier transformation is a linear operation and will not alter noise statistics. The noise in the absolute value of the real-space signal, however, was observed to follow a Rayleigh distribution (Fig. C-4c). This is well known in the theory of MRI (ref. [106]). The standard deviation of the Rayleigh distribution was computed and the real-space data was thresholded at 5 times this standard deviation to obtain the 2D images of NV centers shown in the main text. In the 2D imaging experiment in Fig. 4-4c , the total free precession time was $\tau = 30\ \mu$s. For each point in k-space, the sequence was repeated 30,000 times to improve the signal-to-noise ratio. The image was acquired for k_x and k_y values between -0.018 nm^{-1} and $+0.018$ nm^{-1} in 64×64 steps. The 2D imaging experiment was then repeated 21 times to further improve the signal-to-noise ratio, such that the total data acquisition time per k value was 25.2 seconds. Plotted in Fig. 4-4d is the amplitude of the Fourier-transformed signal (abs$[S(\boldsymbol{r})]$).

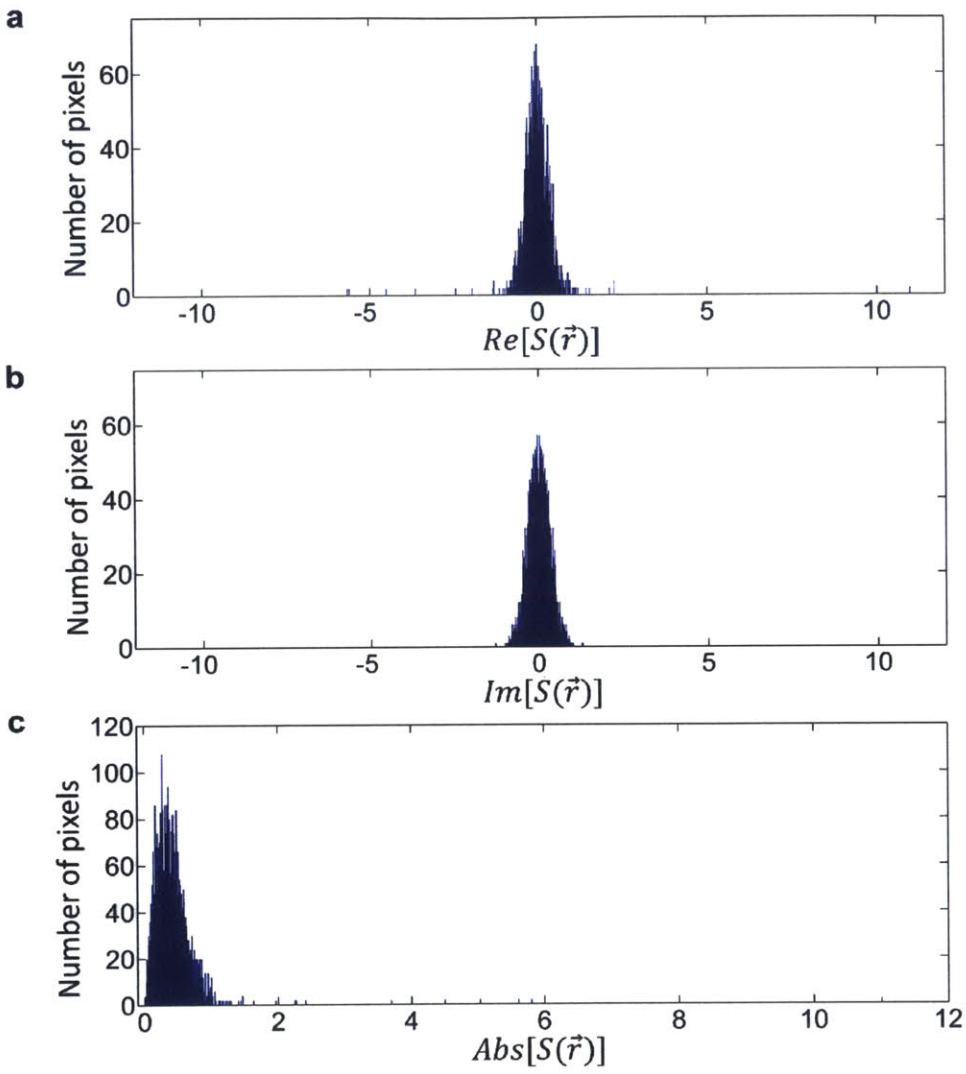

Figure C-4: Analysis of noise statistics. Fourier transform of k-space data from Fig. 4-4c. **a**, Histogram of the real part of the Fourier transformed real-space signal. **b**, Histogram of the imaginary part of the Fourier transformed real-space signal. The data of (**a**) and (**b**) exhibit Gaussian noise; and are fit to extract the standard deviation, σ of the noise. **c**, Histogram of the absolute value of the Fourier transformed real-space signal. The noise follows a Rayleigh distribution.

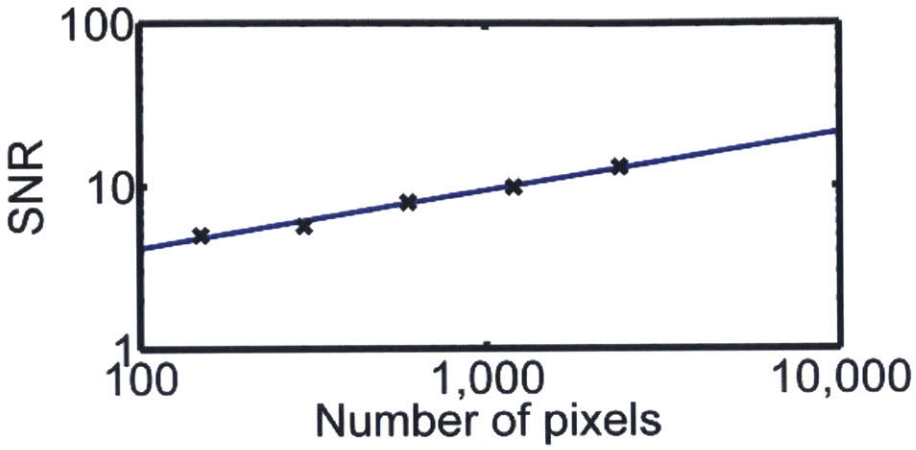

Figure C-5: Scaling of SNR with number of number of pixels. Fit to data (blue line) shows SNR scales as $N_{\text{pix}}^{0.36(0.8)}$ which is close to but smaller than the expected $N_{\text{pix}}^{1/2}$ scaling.

C.6 Multiplex Advantage

This section discusses the circumstances under which Fourier (k-space) imaging is faster than imaging based on point-by-point (real space) scanning. To make the discussion broad-based and not specific to NV centers, the following simplifying assumptions are made: (i) there are N_E ideal photon emitters that emit R photons per second, which are to be imaged using both point-by-point scanning and Fourier techniques; and (ii) each emitter is a two-level spin system with optical contrast $= 1$, i.e., all R photons are emitted by the spin-down state and zero photons by the spin-up state.

For the case of point-by-point scanning, if the imaging device scans over N_{pix} number of pixels spending time dt per pixel, then the total imaging time is $N_{\text{pix}}dt$ and the SNR is $\sqrt{Rdt}$. The data acquisition time, defined as $T_{\text{SNR}=1} = T/\text{SNR}^2$, where T is the total data acquisition time per k-value, is therefore given by $T_{\text{SNR}=1} = 1/R$.

In Fourier imaging, data is first acquired in k-space. Assuming the number of k-space points is N_{pix} and photons are counted for time dt per pixel, the total imaging

time is $N_{\text{pix}}dt$ and the SNR in k-space is $\sqrt{N_E R dt}$. To compute SNR in real space (i.e., after Fourier transformation), Parseval's theorem yields

$$(\text{Signal})_r = \frac{N_{\text{pix}}}{\sqrt{N_E}} \times (\text{Signal})_k \tag{C.4a}$$

$$(\text{Noise})_r = \sqrt{N_{\text{pix}}} \times (\text{Noise})_k \tag{C.4b}$$

which implies

$$(\text{SNR})_r = \sqrt{\frac{N_{\text{pix}}}{N_E}} \times (\text{SNR})_k. \tag{C.5}$$

Here the subscripts r and k represent real space and k-space respectively. The SNR for Fourier imaging is therefore equal to $\sqrt{N_{\text{pix}} R dt}$, which is higher than the SNR for point-by-point scanning by a factor $\sqrt{N_{\text{pix}}}$. Consequently, the total data acquisition time for Fourier imaging is

$$T_{\text{SNR}=1} = \frac{1}{R N_{\text{pix}}}, \tag{C.6}$$

which is less than that of point-by-point scanning by a factor N_{pix}. This improvement in SNR (or equivalently, multiplex speed-up in data acquisition time) is well known in FTIR spectroscopy, where it is referred to as the Fellgett advantage [82].

In Fig. C-5 data from Fig. 4-3 is used to show how SNR in real space scales with the number of pixels under our experimental conditions. The SNR is observed to increase with the number of pixels albeit with a slightly smaller exponent of 0.36(8) instead of 0.5. The distribution of the noise in the presence of phase encoding signal is Rician, which is a convolution between Gaussian and Rayleigh. For a signal-to-noise ratio (SNR) < 2, this noise is well approximated by a Rayleigh distribution. Thus, the measured SNR in this regime appears larger than that expected from a pure Gaussian. If this biasing effect, which could apply to the first two data points (where $N_{\text{pix}} \sim 128, 256$), is taken into account, the exponent may approach 0.5. It is also noted that the full multiplex enhancement in SNR may not always be realized

under realistic experimental conditions. For example, if the optical contrast is not perfect or if the point-spread-function of the signal peaks is wider than the imaging resolution, then the multiplex advantage will be diminished, though it may still be substantial. These issues will be addressed more in detail in future work.

C.7 Magnetic Field and Gradient Sensitivity

The magnetic field sensitivity and the field gradient sensitivity are calculated from the data presented in Fig. 4-5. In this measurement, information about NV center location and its local magnetic field is phase-encoded in 128 pixels, with a pulse sequence length of 20 μs for each data point in k-space. This Fourier magnetic imaging protocol is then repeated 3×10^5 times to improve the SNR. The total data acquisition time is therefore $T_{\text{tot}} = 768$ sec. The magnetic field sensitivity is given by

$$\eta = \frac{\sigma_B}{dS/dB}\sqrt{T_{\text{tot}}}, \tag{C.7}$$

where σ_B is the noise, and dS/dB is the slope of the magnetometry curve. From the low-resolution magnetic field measurement in Fig. 4-6, the current-to-field conversion is found to be $dB/dI = 0.0058$ T A^{-1}. From Fig. 4-5c, one can determine $\sigma_B = 0.11$, $dS/dI = 2\pi \times 2.3 \times 10^3$ A^{-1}. The magnetic field field sensitivity is therefore $\eta = 1.2 \times 10^3$ nT Hz$^{-1/2}$.

The gradient sensitivity between the two NV centers in Fig. 4-5 is calculated from the uncertainty of the field gradient, which is given by $G = \Delta B/\Delta x$, where $\Delta B = B(x_1) - B(x_2) = 650$ nT is the measured field difference between the two NV centers and $\Delta x = x_1 - x_2 = 121$ nm is the distance between them. Through error

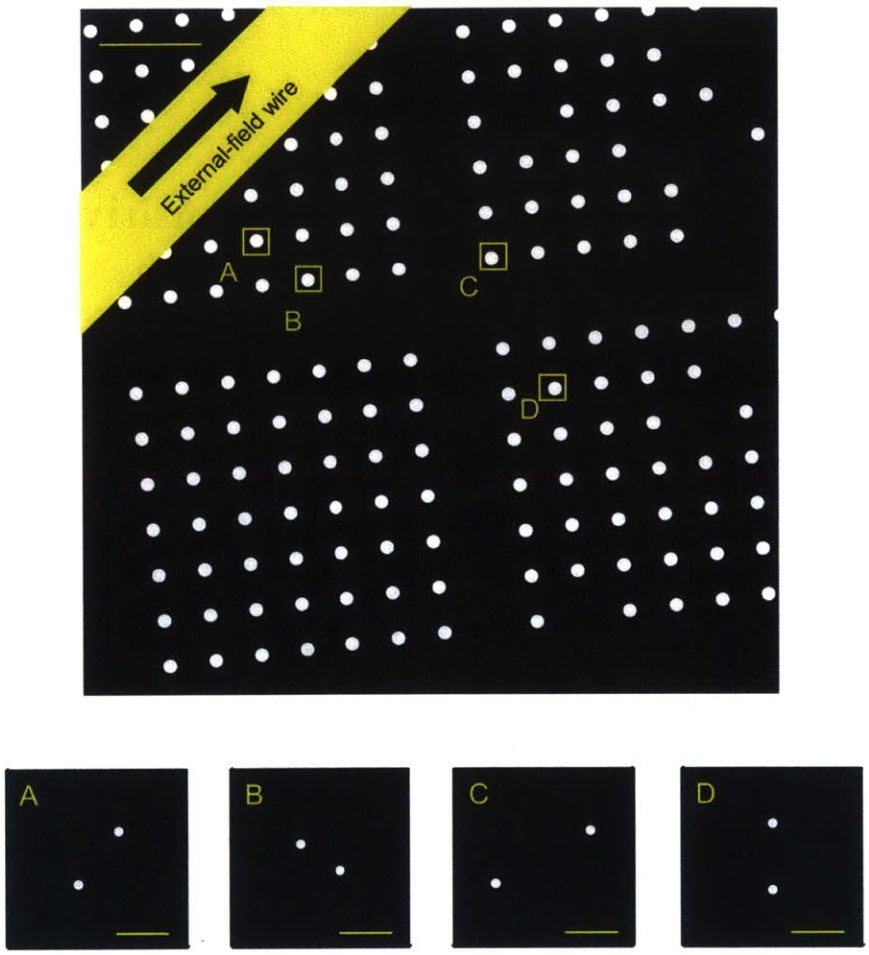

Figure C-6: Location of nanopillars relative to the external-field wire. Data for Figs. 4-4 and Fig. 4-5 were taken from nanopillar B. Data for Fig. 4-6 was taken from nanopillars B, C, and D. The compressed sensing data of Fig. 4-7 was taken from nanopillar A. Scale bars are 2 μm and 100 nm for top and bottom figures, respectively.

propagation the minimum detectable gradient is found to be

$$\delta G = G\left[\left(\frac{\delta\Delta B}{\Delta B}\right)^2 + \left(\frac{\delta\Delta x}{\Delta x}\right)^2\right]^{\frac{1}{2}}, \tag{C.8}$$

where $\delta\Delta B = \sqrt{2}\delta B = \sqrt{2} \times (1200 \text{ nT Hz}^{-1/2}/\sqrt{768} \text{ s}) = 61$ nT is the uncertainty in the magnetic field difference, and $\delta\Delta x = \sqrt{2}\delta x \sim \sqrt{2} \times (30 \text{ nm/SNR}/\sqrt{T_{\text{tot}}})$ is the uncertainty in the NV separation. Note that the dominant contribution comes from the first term, but that all errors are relatively small, justifying the error propagation analysis. The magnetic field gradient sensitivity is thus given by $\eta_G = \delta G\sqrt{T_{\text{tot}}} \approx (650$ nT/121 nm)(61 nT/650 nT)$\times\sqrt{768}$ s $= 14$ nT nm^{-1} Hz$^{-1/2}$.

C.8 Wide Applicability of Fourier Magnetic Imaging Technique

NV Fourier magnetic imaging, which employs phase-encoding of the detector NV spins rather than of the sample spins as in previous Fourier techniques, should be applicable to a broad range of systems that can be placed on or near the diamond surface. With the microcoil design and experimental conditions implemented in the present work, the maximum magnetic field difference generated by the gradients is ± 5 G across the largest field of view; and the gradient switching time is slower than 1 μs. Within these operating conditions, a wide range of nano-magnetic systems of interest will be unperturbed by such pulsed magnetic field gradients [119, 142, 135, 155, 185, 195, 264, 275]. See Table C.1 and Fig. C-7.

Table C.1: A survey of the minimum external magnetic field (H) required to perturb several condensed matter nano-magnetic phenomena of current research interest, as well as the characteristic timescales of these phenomena. In air, an H-field of 1 Oe corresponds to a B-field of 1 G. All of these systems would be unperturbed by the magnetic field gradients implemented with our NV-diamond Fourier magnetic imaging technique.

Physical phenomena of interests	Minimum magnetic field to perturb system, $H_{\min}$ (Oe)	Time scale	System (materials)	ref.
Magnetic vortex core reversal	15	4 ns	$Ni_{80}Fe_{20}$	[264]
	800	100 ps	$Ni_{81}Fe_{19}$	[119]
	~1000	static	$Ni_{80}Fe_{20}$	[195]
Ferromagnetic resonance	~ 1000	static	$Ni_{80}Fe_{20}$	[155]
Domain wall motion	~15	static	YIG	[275]
	~50	static	Co/Ni	[142]
	~500	~ 5 ns	$Ni_{80}Fe_{20}$	[135]
Skyrmion	~100	static	Cu_2OSeO_3	[185]
	~1000	static	FeGe	[185]

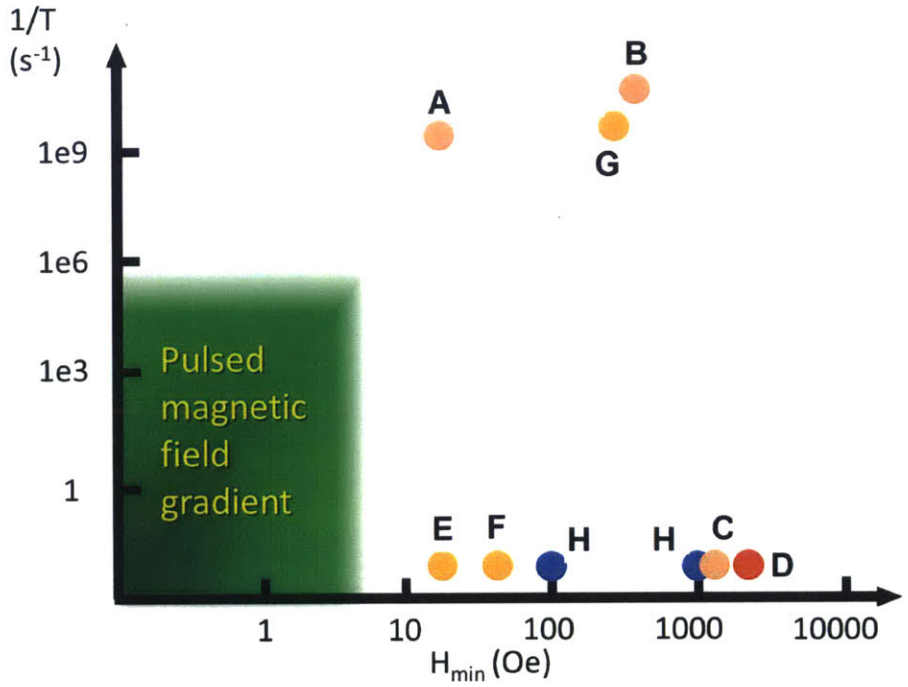

Figure C-7: Scatter plot of the magnetic field strengths and switching rates required to perturb several example condensed matter systems. Colored dots represent systems listed in the Table. Letters correspond to the referenced literature (A [264], B [119], C [195], D [155], E [275], F [142], G [135], H [185]). The green region indicates the working region of the pulsed magnetic field gradients implemented in our NV Fourier magnetic imaging demonstrations, which have a maximum magnetic field of ± 5 G and fastest switching rate of 1 MHz.

Appendix D

Additional Details for Geometric Phase Magnetometry

D.1 Geometric Phase Magnetometry Signal

The geometric phase magnetometry pulse is characterized by a time-varying Hamiltonian with three control parameters, Rabi frequency Ω, driving field phase ρ, and external field B:

$$H(t) = \frac{\hbar}{2}\boldsymbol{R}(t)\cdot\boldsymbol{\sigma}, \tag{D.1}$$

where $\boldsymbol{R}(t) = [\Omega\cos\rho(t), \Omega\sin\rho(t), \gamma B]$ is the Larmor vector and $\boldsymbol{\sigma} = [\sigma_x, \sigma_y, \sigma_z]$ the Pauli matrices. At time $t = t_i$, the system is prepared in a superposition of two levels: $|\psi(t_i)\rangle = \frac{1}{\sqrt{2}}(|+\rangle + |-\rangle)$. If the evolution of the Larmor vector is adiabatic, the instantaneous eigenstates depend on the Larmor vector

$$|+_{\boldsymbol{R}}\rangle = +\cos\frac{\theta}{2}|+\rangle + e^{+i\rho}\sin\frac{\theta}{2}|-\rangle \tag{D.2a}$$

$$|-_{\boldsymbol{R}}\rangle = -\sin\frac{\theta}{2}|+\rangle + e^{+i\rho}\cos\frac{\theta}{2}|-\rangle, \tag{D.2b}$$

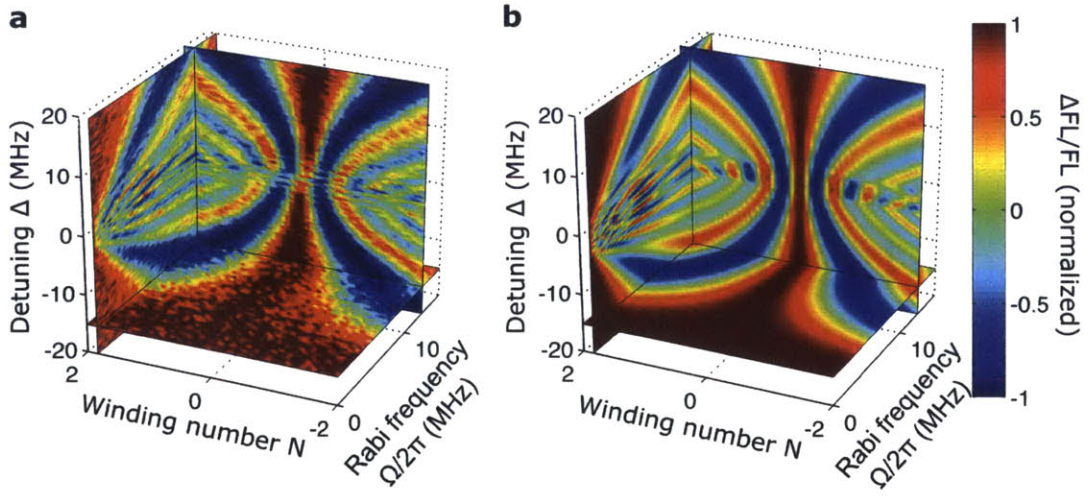

Figure D-1: Observation of geometric phase using a single electronic spin qubit in diamond. **a**, Measurement of the cosine of geometric phase as a function of Rabi frequency Ω, microwave frequency detuning Δ, and winding number N with a fixed interaction time of $T = 10$ μs. The amplitude of each hyperfine oscillations is extracted by fitting the 1D cross section data along Δ at $N = 2, \Omega/2\pi = 12$ MHz to the analytical expression of geometric phase signal with three hyperfine transitions. The measured signal is normalized to the mean of these three amplitudes. **b**, Analytical model of the cosine of geometric phase including three hyperfine transitions with the relative amplitudes determined in **a**. The measurement and analytical model agree well.

where θ is the polar angle between the z-axis and the Larmor vector $\boldsymbol{R}(t)$[1]. During the precession, the spin state vector rotates around the Larmor vector. Then, the spin acquires a dynamic phase ϕ_d, given by

$$\phi_d(t_i, t_f) = \int_{t_i}^{t_f} |\boldsymbol{R}(t')| dt' = R(t_f - t_i). \tag{D.3}$$

It is clear from this expression that the dynamic phase depends on the precession time. If this precession is cyclic, namely, $\boldsymbol{R}(t_f) = \boldsymbol{R}(t_i)$, the state will also acquire a geometric phase ϕ_g. To obtain the expression of geometric phase, we first calculate Berry connection:

$$\boldsymbol{A}^{\pm} = i\langle \pm_{\boldsymbol{R}} | \boldsymbol{\nabla}_{\boldsymbol{\lambda}} | \pm_{\boldsymbol{R}} \rangle = -\frac{1 \mp \cos\theta}{2r \sin\theta} \hat{\rho}, \tag{D.4}$$

where $\boldsymbol{\lambda} = (\theta, \rho)$ is the polar and azimuthal angels for the control parameters, and $\boldsymbol{\nabla}_{\boldsymbol{\lambda}} = r^{-1}\partial_\theta \hat{\theta} + (r\sin\theta)^{-1}\partial_\rho \hat{\rho}$ is the gradient Only the ρ component of the Berry connection is nonzero. Then, the geometric phase between two states is given by[2]

$$\phi_g^{\pm}(t_i, t_f) = \oint_c \boldsymbol{A}^{\pm} \cdot d\boldsymbol{\lambda} = -\pi N(1 \mp \cos\theta) = \mp \frac{N}{2}\Theta \qquad \text{mod } 2\pi. \tag{D.5}$$

The integration is performed along the closed path C with $\rho \in [0, 2\pi N]$, and $\Theta = 2\pi(1 - \cos\theta)$ represents the solid angle subtended by the path C.

In the geometric phase magnetometry sequence, we insert two Berry pulses between the spin echo pulses. Let us take the entire sequence length to be T. The microwave π rotation pulse about the x axis, $e^{-i\sigma_x \pi/2} = -i\sigma_x$, flips the $|\pm\rangle$ states,

---

[1]The instantaneous eigenstates are obtained by applying the SU(2) rotation operators to the original eigenstates

$$|\pm_{\boldsymbol{R}}\rangle = e^{-i\sigma_z \rho/2} e^{-i\sigma_y \theta/2} |\pm\rangle.$$

Under 2π rotations of ρ, however, these states will acquire a minus sign, which is strange because this azimuthal angle corresponds to the microwave phase. A gauge transformation $e^{i\rho/2}$ gives Eq. (A.2), which is single valued for ρ rotation.

[2]If the gauge transformation is not applied properly, the resulting geometric phase is off by π.

giving minus sign in front of the phase acquired during the second half of the interaction time

$$|\psi(T)\rangle = -\frac{i}{\sqrt{2}}\left(e^{-\frac{i}{2}\phi_{\rm tot}(0,T)}|+\rangle + e^{+\frac{i}{2}\phi_{\rm tot}(0,T)}|-\rangle\right), \tag{D.6}$$

where $\phi_{\rm tot}(0,T) = \phi_d(0,T/2) - \phi_d(T/2,T) + \phi_g(0,T/2) - \phi_g(T/2,T)$ is the total phase acquired during the sequence. The dynamic phase part cancels because $\phi_d(0,T/2) = \phi_d(T/2,T) = RT/2$. On the other side, the geometric phase part can be doubled by alternating the direction of precession between each pulse: $\phi_g(0,T/2) = -\phi_g(T/2,T) = N\Theta$. The final state is

$$|\psi(T)\rangle = -\frac{i}{\sqrt{2}}\left(e^{-iN\Theta}|+\rangle + e^{+iN\Theta}|-\rangle\right). \tag{D.7}$$

Finally, the final $\pi/2$-pulse maps the phase into a population difference:

$$P = \cos(2N\Theta). \tag{D.8}$$

In Fig. D-1, the geometric phase signal is measured in 3D parameter space.

D.2 2π phase ambiguity

The dynamic phase magnetometry signal and its derivative are expressed as

$$P_d(B) = \cos(\gamma BT) \tag{D.9a}$$

$$\frac{dP_d(B)}{dB} = \gamma T \sin(\gamma BT). \tag{D.9b}$$

For any measured signal P_d, there are infinite number of degenerate magnetic field values, which are related by $B_m = B + 2\pi m(\gamma T)^{-1}$, where $m = 0, \pm 1, \pm 2, \ldots$, is an integer. This degeneracy cannot be resolved by measuring the slope or adding a

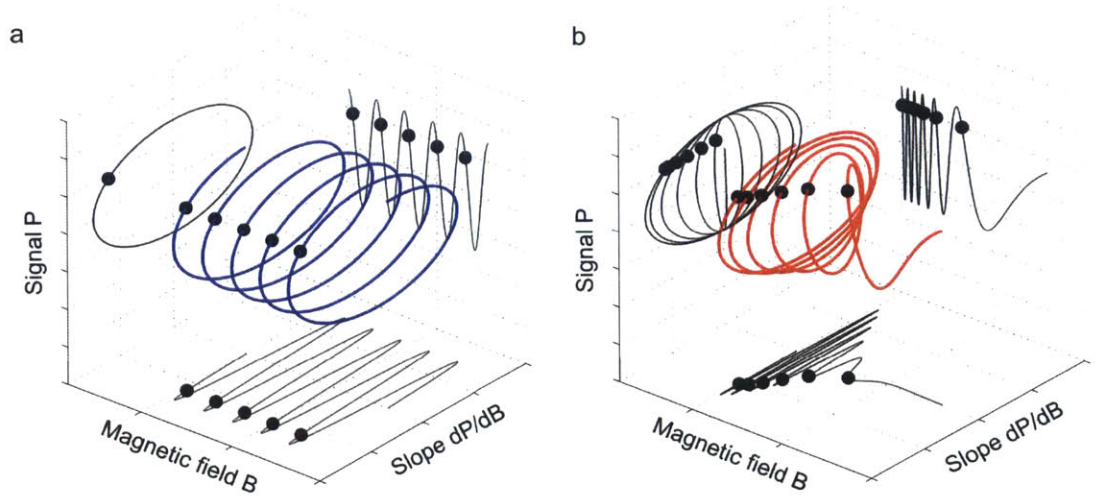

Figure D-2: Graphical representation of 2π phase unwrapping. Magnetometry signal P and slope dP/dB are plotted against magnetic field B. The gray curves are projections. **a**, Dynamic phase approach. All data points lie on a single circle on the $(P, dP/dB)$ plane. There are infinite possibilities of magnetic field value (black dots) that are projected onto the same single point on the $(P, dP/dB)$ plane. Adding a magnetic field offset doesn't solve this degeneracy because moving to another magnetic field value just results in another set of degeneracy. **b**, Geometric phase approach. Since the magnetometry oscillation $P(B)$ is chirped, there are only finite possibilities of magnetic field value (black dots) that give the same signal. Moreover, one can resolve the degeneracy by looking at the slope because the data points except for $P = \pm 1$ are spread over the $(P, dP/dB)$ plane. Even if the signal is measured to be $P = \pm 1$, once can still resolve the degeneracy by moving to a different point.

magnetic field offset. In Fig. D-2a, the dynamic phase signal is plotted in 3D as a function of magnetic field B, signal P_d, and derivative dP_d/dB. When the dynamic phase magnetometry curve is projected onto the $(P_d, dP_d/dB)$ plane, all data points lie on a 1D circle, given by

$$P_d^2 + (\gamma T)^{-2} \left(\frac{dP_d}{dB} \right)^2 = 1. \tag{D.10}$$

Even if a magnetic field offset is added, one encounters another set of infinite degeneracies. For this reason, the degeneracy of dynamic phase magnetometry signal can be resolved only if the interaction time T is changed (for example, quantum phase estimation algorithm). On the $(P_d, dP_d/dB)$ plane, this approach is understood as changing the radius of circle. In conclusion, the key idea behind 2π phase unwrapping resides in spreading the degenerate curve across the two dimensional space.

The geometric phase signal and its derivative are

$$P_g(B) = \cos \left[4\pi N \left(1 - \frac{\gamma B}{\sqrt{(\gamma B)^2 + \Omega^2}} \right) \right] \tag{D.11a}$$

$$\frac{dP_g(B)}{dB} = \frac{4\pi N \gamma \Omega^2}{((\gamma B)^2 + \Omega^2)^{\frac{3}{2}}} \sin \left[4\pi N \left(1 - \frac{\gamma B}{\sqrt{(\gamma B)^2 + \Omega^2}} \right) \right]. \tag{D.11b}$$

For any given value of $P_g \neq \pm 1$, there are only finite degeneracies of magnetic field values. They are related by

$$\frac{\gamma B_m}{\sqrt{(\gamma B_m)^2 + \Omega^2}} = \frac{\gamma B}{\sqrt{(\gamma B)^2 + \Omega^2}} + \frac{m}{2N}, \tag{D.12}$$

where m is an integer, which satisfies $|m| < 2N$. This degeneracy can be resolved by measuring the slope because the slope decreases monotonically across a fixed value of P_g unless $P_g = \pm 1$. This concept can also be presented clearly by plotting the geometric phase signal in 3D (Fig. D-2b). In contrast to dynamic phase, the geometric

phase magnetometry curve, projected onto the $(P_g, dP_g/dB)$ plane, does not lie on a 1D circle. All data points except for $(P_g = \pm 1, dP_g/dB = 0)$ are spread across two dimensional map and the degeneracy is resolved. It is also noted that even if $P = \pm 1$ is measured, one can always add a microwave frequency detuning to look for $P_g \neq \pm 1$. In summary, the geometric phase magnetometry protocol is as follows:

- Step 1: Measure the signal P_g and slope dP_g/dB.
- Step 2: Identify the corresponding magnetic field value B. If the measured signal and slope leaves an ambiguity, for example $(P_g = \pm 1, dP_g/dB = 0)$, add a microwave frequency offset and repeat the measurement.
- Step 3: The highest slope for high-sensitivity magnetometry is accessible by tuning a microwave frequency.

In the experiment, the NV spin has three hyperfine transitions. The dynamic phase magnetometry signal becomes

$$P_d(B) = \frac{1}{3} \sum_{m_I=-1,0,+1} \cos\left[(\gamma B + m_I \omega_{\mathrm{HF}})T\right] = \cos(\gamma B T)\left[1 + 2\cos(\omega_{\mathrm{HF}} T)\right], \quad \text{(D.13)}$$

where $\omega_{\mathrm{HF}} = 2\pi \times 2.16$ MHz. The hyperfine transitions only introduce an envelope modulation to P_d, which merely changes the radius of the circle in $(P, dP/dB)$, so that all data points still lie on the same circle. Thus, it is not possible to resolve the degeneracy either by measuring the slope or moving to other magnetic field values. The geometric phase magnetometry signal with three hyperfine transitions is

$$P_g(B) = \frac{1}{3} \sum_{m_I=-1,0,+1} \cos\left[4\pi N\left(1 - \frac{\gamma B + m_I \omega_{\mathrm{HF}}}{\sqrt{(\gamma B + m_I \omega_{\mathrm{HF}})^2 + \Omega^2}}\right)\right]. \quad \text{(D.14)}$$

The hyperfine transitions introduce a complicated modulation. In particular, degeneracy points can appear at $P \neq \pm 1$. However, since the data points are spread across

the two-dimensional $(P, dP/dB)$ space, the degeneracy can always be resolved by moving to a different magnetic field value. Although it is difficult to derive an analytical expression for 2π phase unwrapping in general, exploring the following three cases are sufficient to cover the parameter space:

- $\gamma|B| \gg \omega_{\mathrm{HF}}$: $P_g(B) \sim \cos\left[4\pi N\left(1 - \frac{\gamma B}{\sqrt{(\gamma B)^2+\Omega^2}}\right)\right] + O(\omega_{\mathrm{HF}}^2)$.
- $\gamma|B| \sim \omega_{\mathrm{HF}} \ll \Omega$: $P_g(B) \sim \cos\left[4\pi N\left(1 - \frac{\gamma B}{\Omega}\right)\right]\left(1 + 2\cos\left[4\pi N\left(1 - \frac{\omega_{\mathrm{HF}}}{\Omega}\right)\right]\right)$.
- $\gamma|B| \sim \omega_{\mathrm{HF}} \geq \Omega$: approximation is difficult. However, this parameter range is of importance for neither high-dynamic-range nor high-sensitivity magnetometry.

D.3 Sensitivity and Maximum Detectable Field

To calculate the sensitivity and dynamic-range, the average change of fluorescence per measurement is recast as $\Delta FL = \alpha\beta$, where $\alpha \sim 10$ % is the fluorescence contrast, and $\beta \sim 0.015$ is the average number of photons collected per measurement. The sensitivity is given by

$$\eta \approx \frac{1}{\mathrm{SNR}} \frac{1}{|dP/dB|_{\max}} \sqrt{t_m}, \tag{D.15}$$

where $\mathrm{SNR} = \Delta FL/\sqrt{\beta} = \alpha\sqrt{\beta}$ represents the signal-to-noise ratio of a single measurement, $|dP/dB|_{\max}$ is the maximum slope of the magnetometry curve, and $t_m \approx T$ is the measurement time. For dynamic phase magnetometry, the maximum slope is $|dP_d/dB|_{\max} = \gamma T$, and then the sensitivity is

$$\eta \approx \frac{1}{\gamma\alpha\sqrt{\beta}} \frac{1}{\sqrt{T}}. \tag{D.16}$$

The maximum field-range is defined as the half cycle of magnetometry oscillation:

$$B_{\max} \approx \frac{\pi}{\gamma T}. \tag{D.17}$$

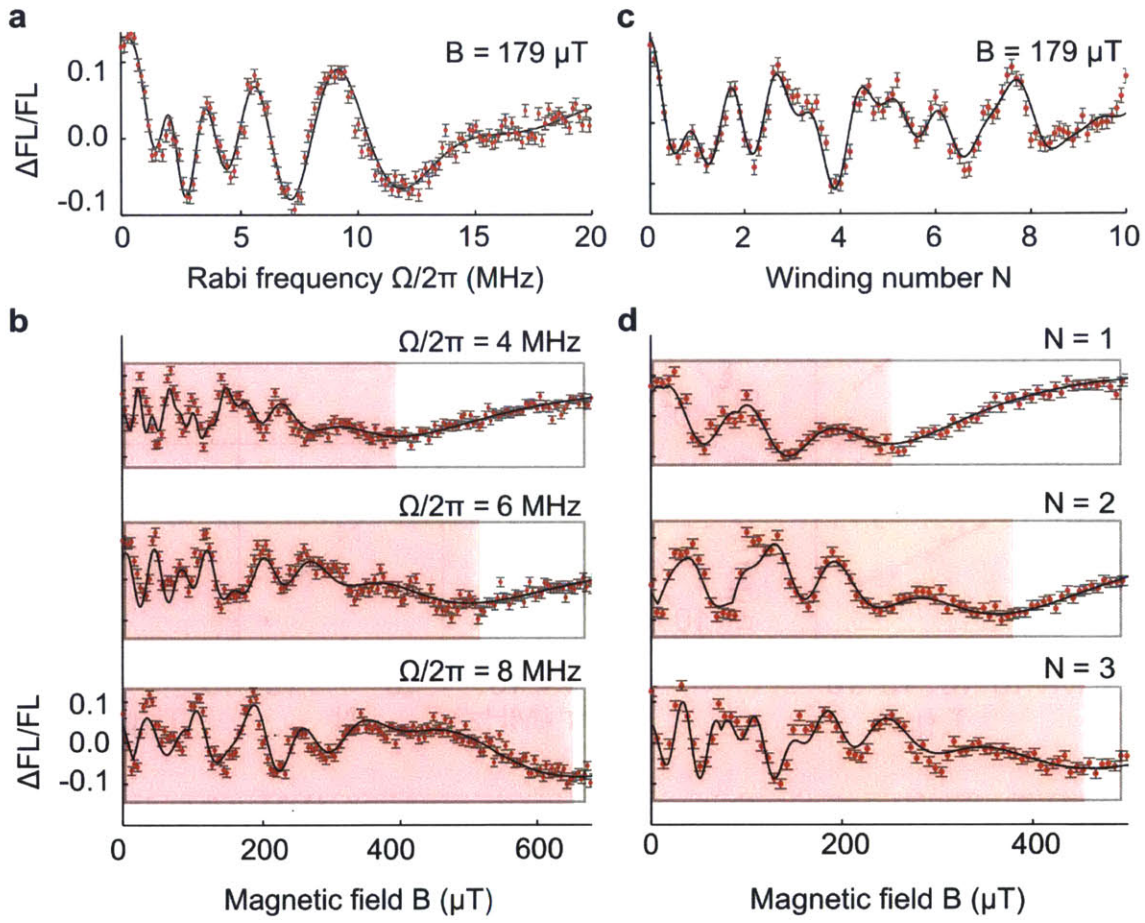

Figure D-3: Dependence of geometric phase magnetometry signal on geometrical parameters. **a-d**, Dots represent measured geometric phase magnetometry data with various values of Rabi frequency Ω and winding number N. The vertical axis is the signal, defined by the change of signal fluorescence count (ΔFL) normalized by the reference fluorescence count (FL). Error bars indicate 1σ photon shot-noise. Black lines show fit to the analytical expression of geometric phase signal including three hyperfine transitions. The red shaded regions indicate the dynamic range defined at the last minimum. Fixed parameters used in these measurements are: (**a**) $B = 179$ μT, $N = 3$, $T = 10$ μs, (**b**) $\Omega/2\pi = 4, 6, 8$ MHz, $N = 3$, $T = 10$ μs, (**c**) $B = 179$ μT, $\Omega/2\pi = 5$, $T = 10$ μs, and (**d**) $\Omega/2\pi = 5$ MHz, $N = 1, 2, 3$, $T = 10$ μs.

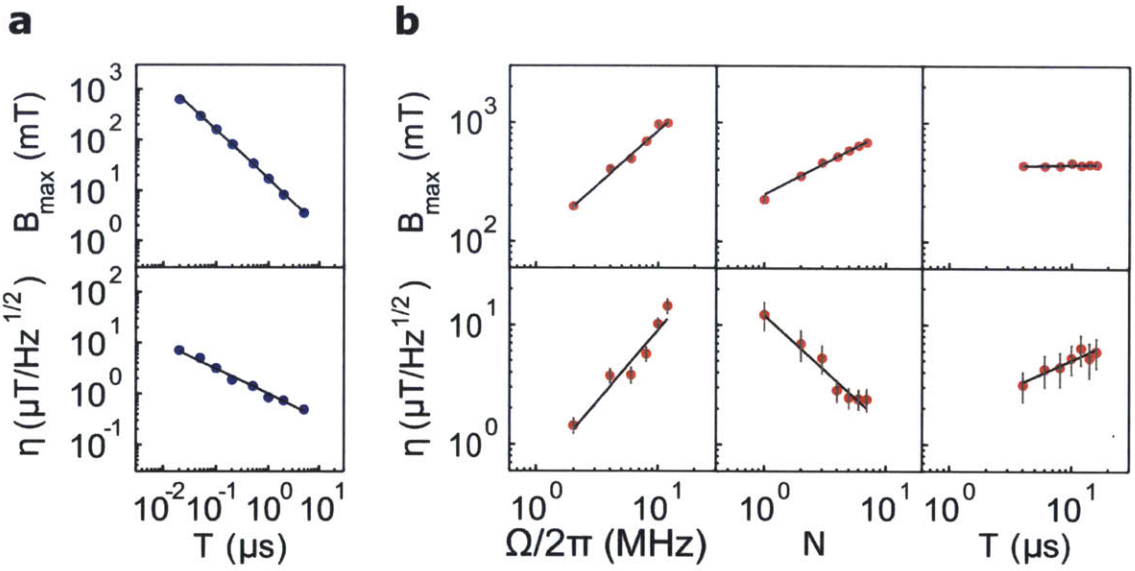

Figure D-4: Scaling of sensitivity and dynamic range on three control parameters. **a**, Measured sensitivity and field range of dynamic phase magnetometry as a function of interaction time T. The theoretical model predicts $\eta \propto T^{-1/2}$ and $B_{\max} \propto T^{-1}$, and the measurement gives $\eta \propto T^{-0.49(6)}$ and $B_{\max} \propto T^{-0.96(2)}$. **b**, Measured sensitivities and field-ranges of geometric phase magnetometry as a function of Rabi frequency Ω, winding number N, and interaction time T. The theoretical model predicts $\eta \propto \Omega^1 N^{-1} T^{1/2}$ and $B_{\max} \propto \Omega^1 N^{1/2} T^0$, and the measurements give $\eta \propto \Omega^{1.2(5)} N^{-0.92(1)} T^{0.46(1)}$ and $B_{\max} \propto \Omega^{0.9(1)} N^{0.52(1)} T^{0.02(1)}$. (**a**, **b**) The dots represent measured data points and lines are linear fit.

For the geometric phase magnetometry, the maximum slope of the curve is given by $|dP_g/dB|_{\max} = 4\pi\gamma N\Omega^{-1}$, and then the sensitivity is

$$\eta \approx \frac{1}{\gamma\alpha\sqrt{\beta}}\frac{\Omega\sqrt{T}}{4\pi N} = \frac{1}{\gamma\alpha\sqrt{\beta}}\frac{1}{2A\sqrt{T}}, \tag{D.18}$$

where $A = 2\pi N/\Omega T$ is the adiabaticity parameter evaluated at $B \approx 0$. The maximum field-range is defined at the point where the last minimum of chirped curve is: $\phi_g(B_{\max}) = 4\pi N(1 - \gamma B_{\max}/\sqrt{(\gamma B_{\max})^2 + \Omega^2}) = \pi$. By defining a small parameter, $\epsilon \equiv \phi_g/4\pi N \ll 1$, the above equation can be solved in terms of $B_{\max}$ to first order:

$$B_{\max} \approx \sqrt{2N}\Omega. \tag{D.19}$$

The scaling of sensitivity and dynamic range derived here is confirmed in experiments (Fig. D-3& D-4).

D.4 Geometric Phase Coherence Theory

If the qubit interacts with an environment with random noise, the Larmor vector will experience a perturbation:

$$\boldsymbol{R}(t) = \boldsymbol{R}_0(t) + \delta\boldsymbol{R}(t). \tag{D.20}$$

The second term, assumed to be smaller than the first term, is a classical random variable representing fluctuation of the energy splitting due to coupling to the environmental noise. When the measurement is repeated, the qubit acquires a different phase each time. Then the system is described by a mixed state using a density matrix, which is obtained by weighting the appropriate probability p for each environment condition,

$$\rho(t_f) = pU(t_i, t_f)\rho(t_i)U^{\dagger}(t_i, t_f), \tag{D.21}$$

where $\rho(t_i) = |\psi(t_i)\rangle\langle\psi(t_i)|$ is the initial density matrix at time $t = t_i$ constructed from a pure initial state. In particular, the diagonal elements give the probability of occupying each state, and the off-diagonal elements measure the coherence between these states. Thus, the coherence is defined as the off-diagonal component of density matrix averaged over many realizations:

$$W(t_i, t_f) = \frac{|\langle\rho_{\pm}(t_f)\rangle|}{|\langle\rho_{\pm}(t_i)\rangle|}. \tag{D.22}$$

For magnetic field sensing, the longitudinal magnetic fluctuations are of main interest as a decoherence source, so that $\delta\boldsymbol{R} = (0, 0, \delta R)$ is considered in the following calculations. First, the dynamic phase fluctuation is given by

$$\delta\phi_d(t_i, t_f) = \int_{t_i}^{t_f} \frac{R_z}{R}\delta R dt'. \tag{D.23}$$

Since we know that the dynamic phase is canceled by an echo operation, we consider only the fluctuation term. Next, the geometric phase fluctuation. The Berry connection is modified as

$$A_\rho \to A'_\rho = A_\rho + \partial_\theta A_\rho \delta\theta = \frac{1}{2}\cos\theta + \frac{1}{2}\delta(\cos\theta). \tag{D.24}$$

The second term describes the fluctuation of the polar angle due to the fluctuating field δR. The cyclic path is also perturbed due to the fluctuation:

$$dC_\phi \to dC'_\phi = N\frac{dt'}{t} + \delta N\frac{dt'}{t}. \tag{D.25}$$

The first term corresponds to the speed of rotation, and the second term gives the first order correction due to the fluctuation. The geometric phase fluctuation is then

given by

$$\delta\phi_g(t_i,t_f)=\frac{N\pi}{t_f-t_i}\int_{t_i}^{t_f}\delta(\cos\theta)dt'=\frac{N\pi}{t_f-t_i}\int_{t_i}^{t_f}\left[\frac{R^2-R_z^2}{R^3}\right]\delta R dt'\approx A\int_{t_i}^{t_f}\delta R dt'. \tag{D.26}$$

Here the definition of adiabaticity $A=\dot{\phi}\sin\theta/2R$ is used. The final state is

$$|\psi(T)\rangle=-\frac{i}{\sqrt{2}}\left(e^{+\frac{i}{2}\delta\phi_{\rm tot}(0,T)}|+\rangle+e^{-\frac{i}{2}\delta\phi_{\rm tot}(0,T)}|-\rangle\right), \tag{D.27}$$

where $\delta\phi_{\rm tot}(0,T)=\delta\phi_d(0,T/2)-\delta\phi_d(T/2,T)+\delta\phi_g(0,T/2)-\delta\phi_g(T/2,T)$. It is important to remind that the direction of revolution is switched between the first and second Berry pulses. Finally, the coherence becomes

$$W(0,T)=\left\langle\exp\left[-i\frac{R_z}{R}\int_0^T\delta R f_1(T;t)dt-iA\int_0^T\delta R f_0(T;t)dt\right]\right\rangle, \tag{D.28}$$

where $f_n(T;t)=\sum_{k=0}^{n}(-1)^k\Theta(t_{k+1}-t)\Theta(t-t_k)$ is a function that characterizes the pulse sequence. Θ is the Heaviside step function and $t_0=0,t_{n+1}=T$.

If the noise distribution is assumed to follow a Gaussian distribution with a zero mean $\langle\delta R(t)\rangle=0$, then the coherence function can be reduced to the two-point correlation function

$$S(t_i,t_f)=\langle\delta R(t_i)\delta R(t_f)\rangle \tag{D.29}$$

using the Wick's theorem: $W(0,T)\sim\langle e^{-i\delta R}\rangle\sim\exp\left[-\langle\delta R\delta R\rangle/2\right]$. Then the coherence can be analyzed in the frequency domain by use of the spectral density of the noise:

$$S(\omega)=\int_{\infty}^{+\infty}dte^{i\omega t}S(t). \tag{D.30}$$

We also define the decoherence function as

$$\chi(T)=-\log W(T). \tag{D.31}$$

The cross term between the dynamic and geometric part becomes zero because the sequence functions f_1 and f_0 have an opposite parity. Thus, the decoherence function reduces to two terms

$$\chi(T) = \chi_d(T) + \chi_g(T), \tag{D.32}$$

$$\begin{aligned}
\chi_d(T) =& \frac{1}{2}\left(\frac{R_z}{R}\right)^2 \int_0^T dt_a \int_0^T dt_b \langle \delta R(t_a)\delta R(t_b)\rangle f_1(T;t_a) f_1(T;t_b) \\
=& \left(\frac{R_z}{R}\right)^2 \int_0^\infty \frac{d\omega}{\pi} S(\omega) \frac{F_1(\omega T)}{\omega^2} \qquad \text{(D.33a)} \\
\chi_g(T) =& \frac{1}{2} A^2 \int_0^T dt_a \int_0^T dt_b \langle \delta R(t_a)\delta R(t_b)\rangle f_0(T;t_a) f_0(T;t_b) \\
=& A^2 \int_0^\infty \frac{d\omega}{\pi} S(\omega) \frac{F_0(\omega T)}{\omega^2}. \qquad \text{(D.33b)}
\end{aligned}$$

Here $F_0(\omega T) = \frac{\omega^2}{2}|\mathrm{FT}(f_0)|^2 = 2\sin^2\frac{\omega T}{2}$ and $F_1(\omega T) = \frac{\omega^2}{2}|\mathrm{FT}(f_1)|^2 = 8\sin^4\frac{\omega T}{4}$ are the filter functions of the pulse sequence.

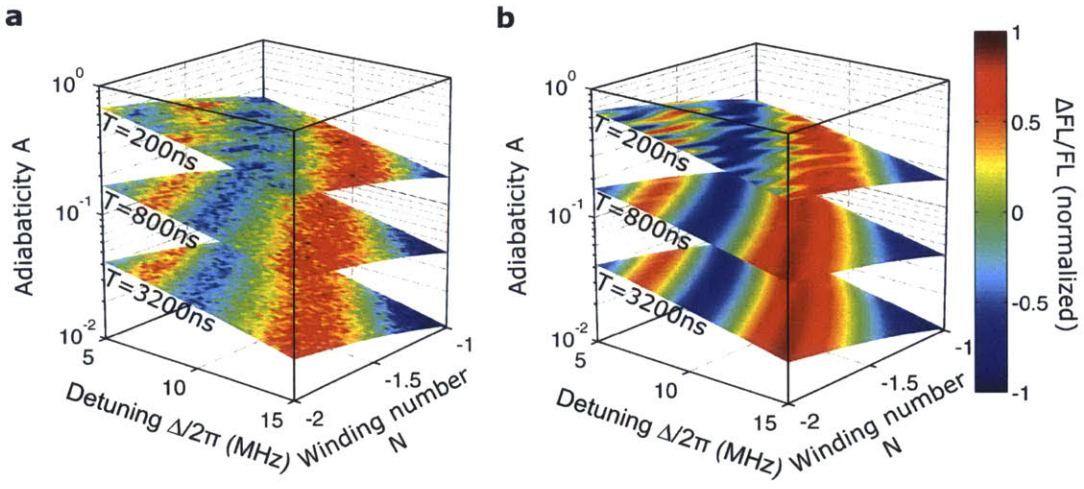

Figure D-5: Measurement and simulation of geometric phase signal in the non-adiabatic regime. **a**, Measurement of the cosine of geometric phase as a function of microwave frequency detuning Δ and winding number N with a fixed Rabi frequency of $\Omega/2\pi = 13$ MHz. Three layers represent isochrone planes at $T = 200, 800, 3200$ ns. The vertical axis is adiabaticity $A = \dot{\rho} \sin\theta/2R$, where $R = (\Omega^2 + \Delta^2)^{1/2}$. The amplitude of each hyperfine oscillations is extracted by fitting the 1D cross section data along Δ at $N = -2, T = 3200$ ns to the analytical expression of geometric phase signal with three hyperfine transitions. The measured signal is normalized to the mean of these three amplitudes. The analytical expression of the geometric phase signal is independent of the interaction time T. The layers at $T = 200$ ns and 800 ns ($0.01 < A < 0.2$) look the same as expected. However, the layer at $T = 200$ ns ($A > 0.2$) looks quite different from the other two, indicating that the analytical expression becomes invalid in the nonadiabatic regime. **b**, Simulation of the cosine of geometric phase including three hyperfine transitions with the relative amplitudes obtained in **a** (see also Section 5.7). The measurement and simulation agree, indicating that the time evolution of spin state is described deterministically by the Schrödinger equation even in the non-adiabatic regime.

Bibliography

[1] A. A. Abdumalikov Jr, J. M. Fink, K. Juliusson, M. Pechal, S. Berger, A. Wallraff, and S. Filipp. Experimental realization of non-Abelian non-adiabatic geometric gates. *Nature*, 496(7446):482–485, apr 2013.

[2] J. Achard, F. Silva, O. Brinza, A. Tallaire, and A. Gicquel. Coupled effect of nitrogen addition and surface temperature on the morphology and the kinetics of thick CVD diamond single crystals. *Diamond and Related Materials*, 16(4-7):685–689, apr 2007.

[3] J. Achard, A. Tallaire, R. Sussmann, F. Silva, and A. Gicquel. The control of growth parameters in the synthesis of high-quality single crystalline diamond by CVD. *Journal of Crystal Growth*, 284(3-4):396–405, nov 2005.

[4] V. M. Acosta. *Optical Magnetometry with Nitrogen-Vacancy Centers in Diamond.* PhD thesis, University of California, Berkeley, 2011.

[5] V. M. Acosta, E. Bauch, M. P. Ledbetter, A. Waxman, L.-S. Bouchard, and D. Budker. Temperature Dependence of the Nitrogen-Vacancy Magnetic Resonance in Diamond. *Physical Review Letters*, 104(7):070801, feb 2010.

[6] Y. Aharonov and J. Anandan. Phase change during a cyclic quantum evolution. *Physical Review Letters*, 58(16):1593–1596, apr 1987.

[7] C. D. Aiello. *Qubit Dynamics under Alternating Controls.* PhD thesis, Massachusetts Institute of Technology, 2014.

[8] A. Ajoy and P. Cappellaro. Stable three-axis nuclear-spin gyroscope in diamond. *Physical Review A*, 86(6):062104, dec 2012.

[9] A. Ajoy and P. Cappellaro. Quantum Simulation via Filtered Hamiltonian Engineering: Application to Perfect Quantum Transport in Spin Networks. *Physical Review Letters*, 110(22):220503, may 2013.

[10] F. Allmendinger, W. Heil, S. Karpuk, W. Kilian, A. Scharth, U. Schmidt, A. Schnabel, Y. Sobolev, and K. Tullney. New Limit on Lorentz-Invariance- and CPT -Violating Neutron Spin Interactions Using a Free-Spin-Precession He. *Physical Review Letters*, 112(11):110801, mar 2014.

[11] J. Anandan. Non-adiabatic non-abelian geometric phase. *Physics Letters A*, 133(4-5):171–175, nov 1988.

[12] P. W. Anderson and J. M. Rowell. Probable Observation of the Josephson Superconducting Tunneling Effect. *Physical Review Letters*, 10(6):230–232, mar 1963.

[13] S. M. Anton, J. S. Birenbaum, S. R. O'Kelley, V. Bolkhovsky, D. A. Braje, G. Fitch, M. Neeley, G. C. Hilton, H.-M. Cho, K. D. Irwin, F. C. Wellstood, W. D. Oliver, A. Shnirman, and J. Clarke. Magnetic Flux Noise in dc SQUIDs: Temperature and Geometry Dependence. *Physical Review Letters*, 110(14):147002, apr 2013.

[14] K. Arai, C. Belthangady, H. Zhang, N. Bar-Gill, S. J. DeVience, P. Cappellaro, A. Yacoby, and R. L. Walsworth. Fourier magnetic imaging with nanoscale resolution and compressed sensing speed-up using electronic spins in diamond. *Nature Nanotechnology*, 10(10):859–864, aug 2015.

[15] G. B. Arfken and H. J. Weber. *Mathematical Methods for Physicists*. Academic Press, 6th edition, 2005.

[16] H. U. Auster, K. H. Glassmeier, W. Magnes, O. Aydogar, W. Baumjohann, D. Constantinescu, D. Fischer, K. H. Fornacon, E. Georgescu, P. Harvey, O. Hillenmaier, R. Kroth, M. Ludlam, Y. Narita, R. Nakamura, K. Okrafka, F. Plaschke, I. Richter, H. Schwarzl, B. Stoll, A. Valavanoglou, and M. Wiedemann. The THEMIS Fluxgate Magnetometer. In *The THEMIS Mission*, pages 235–264. Springer New York, New York, NY, 2009.

[17] M. Auzinsh, D. Budker, D. F. Kimball, S. M. Rochester, J. E. Stalnaker, A. O. Sushkov, and V. V. Yashchuk. Can a Quantum Nondemolition Measurement Improve the Sensitivity of an Atomic Magnetometer? *Physical Review Letters*, 93(17):173002, oct 2004.

[18] M. N. Baibich, J. M. Broto, A. Fert, F. N. Van Dau, F. Petroff, P. Etienne, G. Creuzet, A. Friederich, and J. Chazelas. Giant Magnetoresistance of (001)Fe/(001)Cr Magnetic Superlattices. *Physical Review Letters*, 61(21):2472–2475, nov 1988.

[19] G. Balasubramanian, I. Y. Chan, R. Kolesov, M. Al-Hmoud, J. Tisler, C. Shin, C. Kim, A. Wojcik, P. R. Hemmer, A. Krueger, T. Hanke, A. Leitenstorfer, R. Bratschitsch, F. Jelezko, and J. Wrachtrup. Nanoscale imaging magnetometry with diamond spins under ambient conditions. *Nature*, 455(7213):648–651, oct 2008.

[20] G. Balasubramanian, P. Neumann, D. Twitchen, M. Markham, R. Kolesov, N. Mizuochi, J. Isoya, J. Achard, J. Beck, J. Tissler, V. Jacques, P. R. Hemmer, F. Jelezko, and J. Wrachtrup. Ultralong spin coherence time in isotopically engineered diamond. *Nature Materials*, 8(5):383–387, may 2009.

[21] N. Bar-Gill, L. Pham, C. Belthangady, D. Le Sage, P. Cappellaro, J. Maze, M. Lukin, A. Yacoby, and R. Walsworth. Suppression of spin-bath dynamics for improved coherence of multi-spin-qubit systems. *Nature Communications*, 3:858, may 2012.

[22] N. Bar-Gill, L. Pham, A. Jarmola, D. Budker, and R. Walsworth. Solid-state electronic spin coherence time approaching one second. *Nature Communications*, 4:1743, apr 2013.

[23] D. R. Baselt, G. U. Lee, M. Natesan, S. W. Metzger, P. E. Sheehan, and R. J. Colton. A biosensor based on magnetoresistance technology. *Biosensors and Bioelectronics*, 13(7-8):731–739, oct 1998.

[24] I. Bayn, E. H. Chen, M. E. Trusheim, L. Li, T. Schröder, O. Gaathon, M. Lu, A. Stein, M. Liu, K. Kisslinger, H. Clevenson, and D. Englund. Generation of Ensembles of Individually Resolvable Nitrogen Vacancies Using Nanometer-Scale Apertures in Ultrahigh-Aspect Ratio Planar Implantation Masks. *Nano Letters*, 15(3):1751–1758, mar 2015.

[25] C. Belthangady, N. Bar-Gill, L. M. Pham, K. Arai, D. Le Sage, P. Cappellaro, and R. L. Walsworth. Dressed-State Resonant Coupling between Bright and Dark Spins in Diamond. *Physical Review Letters*, 110(15):157601, apr 2013.

[26] C. J. Berglund, L. R. Hunter, D. Krause, Jr., E. O. Prigge, M. S. Ronfeldt, and S. K. Lamoreaux. New Limits on Local Lorentz Invariance from Hg and Cs Magnetometers. *Physical Review Letters*, 75(10):1879–1882, sep 1995.

[27] B. A. Bernevig, T. L. Hughes, and S.-C. Zhang. Quantum Spin Hall Effect and Topological Phase Transition in HgTe Quantum Wells. *Science*, 314(5806):1757–1761, dec 2006.

[28] H. Bernien, B. Hensen, W. Pfaff, G. Koolstra, M. S. Blok, L. Robledo, T. H. Taminiau, M. Markham, D. J. Twitchen, L. Childress, and R. Hanson. Heralded entanglement between solid-state qubits separated by three metres. *Nature*, 497(7447):86–90, apr 2013.

[29] M. V. Berry. Quantal Phase Factors Accompanying Adiabatic Changes. *Proceedings of the Royal Society A: Mathematical, Physical and Engineering Sciences*, 392(1802):45–57, mar 1984.

[30] E. Betzig, G. H. Patterson, R. Sougrat, O. W. Lindwasser, S. Olenych, J. S. Bonifacino, M. W. Davidson, J. Lippincott-Schwartz, and H. F. Hess. Imaging Intracellular Fluorescent Proteins at Nanometer Resolution. *Science*, 313(5793):1642–1645, sep 2006.

[31] A. Beyzavi and N.-T. Nguyen. Programmable two-dimensional actuation of ferrofluid droplet using planar microcoils. *Journal of Micromechanics and Microengineering*, 20(1):015018, jan 2010.

[32] G. Binasch, P. Grünberg, F. Saurenbach, and W. Zinn. Enhanced magnetoresistance in layered magnetic structures with antiferromagnetic interlayer exchange. *Physical Review B*, 39(7):4828–4830, mar 1989.

[33] M. S. Blok. *Quantum measurement and real-time feedback with a spin-register in diamond.* PhD thesis, Delft University of Technology, 2015.

[34] N. Bohr. XXXVII. On the constitution of atoms and molecules. *Philosophical Magazine Series 6*, 26(153):476–502, sep 1913.

[35] J. J. Bollinger, W. M. Itano, D. J. Wineland, and D. J. Heinzen. Optimal frequency measurements with maximally correlated states. *Physical Review A*, 54(6):R4649–R4652, dec 1996.

[36] C. Bonato, M. S. Blok, H. T. Dinani, D. W. Berry, M. L. Markham, D. J. Twitchen, and R. Hanson. Optimized quantum sensing with a single electron spin using real-time adaptive measurements. *Nature Nanotechnology*, nov 2015.

[37] R. Bouchendira, P. Cladé, S. Guellati-Khélifa, F. Nez, and F. Biraben. New Determination of the Fine Structure Constant and Test of the Quantum Electrodynamics. *Physical Review Letters*, 106(8):080801, feb 2011.

[38] J. M. Brown, S. J. Smullin, T. W. Kornack, and M. V. Romalis. New Limit on Lorentz and CPT-Violating Neutron Spin Interactions. *Physical Review Letters*, 105(15):151604, oct 2010.

[39] A. D. Buckingham and P. J. Stephens. Magnetic Optical Activity. *Annual Review of Physical Chemistry*, 17(1):399–432, oct 1966.

[40] B. B. Buckley, G. D. Fuchs, L. C. Bassett, and D. D. Awschalom. Spin-Light Coherence for Single-Spin Measurement and Control in Diamond. *Science*, 330(6008):1212–1215, nov 2010.

[41] D. Budker and M. Romalis. Optical magnetometry. *Nature Physics*, 3(4):227–234, apr 2007.

[42] J. Cai, F. Jelezko, and M. B. Plenio. Hybrid sensors based on colour centres in diamond and piezoactive layers. *Nature Communications*, 5, jun 2014.

[43] J. Cai, A. Retzker, F. Jelezko, and M. B. Plenio. A large-scale quantum simulator on a diamond surface at room temperature. *Nature Physics*, 9(3):168–173, jan 2013.

[44] E. Candes, J. Romberg, and T. Tao. Robust uncertainty principles: exact signal reconstruction from highly incomplete frequency information. *IEEE Transactions on Information Theory*, 52(2):489–509, feb 2006.

[45] H. Y. Carr and E. M. Purcell. Effects of Diffusion on Free Precession in Nuclear Magnetic Resonance Experiments. *Physical Review*, 94(3):630–638, may 1954.

[46] A. M. Chang, H. D. Hallen, L. Harriott, H. F. Hess, H. L. Kao, J. Kwo, R. E. Miller, R. Wolfe, J. van der Ziel, and T. Y. Chang. Scanning Hall probe microscopy. *Applied Physics Letters*, 61(16):1974, 1992.

[47] A. Chayahara, Y. Mokuno, Y. Horino, Y. Takasu, H. Kato, H. Yoshikawa, and N. Fujimori. The effect of nitrogen addition during high-rate homoepitaxial growth of diamond by microwave plasma CVD. *Diamond and Related Materials*, 13(11-12):1954–1958, nov 2004.

[48] E. H. Chen, O. Gaathon, M. E. Trusheim, and D. Englund. Wide-Field Multispectral Super-Resolution Imaging Using Spin-Dependent Fluorescence in Nanodiamonds. *Nano Letters*, 13(5):2073–2077, may 2013.

[49] L. Childress. *Coherent Manipulation of Single Quantum Systems in the Solid State.* PhD thesis, Harvard University, 2006.

[50] L. Childress, M. V. Gurudev Dutt, J. M. Taylor, A. S. Zibrov, F. Jelezko, J. Wrachtrup, P. R. Hemmer, and M. D. Lukin. Coherent Dynamics of Coupled Electron and Nuclear Spin Qubits in Diamond. *Science*, 314(5797):281–285, oct 2006.

[51] L. Childress, R. Walsworth, and M. Lukin. Atom-like crystal defects: From quantum computers to biological sensors. *Physics Today*, 67(10):38–43, oct 2014.

[52] C.-H. Chiou, Y.-Y. Huang, M.-H. Chiang, H.-H. Lee, and G.-B. Lee. New magnetic tweezers for investigation of the mechanical properties of single DNA molecules. *Nanotechnology*, 17(5):1217–1224, mar 2006.

[53] C.-H. Chiou and G.-B. Lee. A micromachined DNA manipulation platform for the stretching and rotation of a single DNA molecule. *Journal of Micromechanics and Microengineering*, 15(1):109–117, jan 2005.

[54] Y. Chu. *Quantum optics with atom-like systems in diamond.* PhD thesis, Harvard University, 2014.

[55] H. Clevenson, M. E. Trusheim, C. Teale, T. Schröder, D. Braje, and D. Englund. Broadband magnetometry and temperature sensing with a light-trapping diamond waveguide. *Nature Physics*, 11(5):393–397, apr 2015.

[56] J. Daughton. GMR applications. *Journal of Magnetism and Magnetic Materials*, 192(2):334–342, feb 1999.

[57] G. Davies and M. F. Hamer. Optical Studies of the 1.945 eV Vibronic Band in Diamond. *Proceedings of the Royal Society A: Mathematical, Physical and Engineering Sciences*, 348(1653):285–298, feb 1976.

[58] G. De Chiara and G. M. Palma. Berry phase for a spin 1/2 particle in a classical fluctuating field. *Physical review letters*, 91(9):090404, aug 2003.

[59] G. de Lange. *Quantum control and coherence of interacting spins in diamond.* PhD thesis, Delft University of Technology, 2012.

[60] G. de Lange, Z. H. Wang, D. Riste, V. V. Dobrovitski, and R. Hanson. Universal Dynamical Decoupling of a Single Solid-State Spin from a Spin Bath. *Science*, 330(6000):60–63, oct 2010.

[61] C. L. Degen, M. Poggio, H. J. Mamin, C. T. Rettner, and D. Rugar. Nanoscale magnetic resonance imaging. *Proceedings of the National Academy of Sciences*, 106(5):1313–1317, feb 2009.

[62] D. M. Dennison. A Note on the Specific Heat of the Hydrogen Molecule. *Proceedings of the Royal Society A: Mathematical, Physical and Engineering Sciences*, 115(771):483–486, jul 1927.

[63] S. J. DeVience. *Nuclear Magnetic Resonance with Spin Singlet States and Nitrogen Vacancy Centers in Diamond.* PhD thesis, Harvard University, 2014.

[64] S. J. DeVience, L. M. Pham, I. Lovchinsky, A. O. Sushkov, N. Bar-Gill, C. Belthangady, F. Casola, M. Corbett, H. Zhang, M. Lukin, H. Park, A. Yacoby, and R. L. Walsworth. Nanoscale NMR spectroscopy and imaging of multiple nuclear species. *Nature Nanotechnology*, 10(2):129–134, jan 2015.

[65] P. A. M. Dirac. The Quantum Theory of the Electron. *Proceedings of the Royal Society A: Mathematical, Physical and Engineering Sciences*, 117(778):610–624, feb 1928.

[66] J. Dobson. Magnetic Iron Compounds in Neurological Disorders. *Annals of the New York Academy of Sciences*, 1012(1):183–192, mar 2004.

[67] M. W. Doherty, V. V. Struzhkin, D. A. Simpson, L. P. McGuinness, Y. Meng, A. Stacey, T. J. Karle, R. J. Hemley, N. B. Manson, L. C. L. Hollenberg, and S. Prawer. Electronic properties and metrology applications of the diamond NV- center under pressure. *Physical review letters*, 112(4):047601, jan 2014.

[68] F. Dolde. Electric-field sensing using single diamond spins. *Nature Phys.*, 7:459–463, 2011.

[69] F. Dolde. *The nitrogen vacancy center in internal and external fields.* PhD thesis, University of Stuttgart, 2014.

[70] F. Dolde, I. Jakobi, B. Naydenov, N. Zhao, S. Pezzagna, C. Trautmann, J. Meijer, P. Neumann, F. Jelezko, and J. Wrachtrup. Room-temperature entanglement between single defect spins in diamond. *Nature Physics*, 9(3):139–143, feb 2013.

[71] O. Draper, M. E. Byrne, Z. Li, S. Keyhani, J. C. Barrozo, G. Jensen, and A. Komeili. MamK, a bacterial actin, forms dynamic filaments in vivo that are regulated by the acidic proteins MamJ and LimJ. *Molecular microbiology*, 82(2):342–54, oct 2011.

[72] M. Drndić, K. S. Johnson, J. H. Thywissen, M. Prentiss, and R. M. Westervelt. Micro-electromagnets for atom manipulation. *Applied Physics Letters*, 72(22):2906, 1998.

[73] M. Drndić, C. S. Lee, and R. M. Westervelt. Three-dimensional microelectromagnet traps for neutral and charged particles. *Physical Review B*, 63(8):085321, feb 2001.

[74] L.-M. Duan. Geometric Manipulation of Trapped Ions for Quantum Computation. *Science*, 292(5522):1695–1697, jun 2001.

[75] R. E. Dunin-Borkowski. Magnetic Microstructure of Magnetotactic Bacteria by Electron Holography. *Science*, 282(5395):1868–1870, dec 1998.

[76] M. V. G. Dutt, L. Childress, L. Jiang, E. Togan, J. Maze, F. Jelezko, A. S. Zibrov, P. R. Hemmer, and M. D. Lukin. Quantum Register Based on Individual Electronic and Nuclear Spin Qubits in Diamond. *Science*, 316(5829):1312–1316, jun 2007.

[77] S. H. K. Eder, H. Cadiou, A. Muhamad, P. A. McNaughton, J. L. Kirschvink, and M. Winklhofer. Magnetic characterization of isolated candidate vertebrate magnetoreceptor cells. *Proceedings of the National Academy of Sciences*, 109(30):12022–12027, jul 2012.

[78] A. M. Edmonds, U. F. S. D'Haenens-Johansson, R. J. Cruddace, M. E. Newton, K.-M. C. Fu, C. Santori, R. G. Beausoleil, D. J. Twitchen, and M. L. Markham. Production of oriented nitrogen-vacancy color centers in synthetic diamond. *Physical Review B*, 86(3):035201, jul 2012.

[79] R. R. Ernst. Application of Fourier Transform Spectroscopy to Magnetic Resonance. *Review of Scientific Instruments*, 37(1):93, jun 1966.

[80] L. Essen and J. V. L. Parry. An Atomic Standard of Frequency and Time Interval: A Cæsium Resonator. *Nature*, 176(4476):280–282, aug 1955.

[81] D. Faivre and D. Schüler. Magnetotactic Bacteria and Magnetosomes. *Chemical Reviews*, 108(11):4875–4898, nov 2008.

[82] P. Fellgett. On numerical Fourier transformation, with special reference to Lipson-Beevers strips. *Journal of Scientific Instruments*, 35(7):257–258, jul 1958.

[83] S. Felton, A. M. Edmonds, M. E. Newton, P. M. Martineau, D. Fisher, D. J. Twitchen, and J. M. Baker. Hyperfine interaction in the ground state of the negatively charged nitrogen vacancy center in diamond. *Physical Review B*, 79(7):075203, feb 2009.

[84] A. Fert. Nobel Lecture: Origin, development, and future of spintronics. *Reviews of Modern Physics*, 80(4):1517–1530, dec 2008.

[85] R. P. Feynman. Simulating physics with computers. *International Journal of Theoretical Physics*, 21(6-7):467–488, jun 1982.

[86] R. P. Feynman, F. L. Vernon, and R. W. Hellwarth. Geometrical Representation of the Schrödinger Equation for Sing Maser Problems. *Journal of Applied Physics*, 28(1):49, 1957.

[87] S. Filipp, J. Klepp, Y. Hasegawa, C. Plonka-Spehr, U. Schmidt, P. Geltenbort, and H. Rauch. Experimental Demonstration of the Stability of Berry's Phase for a Spin-1/2 Particle. *Physical Review Letters*, 102(3):030404, jan 2009.

[88] A. Finkler, Y. Segev, Y. Myasoedov, M. L. Rappaport, L. Ne'eman, D. Vasyukov, E. Zeldov, M. E. Huber, J. Martin, and A. Yacoby. Self-Aligned Nanoscale SQUID on a Tip. *Nano Letters*, 10(3):1046–1049, mar 2010.

[89] O. Florescu, M. Mattmann, and B. Boser. Fully integrated detection of single magnetic beads in complementary metal-oxide-semiconductor. *Journal of Applied Physics*, 103(4):046101, 2008.

[90] R. R. Fu, B. P. Weiss, E. A. Lima, R. J. Harrison, X.-N. Bai, S. J. Desch, D. S. Ebel, C. Suavet, H. Wang, D. Glenn, D. Le Sage, T. Kasama, R. L. Walsworth, and A. T. Kuan. Solar nebula magnetic fields recorded in the Semarkona meteorite. *Science*, 346(6213):1089–1092, nov 2014.

[91] G. D. Fuchs, V. V. Dobrovitski, D. M. Toyli, F. J. Heremans, and D. D. Awschalom. Gigahertz Dynamics of a Strongly Driven Single Quantum Spin. *Science*, 326(5959):1520–1522, dec 2009.

[92] T. Fukui, Y. Doi, T. Miyazaki, Y. Miyamoto, H. Kato, T. Matsumoto, T. Makino, S. Yamasaki, R. Morimoto, N. Tokuda, M. Hatano, Y. Sakagawa, H. Morishita, T. Tashima, S. Miwa, Y. Suzuki, and N. Mizuochi. Perfect selective alignment of nitrogen-vacancy centers in diamond. *Applied Physics Express*, 7(5):055201, may 2014.

[93] B. Fürtig, C. Richter, J. Wöhnert, and H. Schwalbe. NMR Spectroscopy of RNA. *ChemBioChem*, 4(10):936–962, oct 2003.

[94] A. Gali, M. Fyta, and E. Kaxiras. Ab initio supercell calculations on nitrogen-vacancy center in diamond: Electronic structure and hyperfine tensors. *Physical Review B*, 77(15):155206, apr 2008.

[95] M. Germann, T. Latychevskaia, C. Escher, and H.-W. Fink. Pulsed electron holography. *Applied Physics Letters*, 102(20):203115, 2013.

[96] V. Giovannetti. Quantum-Enhanced Measurements: Beating the Standard Quantum Limit. *Science*, 306(5700):1330–1336, nov 2004.

[97] D. R. Glenn, K. Lee, H. Park, R. Weissleder, A. Yacoby, M. D. Lukin, H. Lee, R. L. Walsworth, and C. B. Connolly. Single-cell magnetic imaging using a quantum diamond microscope. *Nature Methods*, 12(8):736–738, jun 2015.

[98] P. Glover and S. P. Mansfield. Limits to magnetic resonance microscopy. *Reports on Progress in Physics*, 65(10):1489–1511, oct 2002.

[99] D. L. Graham, H. A. Ferreira, and P. P. Freitas. Magnetoresistive-based biosensors and biochips. *Trends in Biotechnology*, 22(9):455–462, sep 2004.

[100] M. S. Grinolds, S. Hong, P. Maletinsky, L. Luan, M. D. Lukin, R. L. Walsworth, and A. Yacoby. Nanoscale magnetic imaging of a single electron spin under ambient conditions. *Nature Physics*, 9(4):215–219, feb 2013.

[101] M. S. Grinolds, P. Maletinsky, S. Hong, M. D. Lukin, R. L. Walsworth, and A. Yacoby. Quantum control of proximal spins using nanoscale magnetic resonance imaging. *Nature Physics*, 7(9):687–692, may 2011.

[102] M. S. Grinolds, M. Warner, K. De Greve, Y. Dovzhenko, L. Thiel, R. L. Walsworth, S. Hong, P. Maletinsky, and A. Yacoby. Subnanometre resolution in three-dimensional magnetic resonance imaging of individual dark spins. *Nature Nanotechnology*, 9(4):279–284, mar 2014.

[103] V. Gritsev and A. Polkovnikov. Dynamical quantum Hall effect in the parameter space. *Proceedings of the National Academy of Sciences*, 109(17):6457–6462, apr 2012.

[104] S. Groth, P. KruÌĹger, S. Wildermuth, R. Folman, T. Fernholz, J. Schmiedmayer, D. Mahalu, and I. Bar-Joseph. Atom chips: Fabrication and thermal properties. *Applied Physics Letters*, 85(14):2980, 2004.

[105] A. Gruber. Scanning Confocal Optical Microscopy and Magnetic Resonance on Single Defect Centers. *Science*, 276(5321):2012–2014, jun 1997.

[106] H. Gudbjartsson and S. Patz. The Rician distribution of noisy MRI data. *Magnetic resonance in medicine*, 34(6):910–4, dec 1995.

[107] E. L. Hahn. Spin Echoes. *Physical Review*, 80(4):580–594, nov 1950.

[108] F. D. M. Haldane. Model for a Quantum Hall Effect without Landau Levels: Condensed-Matter Realization of the "Parity Anomaly". *Physical Review Letters*, 61(18):2015–2018, oct 1988.

[109] L. T. Hall, C. D. Hill, J. H. Cole, B. Stadler, F. Caruso, P. Mulvaney, J. Wrachtrup, and L. C. L. Hollenberg. Monitoring ion-channel function in real time through quantum decoherence. *Proceedings of the National Academy of Sciences*, 107(44):18777–18782, nov 2010.

[110] J. H. Hannay. Angle variable holonomy in adiabatic excursion of an integrable Hamiltonian. *Journal of Physics A: Mathematical and General*, 18(2):221–230, feb 1985.

[111] D. Hanneke, S. Fogwell Hoogerheide, and G. Gabrielse. Cavity control of a single-electron quantum cyclotron: Measuring the electron magnetic moment. *Physical Review A*, 83(5):052122, may 2011.

[112] R. Hanson, O. Gywat, and D. D. Awschalom. Room-temperature manipulation and decoherence of a single spin in diamond. *Physical Review B*, 74(16):161203, oct 2006.

[113] R. Hanson, F. M. Mendoza, R. J. Epstein, and D. D. Awschalom. Polarization and Readout of Coupled Single Spins in Diamond. *Physical Review Letters*, 97(8):087601, aug 2006.

[114] S. R. Hartmann and E. L. Hahn. Nuclear Double Resonance in the Rotating Frame. *Physical Review*, 128(5):2042–2053, dec 1962.

[115] X.-F. He, N. B. Manson, and P. T. H. Fisk. Paramagnetic resonance of photoexcited N- V defects in diamond. II. Hyperfine interaction with the N 14 nucleus. *Physical Review B*, 47(14):8816–8822, apr 1993.

[116] H. Heidari, U. Gatti, E. Bonizzoni, and F. Maloberti. Low-noise low-Offset current-mode Hall sensors. In *Proceedings of the 2013 9th Conference on Ph.D. Research in Microelectronics and Electronics (PRIME)*, pages 325–328. IEEE, jun 2013.

[117] S. W. Hell and J. Wichmann. Breaking the diffraction resolution limit by stimulated emission: stimulated-emission-depletion fluorescence microscopy. *Optics Letters*, 19(11):780, jun 1994.

[118] B. Hensen, H. Bernien, A. E. Dréau, A. Reiserer, N. Kalb, M. S. Blok, J. Ruitenberg, R. F. L. Vermeulen, R. N. Schouten, C. Abellán, W. Amaya, V. Pruneri, M. W. Mitchell, M. Markham, D. J. Twitchen, D. Elkouss, S. Wehner, T. H. Taminiau, and R. Hanson. Loophole-free Bell inequality violation using electron spins separated by 1.3 kilometres. *Nature*, 526(7575):682–686, oct 2015.

[119] R. Hertel, S. Gliga, M. Fähnle, and C. M. Schneider. Ultrafast Nanomagnetic Toggle Switching of Vortex Cores. *Physical Review Letters*, 98(11):117201, mar 2007.

[120] B. E. Herzog, D. Cadeddu, F. Xue, P. Peddibhotla, and M. Poggio. Boundary between the thermal and statistical polarization regimes in a nuclear spin ensemble. *Applied Physics Letters*, 105(4):043112, jul 2014.

[121] M. Hirose. *Quantum Control of Spin Systems in diamond.* PhD thesis, Massachusetts Institute of Technology, 2015.

[122] M. A. Hohensee, N. Leefer, D. Budker, C. Harabati, V. A. Dzuba, and V. V. Flambaum. Limits on Violations of Lorentz Symmetry and the Einstein Equivalence Principle using Radio-Frequency Spectroscopy of Atomic Dysprosium. *Physical Review Letters*, 111(5):050401, jul 2013.

[123] K. Iakoubovskii, G. J. Adriaenssens, and M. Nesladek. Photochromism of vacancy-related centres in diamond. *Journal of Physics: Condensed Matter*, 12(2):189–199, jan 2000.

[124] R. C. Jaklevic, J. Lambe, A. H. Silver, and J. E. Mercereau. Quantum Interference Effects in Josephson Tunneling. *Physical Review Letters*, 12(7):159–160, feb 1964.

[125] F. Jelezko, T. Gaebel, I. Popa, A. Gruber, and J. Wrachtrup. Observation of Coherent Oscillations in a Single Electron Spin. *Physical Review Letters*, 92(7):076401, feb 2004.

[126] L. Jiang. *Towards Scalable Quantum Communication and Computation: Novel Approaches and Realizations.* PhD thesis, Harvard University, 2009.

[127] M. Johansson, E. Sjöqvist, L. M. Andersson, M. Ericsson, B. Hessmo, K. Singh, and D. M. Tong. Robustness of nonadiabatic holonomic gates. *Physical Review A*, 86(6):062322, dec 2012.

[128] K. S. Johnson, M. Drndic, J. H. Thywissen, G. Zabow, R. M. Westervelt, and M. Prentiss. Atomic Deflection Using an Adaptive Microelectromagnet Mirror. *Physical Review Letters*, 81(6):1137–1141, aug 1998.

[129] J. A. Jones, V. Vedral, A. Ekert, and G. Castagnoli. Geometric quantum computation using nuclear magnetic resonance. *Nature*, 403(6772):869–871, feb 2000.

[130] G. Jotzu, M. Messer, R. Desbuquois, M. Lebrat, T. Uehlinger, D. Greif, and T. Esslinger. Experimental realization of the topological Haldane model with ultracold fermions. *Nature*, 515(7526):237–240, nov 2014.

[131] C. Ju, C. Lei, X. Xu, D. Culcer, Z. Zhang, and J. Du. NV-center-based digital quantum simulation of a quantum phase transition in topological insulators. *Physical Review B*, 89(4):045432, jan 2014.

[132] B. E. Kane. A silicon-based nuclear spin quantum computer. *Nature*, 393(6681):133–137, may 1998.

[133] C. L. Kane and E. J. Mele. Quantum Spin Hall Effect in Graphene. *Physical Review Letters*, 95(22):226801, nov 2005.

[134] J. Kerr. XLIII. On rotation of the plane of polarization by reflection from the pole of a magnet. *Philosophical Magazine Series 5*, 3(19):321–343, may 1877.

[135] J.-S. Kim, M.-A. Mawass, A. Bisig, B. Krüger, R. M. Reeve, T. Schulz, F. Büttner, J. Yoon, C.-Y. You, M. Weigand, H. Stoll, G. Schütz, H. J. M. Swagten, B. Koopmans, S. Eisebitt, and M. Kläui. Synchronous precessional motion of multiple domain walls in a ferromagnetic nanowire by perpendicular field pulses. *Nature Communications*, 5, mar 2014.

[136] H. J. Kimble, Y. Levin, A. B. Matsko, K. S. Thorne, and S. P. Vyatchanin. Conversion of conventional gravitational-wave interferometers into quantum nondemolition interferometers by modifying their input and/or output optics. *Physical Review D*, 65(2):022002, dec 2001.

[137] A. Kitaev. Fault-tolerant quantum computation by anyons. *Annals of Physics*, 303(1):2–30, jan 2003.

[138] W. F. Koehl, B. B. Buckley, F. J. Heremans, G. Calusine, and D. D. Awschalom. Room temperature coherent control of defect spin qubits in silicon carbide. *Nature*, 479(7371):84–7, nov 2011.

[139] A. Komeili, H. Vali, T. J. Beveridge, and D. K. Newman. Magnetosome vesicles are present before magnetite formation, and MamA is required for their activation. *Proceedings of the National Academy of Sciences*, 101(11):3839–3844, mar 2004.

[140] I. K. Kominis, T. W. Kornack, J. C. Allred, and M. V. Romalis. A subfemtotesla multichannel atomic magnetometer. *Nature*, 422(6932):596–599, apr 2003.

[141] X. Kong, A. Stark, J. Du, L. P. McGuinness, and F. Jelezko. Towards Chemical Structure Resolution with Nanoscale Nuclear Magnetic Resonance Spectroscopy. *Physical Review Applied*, 4(2):024004, aug 2015.

[142] T. Koyama, D. Chiba, K. Ueda, H. Tanigawa, S. Fukami, T. Suzuki, N. Ohshima, N. Ishiwata, Y. Nakatani, and T. Ono. Magnetic field insensitivity of magnetic domain wall velocity induced by electrical current in Co/Ni nanowire. *Applied Physics Letters*, 98(19):192509, 2011.

[143] A. Krichevsky, M. J. Smith, L. J. Whitman, M. B. Johnson, T. W. Clinton, L. L. Perry, B. M. Applegate, K. O'Connor, and L. N. Csonka. Trapping motile magnetotactic bacteria with a magnetic recording head. *Journal of Applied Physics*, 101(1):014701, 2007.

[144] H. W. Kroto, J. R. Heath, S. C. O'Brien, R. F. Curl, and R. E. Smalley. C60: Buckminsterfullerene. *Nature*, 318(6042):162–163, nov 1985.

[145] G. Kucsko, P. C. Maurer, N. Y. Yao, M. Kubo, H. J. Noh, P. K. Lo, H. Park, and M. D. Lukin. Nanometre-scale thermometry in a living cell. *Nature*, 500(7460):54–8, aug 2013.

[146] N. D. Lai, D. Zheng, F. Jelezko, F. Treussart, and J.-F. Roch. Influence of a static magnetic field on the photoluminescence of an ensemble of nitrogen-vacancy color centers in a diamond single-crystal. *Applied Physics Letters*, 95(13):133101, 2009.

[147] K. P. Lam, A. P. Hitchcock, M. Obst, J. R. Lawrence, G. D. Swerhone, G. G. Leppard, T. Tyliszczak, C. Karunakaran, J. Wang, K. Kaznatcheev, D. A. Bazylinski, and U. Lins. Characterizing magnetism of individual magnetosomes by X-ray magnetic circular dichroism in a scanning transmission X-ray microscope. *Chemical Geology*, 270(1-4):110–116, feb 2010.

[148] A. Laraoui, F. Dolde, C. Burk, F. Reinhard, J. Wrachtrup, and C. A. Meriles. High-resolution correlation spectroscopy of ^{13}C spins near a nitrogen-vacancy centre in diamond. *Nature communications*, 4:1651, 2013.

[149] P. C. Lauterbur. Image Formation by Induced Local Interactions: Examples Employing Nuclear Magnetic Resonance. *Nature*, 242(5394):190–191, mar 1973.

[150] D. Le Sage, K. Arai, D. R. Glenn, S. J. DeVience, L. M. Pham, L. Rahn-Lee, M. D. Lukin, A. Yacoby, A. Komeili, and R. L. Walsworth. Optical magnetic imaging of living cells. *Nature*, 496(7446):486–489, apr 2013.

[151] D. Le Sage, L. M. Pham, N. Bar-Gill, C. Belthangady, M. D. Lukin, A. Yacoby, and R. L. Walsworth. Efficient photon detection from color centers in a diamond optical waveguide. *Physical Review B*, 85(12):121202, mar 2012.

[152] C. S. Lee, H. Lee, and R. M. Westervelt. Microelectromagnets for the control of magnetic nanoparticles. *Applied Physics Letters*, 79(20):3308, 2001.

[153] H. Lee, Y. Liu, D. Ham, and R. M. Westervelt. Integrated cell manipulation system–CMOS/microfluidic hybrid. *Lab on a chip*, 7(3):331–7, mar 2007.

[154] H. Lee, A. M. Purdon, V. Chu, and R. M. Westervelt. Controlled Assembly of Magnetic Nanoparticles from Magnetotactic Bacteria Using Microelectromagnets Arrays. *Nano Letters*, 4(5):995–998, may 2004.

[155] I. Lee, Y. Obukhov, G. Xiang, A. Hauser, F. Yang, P. Banerjee, D. V. Pelekhov, and P. C. Hammel. Nanoscale scanning probe ferromagnetic resonance imaging using localized modes. *Nature*, 466(7308):845–848, aug 2010.

[156] S.-C. Lee, K. Kim, J. Kim, S. Lee, J. Han Yi, S. Woo Kim, K.-S. Ha, and C. Cheong. One Micrometer Resolution NMR Microscopy. *Journal of Magnetic Resonance*, 150(2):207–213, jun 2001.

[157] S.-C. Lee, K. Kim, J. Kim, J. H. Yi, S. Lee, and C. Cheong. MR microscopy of micron scale structures. *Magnetic resonance imaging*, 27(6):828–33, jul 2009.

[158] P. J. Leek, J. M. Fink, A. Blais, R. Bianchetti, M. Goppl, J. M. Gambetta, D. I. Schuster, L. Frunzio, R. J. Schoelkopf, and A. Wallraff. Observation of Berry's Phase in a Solid-State Qubit. *Science*, 318(5858):1889–1892, dec 2007.

[159] D. Leibfried, B. DeMarco, V. Meyer, D. Lucas, M. Barrett, J. Britton, W. M. Itano, B. Jelenković, C. Langer, T. Rosenband, and D. J. Wineland. Experimental demonstration of a robust, high-fidelity geometric two ion-qubit phase gate. *Nature*, 422(6930):412–415, mar 2003.

[160] Q. Liang, C.-S. Yan, Y. Meng, J. Lai, S. Krasnicki, H.-K. Mao, and R. J. Hemley. Recent advances in high-growth rate single-crystal CVD diamond. *Diamond and Related Materials*, 18(5-8):698–703, may 2009.

[161] Y.-J. Lin, R. L. Compton, K. Jiménez-García, J. V. Porto, and I. B. Spielman. Synthetic magnetic fields for ultracold neutral atoms. *Nature*, 462(7273):628–632, dec 2009.

[162] D. Loss and D. P. DiVincenzo. Quantum computation with quantum dots. *Physical Review A*, 57(1):120–126, jan 1998.

[163] J. H. N. Loubser and J. A. van Wyk. Electron spin resonance in the study of diamond. *Reports on Progress in Physics*, 41(8):1201–1248, aug 1978.

[164] G. H. Low, T. J. Yoder, and I. L. Chuang. Quantum Imaging by Coherent Enhancement. *Physical Review Letters*, 114(10):100801, mar 2015.

[165] L. Luan, M. S. Grinolds, S. Hong, P. Maletinsky, R. L. Walsworth, and A. Yacoby. Decoherence imaging of spin ensembles using a scanning single-electron spin in diamond. *Scientific Reports*, 5:8119, jan 2015.

[166] M. Lustig, D. Donoho, J. Santos, and J. Pauly. Compressed Sensing MRI. *IEEE Signal Processing Magazine*, 25(2):72–82, mar 2008.

[167] R. M. Lutchyn, J. D. Sau, and S. Das Sarma. Majorana Fermions and a Topological Phase Transition in Semiconductor-Superconductor Heterostructures. *Physical Review Letters*, 105(7):077001, aug 2010.

[168] P. Maletinsky, S. Hong, M. S. Grinolds, B. Hausmann, M. D. Lukin, R. L. Walsworth, M. Loncar, and A. Yacoby. A robust scanning diamond sensor for nanoscale imaging with single nitrogen-vacancy centres. *Nature Nanotechnology*, 7(5):320–324, apr 2012.

[169] H. J. Mamin, M. Kim, M. H. Sherwood, C. T. Rettner, K. Ohno, D. D. Awschalom, and D. Rugar. Nanoscale Nuclear Magnetic Resonance with a Nitrogen-Vacancy Spin Sensor. *Science*, 339(6119):557–560, feb 2013.

[170] H. J. Mamin, C. T. Rettner, M. H. Sherwood, L. Gao, and D. Rugar. High field-gradient dysprosium tips for magnetic resonance force microscopy. *Applied Physics Letters*, 100(1):013102, 2012.

[171] P. Mansfield and P. K. Grannell. NMR 'diffraction' in solids? *Journal of Physics C: Solid State Physics*, 6(22):L422–L426, nov 1973.

[172] T. Matsunaga, T. Suzuki, M. Tanaka, and A. Arakaki. Molecular analysis of magnetotactic bacteria and development of functional bacterial magnetic particles for nano-biotechnology. *Trends in biotechnology*, 25(4):182–8, apr 2007.

[173] P. Maurer. *Coherent control of diamond defects for quantum information science and quantum sensing.* PhD thesis, Harvard University, 2014.

[174] P. C. Maurer, J. R. Maze, P. L. Stanwix, L. Jiang, A. V. Gorshkov, A. A. Zibrov, B. Harke, J. S. Hodges, A. S. Zibrov, A. Yacoby, D. Twitchen, S. W. Hell, R. L. Walsworth, and M. D. Lukin. Far-field optical imaging and manipulation of

individual spins with nanoscale resolution. *Nature Physics*, 6(11):912–918, nov 2010.

[175] J. R. Maze. *Quantum manipulation of nitrogen-vacancy centers in diamond: from basic properties to applications.* PhD thesis, Harvard University, 2010.

[176] J. R. Maze, P. L. Stanwix, J. S. Hodges, S. Hong, J. M. Taylor, P. Cappellaro, L. Jiang, M. V. G. Dutt, E. Togan, A. S. Zibrov, A. Yacoby, R. L. Walsworth, and M. D. Lukin. Nanoscale magnetic sensing with an individual electronic spin in diamond. *Nature*, 455(7213):644–647, oct 2008.

[177] T. McGuire and R. Potter. Anisotropic magnetoresistance in ferromagnetic 3d alloys. *IEEE Transactions on Magnetics*, 11(4):1018–1038, jul 1975.

[178] J. Meijer, B. Burchard, M. Domhan, C. Wittmann, T. Gaebel, I. Popa, F. Jelezko, and J. Wrachtrup. Generation of single color centers by focused nitrogen implantation. *Applied Physics Letters*, 87(26):261909, 2005.

[179] J. Michl, T. Teraji, S. Zaiser, I. Jakobi, G. Waldherr, F. Dolde, P. Neumann, M. W. Doherty, N. B. Manson, J. Isoya, and J. Wrachtrup. Perfect alignment and preferential orientation of nitrogen-vacancy centers during chemical vapor deposition diamond growth on (111) surfaces. *Applied Physics Letters*, 104(10):102407, mar 2014.

[180] M. Miller, P. Sheehan, R. Edelstein, C. Tamanaha, L. Zhong, S. Bounnak, L. Whitman, and R. Colton. A DNA array sensor utilizing magnetic microbeads and magnetoelectronic detection. *Journal of Magnetism and Magnetic Materials*, 225(1-2):138–144, jan 2001.

[181] C. V. Mora, M. Davison, J. M. Wild, and M. M. Walker. Magnetoreception and its trigeminal mediation in the homing pigeon. *Nature*, 432(7016):508–11, nov 2004.

[182] B. M. Moskowitz, R. B. Frankel, and D. A. Bazylinski. Rock magnetic criteria for the detection of biogenic magnetite. *Earth Planet. Sci. Lett.*, 120:283–300, 1993.

[183] B. M. Moskowitz, R. B. Frankel, and D. A. Bazylinski. Rock magnetic criteria for the detection of biogenic magnetite. *Earth and Planetary Science Letters*, 120(3-4):283–300, dec 1993.

[184] S. A. Murthy, D. Krause, Z. L. Li, and L. R. Hunter. New limits on the electron electric dipole moment from cesium. *Physical Review Letters*, 63(9):965–968, aug 1989.

[185] N. Nagaosa and Y. Tokura. Topological properties and dynamics of magnetic skyrmions. *Nature Nanotechnology*, 8(12):899–911, dec 2013.

[186] B. Naydenov, V. Richter, J. Beck, M. Steiner, P. Neumann, G. Balasubramanian, J. Achard, F. Jelezko, J. Wrachtrup, and R. Kalish. Enhanced generation of single optically active spins in diamond by ion implantation. *Applied Physics Letters*, 96(16):163108, 2010.

[187] P. Neumann. *Towards a room temperature solid state quantum processor - the nitrogen-vacancy center in diamond.* PhD thesis, University of Stuttgart, 2012.

[188] P. Neumann, R. Kolesov, B. Naydenov, J. Beck, F. Rempp, M. Steiner, V. Jacques, G. Balasubramanian, M. L. Markham, D. J. Twitchen, S. Pezzagna, J. Meijer, J. Twamley, F. Jelezko, and J. Wrachtrup. Quantum register based on coupled electron spins in a room-temperature solid. *Nature Physics*, 6(4):249–253, apr 2010.

[189] P. Neumann, N. Mizuochi, F. Rempp, P. Hemmer, H. Watanabe, S. Yamasaki, V. Jacques, T. Gaebel, F. Jelezko, and J. Wrachtrup. Multipartite Entanglement Among Single Spins in Diamond. *Science*, 320(5881):1326–1329, jun 2008.

[190] J. M. Nichol, T. R. Naibert, E. R. Hemesath, L. J. Lauhon, and R. Budakian. Nanoscale Fourier-Transform Magnetic Resonance Imaging. *Physical Review X*, 3(3):031016, sep 2013.

[191] N. M. Nusran, M. U. Momeen, and M. V. G. Dutt. High-dynamic-range magnetometry with a single electronic spin in diamond. *Nature Nanotechnology*, 7(2):109–113, dec 2011.

[192] B. K. Ofori-Okai, S. Pezzagna, K. Chang, M. Loretz, R. Schirhagl, Y. Tao, B. A. Moores, K. Groot-Berning, J. Meijer, and C. L. Degen. Spin properties of very shallow nitrogen vacancy defects in diamond. *Physical Review B*, 86(8):081406, aug 2012.

[193] K. Ohno. *Nanometer-scale engineering of shallow spins in diamond.* PhD thesis, University of California, Santa Barbara, 2014.

[194] K. Ohno, F. Joseph Heremans, L. C. Bassett, B. A. Myers, D. M. Toyli, A. C. Bleszynski Jayich, C. J. Palmstrøm, and D. D. Awschalom. Engineering shallow spins in diamond with nitrogen delta-doping. *Applied Physics Letters*, 101(8):082413, 2012.

[195] T. Okuno, K. Shigeto, T. Ono, K. Mibu, and T. Shinjo. MFM study of magnetic vortex cores in circular permalloy dots: behavior in external field. *Journal of Magnetism and Magnetic Materials*, 240(1-3):1–6, feb 2002.

[196] A. Oral, S. J. Bending, and M. Henini. Real-time scanning Hall probe microscopy. *Applied Physics Letters*, 69(9):1324, 1996.

[197] J. O. Orwa, C. Santori, K. M. C. Fu, B. Gibson, D. Simpson, I. Aharonovich, A. Stacey, A. Cimmino, P. Balog, M. Markham, D. Twitchen, A. D. Greentree, R. G. Beausoleil, and S. Prawer. Engineering of nitrogen-vacancy color centers in high purity diamond by ion implantation and annealing. *Journal of Applied Physics*, 109(8):083530, 2011.

[198] W. Pauli. Zur Quantenmechanik des magnetischen Elektrons. *Zeitschrift fur Physik*, 43(9-10):601–623, sep 1927.

[199] J. R. Petta. Coherent Manipulation of Coupled Electron Spins in Semiconductor Quantum Dots. *Science*, 309(5744):2180–2184, sep 2005.

[200] S. Pezzagna, B. Naydenov, F. Jelezko, J. Wrachtrup, and J. Meijer. Creation efficiency of nitrogen-vacancy centres in diamond. *New Journal of Physics*, 12(6):065017, jun 2010.

[201] S. Pezzagna, D. Rogalla, H.-W. Becker, I. Jakobi, F. Dolde, B. Naydenov, J. Wrachtrup, F. Jelezko, C. Trautmann, and J. Meijer. Creation of colour centres in diamond by collimated ion-implantation through nano-channels in mica. *physica status solidi (a)*, 208(9):2017–2022, sep 2011.

[202] L. M. Pham. *Magnetic Field Sensing with Nitrogen-Vacancy Color Centers in Diamond.* PhD thesis, Harvard University, 2013.

[203] L. M. Pham, N. Bar-Gill, C. Belthangady, D. Le Sage, P. Cappellaro, M. D. Lukin, A. Yacoby, and R. L. Walsworth. Enhanced solid-state multispin metrology using dynamical decoupling. *Physical Review B*, 86(4):045214, jul 2012.

[204] L. M. Pham, N. Bar-Gill, D. Le Sage, C. Belthangady, A. Stacey, M. Markham, D. J. Twitchen, M. D. Lukin, and R. L. Walsworth. Enhanced metrology using preferential orientation of nitrogen-vacancy centers in diamond. *Physical Review B*, 86(12):121202, sep 2012.

[205] L. M. Pham, D. Le Sage, P. L. Stanwix, T. K. Yeung, D. Glenn, A. Trifonov, P. Cappellaro, P. R. Hemmer, M. D. Lukin, H. Park, A. Yacoby, and R. L. Walsworth. Magnetic field imaging with nitrogen-vacancy ensembles. *New Journal of Physics*, 13(4):045021, apr 2011.

[206] D. F. Phillips, M. A. Humphrey, E. M. Mattison, R. E. Stoner, R. F. C. Vessot, and R. L. Walsworth. Limit on Lorentz and CPT violation of the proton using a hydrogen maser. *Physical Review D*, 63(11):111101, apr 2001.

[207] L. Popa. *Pulsed magnetic resonance on single defect centers in diamond.* PhD thesis, University of Stuttgart, 2006.

[208] M. Posfai and R. E. Dunin-Borkowski. Magnetic Nanocrystals in Organisms. *Elements*, 5(4):235–240, aug 2009.

[209] R. B. Proksch, T. E. Schäffer, B. M. Moskowitz, E. D. Dahlberg, D. A. Bazylinski, and R. B. Frankel. Magnetic force microscopy of the submicron magnetic assembly in a magnetotactic bacterium. *Applied Physics Letters*, 66(19):2582, 1995.

[210] L. Qian. Magnetic Characterization of Individual Magnetotactic Bacteria. In *APS March Meeting*, 2011.

[211] J. R. Rabeau, P. Reichart, G. Tamanyan, D. N. Jamieson, S. Prawer, F. Jelezko, T. Gaebel, I. Popa, M. Domhan, and J. Wrachtrup. Implantation of labelled single nitrogen vacancy centers in diamond using ^{15}N. *Applied Physics Letters*, 88(2):023113, 2006.

[212] I. I. Rabi. Space Quantization in a Gyrating Magnetic Field. *Physical Review*, 51(8):652–654, apr 1937.

[213] I. I. Rabi, J. R. Zacharias, S. Millman, and P. Kusch. A New Method of Measuring Nuclear Magnetic Moment. *Physical Review*, 53(4):318–318, feb 1938.

[214] P. Rabl, S. J. Kolkowitz, F. H. L. Koppens, J. G. E. Harris, P. Zoller, and M. D. Lukin. A quantum spin transducer based on nanoelectromechanical resonator arrays. *Nature Physics*, 6(8):602–608, aug 2010.

[215] L. Rahn-Lee, M. E. Byrne, M. Zhang, D. Le Sage, D. R. Glenn, T. Milbourne, R. L. Walsworth, H. Vali, and A. Komeili. A Genetic Strategy for Probing the Functional Diversity of Magnetosome Formation. *PLoS Genetics*, 11(1):e1004811, jan 2015.

[216] N. F. Ramsey. A Molecular Beam Resonance Method with Separated Oscillating Fields. *Physical Review*, 78(6):695–699, jun 1950.

[217] N. Reddy, N. Manson, and E. Krausz. Two-laser spectral hole burning in a colour centre in diamond. *Journal of Luminescence*, 38(1-6):46–47, dec 1987.

[218] J. Rife, M. Miller, P. Sheehan, C. Tamanaha, M. Tondra, and L. Whitman. Design and performance of GMR sensors for the detection of magnetic microbeads in biosensors. *Sensors and Actuators A: Physical*, 107(3):209–218, nov 2003.

[219] P. Ripka. Review of fluxgate sensors. *Sensors and Actuators A: Physical*, 33(3):129–141, jun 1992.

[220] P. Ripka. Advances in fluxgate sensors. *Sensors and Actuators A: Physical*, 106(1-3):8–14, sep 2003.

[221] L. Robledo, H. Bernien, T. van der Sar, and R. Hanson. Spin dynamics in the optical cycle of single nitrogen-vacancy centres in diamond. *New Journal of Physics*, 13(2):025013, feb 2011.

[222] L. J. Rogers, S. Armstrong, M. J. Sellars, and N. B. Manson. Infrared emission of the NV centre in diamond: Zeeman and uniaxial stress studies. *New Journal of Physics*, 10(10):103024, oct 2008.

[223] L. Rondin, J. P. Tetienne, S. Rohart, A. Thiaville, T. Hingant, P. Spinicelli, J. F. Roch, and V. Jacques. Stray-field imaging of magnetic vortices with a single diamond spin. *Nature Communications*, 4, jul 2013.

[224] P. Roushan, C. Neill, Y. Chen, M. Kolodrubetz, C. Quintana, N. Leung, M. Fang, R. Barends, B. Campbell, Z. Chen, B. Chiaro, A. Dunsworth, E. Jeffrey, J. Kelly, A. Megrant, J. Mutus, P. J. J. O'Malley, D. Sank, A. Vainsencher, J. Wenner, T. White, A. Polkovnikov, A. N. Cleland, and J. M. Martinis. Observation of topological transitions in interacting quantum circuits. *Nature*, 515(7526):241–244, nov 2014.

[225] D. Rugar, R. Budakian, H. J. Mamin, and B. W. Chui. Single spin detection by magnetic resonance force microscopy. *Nature*, 430(6997):329–332, jul 2004.

[226] M. J. Rust, M. Bates, and X. Zhuang. Sub-diffraction-limit imaging by stochastic optical reconstruction microscopy (STORM). *Nature Methods*, 3(10):793–796, oct 2006.

[227] J. Samuel and R. Bhandari. General Setting for Berry's Phase. *Physical Review Letters*, 60(23):2339–2342, jun 1988.

[228] V. Shah, S. Knappe, P. D. D. Schwindt, and J. Kitching. Subpicotesla atomic magnetometry with a microfabricated vapour cell. *Nature Photonics*, 1(11):649–652, nov 2007.

[229] F. Shi, Q. Zhang, P. Wang, H. Sun, J. Wang, X. Rong, M. Chen, C. Ju, F. Reinhard, H. Chen, J. Wrachtrup, J. Wang, and J. Du. Single-protein spin resonance spectroscopy under ambient conditions. *Science*, 347(6226):1135–1138, mar 2015.

[230] B. Shields. *Diamond Platforms for Nanoscale Photonics and Metrology.* PhD thesis, Harvard University, 2014.

[231] C. Shin, C. Kim, R. Kolesov, G. Balasubramanian, F. Jelezko, J. Wrachtrup, and P. R. Hemmer. Sub-optical resolution of single spins using magnetic resonance imaging at room temperature in diamond. *Journal of Luminescence*, 130(9):1635–1645, sep 2010.

[232] C. G. Shull and E. O. Wollan. X-Ray, Electron, and Neutron Diffraction. *Science*, 108(2795):69–75, jul 1948.

[233] E. Sjöqvist, D. M. Tong, L. Mauritz Andersson, B. Hessmo, M. Johansson, and K. Singh. Non-adiabatic holonomic quantum computation. *New Journal of Physics*, 14(10):103035, oct 2012.

[234] C. P. Slichter. *Principles of Magnetic Resonance*, volume 1 of *Springer Series in Solid-State Sciences.* Springer Berlin Heidelberg, Berlin, Heidelberg, 1990.

[235] M. Smith, P. Sheehan, L. Perry, K. OâĂŹConnor, L. Csonka, B. Applegate, and L. Whitman. Quantifying the Magnetic Advantage in Magnetotaxis. *Biophysical Journal*, 91(3):1098–1107, aug 2006.

[236] A. Sodickson. A generalized k-space formalism for treating the spatial aspects of a variety of NMR experiments. *Progress in Nuclear Magnetic Resonance Spectroscopy*, 33(2):77–108, aug 1998.

[237] I. Solomon. Rotary Spin Echoes. *Physical Review Letters*, 2(7):301–302, apr 1959.

[238] P. L. Stanwix, L. M. Pham, J. R. Maze, D. Le Sage, T. K. Yeung, P. Cappellaro, P. R. Hemmer, A. Yacoby, M. D. Lukin, and R. L. Walsworth. Coherence of nitrogen-vacancy electronic spin ensembles in diamond. *Physical Review B*, 82(20):201201, nov 2010.

[239] T. Staudacher, F. Shi, S. Pezzagna, J. Meijer, J. Du, C. A. Meriles, F. Reinhard, and J. Wrachtrup. Nuclear Magnetic Resonance Spectroscopy on a (5-Nanometer)3 Sample Volume. *Science*, 339(6119):561–563, feb 2013.

[240] M. Steiner. *Towards diamond-based quantum computers.* PhD thesis, University of Stuttgart, 2009.

[241] M. Steiner, P. Neumann, J. Beck, F. Jelezko, and J. Wrachtrup. Universal enhancement of the optical readout fidelity of single electron spins at nitrogen-vacancy centers in diamond. *Physical Review B*, 81(3):035205, jan 2010.

[242] S. Steinert, F. Dolde, P. Neumann, A. Aird, B. Naydenov, G. Balasubramanian, F. Jelezko, and J. Wrachtrup. High sensitivity magnetic imaging using an array of spins in diamond. *The Review of scientific instruments*, 81(4):043705, apr 2010.

[243] K. Sternickel and A. I. Braginski. Biomagnetism using SQUIDs: status and perspectives. *Superconductor Science and Technology*, 19(3):S160–S171, mar 2006.

[244] A. O. Sushkov, N. Chisholm, I. Lovchinsky, M. Kubo, P. K. Lo, S. D. Bennett, D. Hunger, A. Akimov, R. L. Walsworth, H. Park, and M. D. Lukin. All-Optical Sensing of a Single-Molecule Electron Spin. *Nano Letters*, 14(11):6443–6448, nov 2014.

[245] A. O. Sushkov, I. Lovchinsky, N. Chisholm, R. L. Walsworth, H. Park, and M. D. Lukin. Magnetic Resonance Detection of Individual Proton Spins Using Quantum Reporters. *Physical Review Letters*, 113(19):197601, nov 2014.

[246] D. Suter, K. T. Mueller, and A. Pines. Study of the Aharonov-Anandan quantum phase by NMR interferometry. *Physical Review Letters*, 60(13):1218–1220, mar 1988.

[247] M. Takamoto, F.-L. Hong, R. Higashi, and H. Katori. An optical lattice clock. *Nature*, 435(7040):321–324, may 2005.

[248] A. Tallaire, A. Collins, D. Charles, J. Achard, R. Sussmann, A. Gicquel, M. Newton, A. Edmonds, and R. Cruddace. Characterisation of high-quality thick single-crystal diamond grown by CVD with a low nitrogen addition. *Diamond and Related Materials*, 15(10):1700–1707, oct 2006.

[249] J. M. Taylor, P. Cappellaro, L. Childress, L. Jiang, D. Budker, P. R. Hemmer, A. Yacoby, R. Walsworth, and M. D. Lukin. High-sensitivity diamond magnetometer with nanoscale resolution. *Nature Physics*, 4(10):810–816, oct 2008.

[250] J.-P. Tetienne, T. Hingant, J.-V. Kim, L. H. Diez, J.-P. Adam, K. Garcia, J.-F. Roch, S. Rohart, A. Thiaville, D. Ravelosona, and V. Jacques. Nanoscale imaging and control of domain-wall hopping with a nitrogen-vacancy center microscope. *Science*, 344(6190):1366–1369, jun 2014.

[251] J.-P. Tetienne, L. Rondin, P. Spinicelli, M. Chipaux, T. Debuisschert, J.-F. Roch, and V. Jacques. Magnetic-field-dependent photodynamics of single NV defects in diamond: an application to qualitative all-optical magnetic imaging. *New Journal of Physics*, 14(10):103033, oct 2012.

[252] L. H. Thomas. The Motion of the Spinning Electron. *Nature*, 117(2945):514–514, apr 1926.

[253] D. J. Thouless, M. Kohmoto, M. P. Nightingale, and M. den Nijs. Quantized Hall Conductance in a Two-Dimensional Periodic Potential. *Physical Review Letters*, 49(6):405–408, aug 1982.

[254] E. Togan. *Optical Control of Individual Nitrogen-Vacancy Centers in Diamond.* PhD thesis, Harvard University, 2011.

[255] E. Togan, Y. Chu, A. S. Trifonov, L. Jiang, J. Maze, L. Childress, M. V. G. Dutt, A. S. Sørensen, P. R. Hemmer, A. S. Zibrov, and M. D. Lukin. Quantum entanglement between an optical photon and a solid-state spin qubit. *Nature*, 466(7307):730–734, aug 2010.

[256] A. Tomita and R. Y. Chiao. Observation of Berry's Topological Phase by Use of an Optical Fiber. *Physical Review Letters*, 57(8):937–940, aug 1986.

[257] S. Tomonaga. The Story of Spin. *American Journal of Physics*, 66(9):839, 1998.

[258] D. M. Toyli, C. F. de las Casas, D. J. Christle, V. V. Dobrovitski, and D. D. Awschalom. Fluorescence thermometry enhanced by the quantum coherence of single spins in diamond. *Proceedings of the National Academy of Sciences*, 110(21):8417–8421, may 2013.

[259] D. M. Toyli, C. D. Weis, G. D. Fuchs, T. Schenkel, and D. D. Awschalom. Chip-Scale Nanofabrication of Single Spins and Spin Arrays in Diamond. *Nano Letters*, 10(8):3168–3172, aug 2010.

[260] A. S. Trifonov, J.-C. Jaskula, C. Teulon, D. R. Glenn, N. Bar-Gill, and R. L. Walsworth. Limits to Resolution of CW STED Microscopy. In *Advances In Atomic, Molecular, and Optical Physics*, pages 279–302. Academic Press, 2013.

[261] G. E. Uhlenbeck and S. Goudsmit. Spinning Electrons and the Structure of Spectra. *Nature*, 117(2938):264–265, feb 1926.

[262] T. Van der Sar. *Quantum control of single spins and single photons in diamond.* PhD thesis, Delft University of Technology, 2012.

[263] T. van der Sar, F. Casola, R. Walsworth, and A. Yacoby. Nanometre-scale probing of spin waves using single-electron spins. *Nature Communications*, 6:7886, aug 2015.

[264] B. Van Waeyenberge, A. Puzic, H. Stoll, K. W. Chou, T. Tyliszczak, R. Hertel, M. Fähnle, H. Brückl, K. Rott, G. Reiss, I. Neudecker, D. Weiss, C. H. Back, and G. Schütz. Magnetic vortex core reversal by excitation with short bursts of an alternating field. *Nature*, 444(7118):461–464, nov 2006.

[265] M. Vengalattore, J. M. Higbie, S. R. Leslie, J. Guzman, L. E. Sadler, and D. M. Stamper-Kurn. High-Resolution Magnetometry with a Spinor Bose-Einstein Condensate. *Physical Review Letters*, 98(20):200801, may 2007.

[266] G. Waldherr. *Precision quantum state preparation and readout of solid state spin.* PhD thesis, University of Stuttgart, 2014.

[267] G. Waldherr, J. Beck, P. Neumann, R. S. Said, M. Nitsche, M. L. Markham, D. J. Twitchen, J. Twamley, F. Jelezko, and J. Wrachtrup. High-dynamic-range magnetometry with a single nuclear spin in diamond. *Nature Nanotechnology*, 7(2):105–108, dec 2011.

[268] S. X. Wang, J. Labaziewicz, Y. Ge, R. Shewmon, and I. L. Chuang. Individual addressing of ions using magnetic field gradients in a surface-electrode ion trap. *Applied Physics Letters*, 94(9):094103, 2009.

[269] X. G. Wen and Q. Niu. Ground-state degeneracy of the fractional quantum Hall states in the presence of a random potential and on high-genus Riemann surfaces. *Physical Review B*, 41(13):9377–9396, may 1990.

[270] X. G. Wen, F. Wilczek, and A. Zee. Chiral spin states and superconductivity. *Physical Review B*, 39(16):11413–11423, jun 1989.

[271] F. Wilczek and A. Zee. Appearance of Gauge Structure in Simple Dynamical Systems. *Physical Review Letters*, 52(24):2111–2114, jun 1984.

[272] D. Wildanger, B. R. Patton, H. Schill, L. Marseglia, J. P. Hadden, S. Knauer, A. Schönle, J. G. Rarity, J. L. O'Brien, S. W. Hell, and J. M. Smith. Solid

Immersion Facilitates Fluorescence Microscopy with Nanometer Resolution and Sub-Ångström Emitter Localization. *Advanced Materials*, 24(44):OP309–OP313, nov 2012.

[273] D. J. Wineland, J. J. Bollinger, W. M. Itano, F. L. Moore, and D. J. Heinzen. Spin squeezing and reduced quantum noise in spectroscopy. *Physical Review A*, 46(11):R6797–R6800, dec 1992.

[274] S. A. Wolf. Spintronics: A Spin-Based Electronics Vision for the Future. *Science*, 294(5546):1488–1495, nov 2001.

[275] W. X. Xia, Y. S. Chun, S. Aizawa, K. Yanagisawa, K. M. Krishnan, D. Shindo, and A. Tonomura. Investigation of magnetic structure and magnetization process of yttrium iron garnet film by Lorentz microscopy and electron holography. *Journal of Applied Physics*, 108(12):123919, 2010.

[276] C. N. Yang and R. L. Mills. Conservation of Isotopic Spin and Isotopic Gauge Invariance. *Physical Review*, 96(1):191–195, oct 1954.

[277] N. Yao. *Topology, Localization, and Quantum Information in Atomic, Molecular and Optical Systems.* PhD thesis, Harvard University, 2014.

[278] N. Yao, L. Jiang, A. Gorshkov, P. Maurer, G. Giedke, J. Cirac, and M. Lukin. Scalable architecture for a room temperature solid-state quantum information processor. *Nature Communications*, 3:800, apr 2012.

[279] A. N. Youdin, D. Krause, Jr., K. Jagannathan, L. R. Hunter, and S. K. Lamoreaux. Limits on Spin-Mass Couplings within the Axion Window. *Physical Review Letters*, 77(11):2170–2173, sep 1996.

[280] A. M. Zaitsev. *Optical Properties of Diamond.* Springer Berlin Heidelberg, Berlin, Heidelberg, 2001.

[281] P. Zanardi and M. Rasetti. Holonomic quantum computation. *Physics Letters A*, 264(2-3):94–99, dec 1999.

[282] Y. Zhang, Y.-W. Tan, H. L. Stormer, and P. Kim. Experimental observation of the quantum Hall effect and Berry's phase in graphene. *Nature*, 438(7065):201–4, nov 2005.

[283] C. Zu, W.-B. Wang, L. He, W.-G. Zhang, C.-Y. Dai, F. Wang, and L.-M. Duan. Experimental realization of universal geometric quantum gates with solid-state spins. *Nature*, 514(7520):72–75, oct 2014.

[284] O. Zurkiya, A. W. S. Chan, and X. Hu. MagA is sufficient for producing magnetic nanoparticles in mammalian cells, making it an MRI reporter. *Magnetic resonance in medicine*, 59(6):1225–31, jun 2008.